Yu Lin

Simulation of Inhomogeneous Wave Conditions and their Effect on Dynamic Responses of a Floating Bridge

Master's thesis

NTNU
Norwegian University of Science and Technology
Faculty of Engineering
Department of Marine Technology

NTNU
Norwegian University of
Science and Technology

DTU
Technical
University of
Denmark

Yu Lin

Simulation of Inhomogeneous Wave Conditions and their Effect on Dynamic Responses of a Floating Bridge

Master's thesis in Marine Technology
Supervisor: Zhen Gao (NTNU), Yanlin Shao (DTU)
June 2020

Norwegian University of Science and Technology
Faculty of Engineering
Department of Marine Technology

NTNU
Norwegian University of
Science and Technology

NTNU Trondheim
Norwegian University of Science and Technology
Department of Marine Technology

MSC THESIS IN MARINE TECHNOLOGY

SPRING 2020

FOR

Yu Lin

Simulation of Inhomogeneous Wave Conditions and their Effect on Dynamic Responses of a Floating Bridge

Background:

The E39 Coastal Highway Route Project is being developed to reduce the travel time between Trondheim and Kristiansand in Norway and several ferry connections are planned to be replaced by floating bridges or submerged floating tunnels. In this study, a curved floating bridge design for crossing the Bjørnafjorden from COWI is considered, as shown in Figure 6.1.

The curved floating bridge is designed to be supported by one tower with cables at the south end of the bridge and 19 floating pontoons without side moorings. It has a total length of 5 km and the spacing between the adjacent pontoon is about 200m, for which the wave conditions on each pontoon might not be homogeneous. From the long-term point of view, the distribution of the wave conditions in terms of significant wave height and spectral peak period is different at the 19 pontoon locations. From the short-term point of view, there exists a coherence structure between the wave elevations at 19 pontoon locations. Such wave conditions may induce resonant responses of the floating bridges that cannot be captured using a homogeneous wave assumption.

The main goal of this master thesis work is to set up a numerical procedure for time-domain simulations of inhomogeneous wave conditions based on the given coherence function of the wave elevation and to study its effect on dynamic responses of a cable-stayed curved floating bridge for a Norwegian fjord.

Assignment:
The following tasks should be addressed in the thesis work:

Thesis tasks:
1. Based on the measurement data of wave elevation time series at the three locations across the Bjørnafjord, estimate the coherence function for a set of wave frequencies. Assuming a certain coherence structure with respect to the distance, establish a coherence function for the wave elevations in the fjord.

2. With the assumed coherence function (i.e. auto-/cross-spectrum matrix of wave elevations at different pontoons of the floating bridge), considering the number of pontoons of the floating bridge, establish first a theoretical time-domain simulation model for the generation

of the wave elevations at these pontoon locations. The methods based on Campbell's formulation and Cholesky decomposition of the auto-/cross-spectrum matrix should be derived in detail.

3. Then carry out stochastic time-domain wave simulations in Matlab, using these two methods, for the cases of 2, 3 and 19 components of the auto-/cross-spectrum matrix.

4. Based on the wave simulation results, use the SIMA model of the floating bridge to perform time-domain response analysis of the bridge due to wave loads. Compare the responses for the cases with and without the consideration of coherence functions between the wave elevations at different pontoon locations.

5. Summarize the work and write the thesis.

In the thesis the candidate shall present his/her personal contribution to the resolution of problem within the scope of the thesis work.

Theories and conclusions should be based on mathematical derivations and/or logic reasoning identifying the various steps in the deduction.

The candidate should utilize the existing possibilities for obtaining relevant literature.

The thesis should be organized in a rational manner to give a clear exposition of results, assessments, and conclusions. The text should be brief and to the point, with a clear language. Telegraphic language should be avoided.

The thesis shall contain the following elements: A text defining the scope, preface, list of contents, summary, main body of thesis, conclusions with recommendations for further work, list of symbols and acronyms, reference and (optional) appendices. All figures, tables and equations shall be numerated.

The supervisor may require that the candidate, in an early stage of the work, present a written plan for the completion of the work. The plan should include a budget for the use of computer and laboratory resources that will be charged to the department. Overruns shall be reported to the supervisor.

The original contribution of the candidate and material taken from other sources shall be clearly defined. Work from other sources shall be properly referenced using an acknowledged referencing system.

The thesis shall be submitted in Inspera:
- Signed by the candidate
- The text defining the scope included
- Other thesis work information, like computer codes, etc. should be organized in a separate folder.

Supervisor:

Prof. Zhen Gao

Deadline for master thesis: 10.6.2020

Preface

This thesis is the final work written by Yu Lin for the Joint Nordic Master's degree program in Maritime Engineering with the specialization of Ocean Structures. This programme aims to achieve dual degrees of MSc in Marine Technology at the Norwegian University of Science and Technology (NTNU) and MSc in Maritime Engineering at the Technical University of Denmark (DTU). The thesis work has been conducted under supervision of Professor Zhen Gao at NTNU as a main supervisor and Associate Professor Yanlin Shao at DTU as a co-supervisor.

Acknowledgement

Yu Lin
10/06/2020

Abstract

The Norwegian Public Roads Administration (NPRA) has launched The Ferry-free E39 Coastal Highway Route project in order to reduce the travel time from 21 hours to 11 hours between Trondheim and Kristiansand by applying bridges and tunnels to replace the current fjord ferries. In this study, one of the seven fjords, Bjørnafjorden is focused. The end-anchored curved floating bridge which is a long curved structure of 5 km supported by 19 was proposed to cross Bjørnafjorden. Due to the complex topography of Bjørnafjorden, the wave field is inhomogeneous along the fjord which might excite asymmetrical eigenmodes of the floating bridge. The inhomogeneity of the wave field was revealed by analyzing the wave elevation data collected by three Datawell Waveriders (DWRs) [7]. Since it is hard to keep collecting real-time wave elevations for a long period, numerical simulation of the inhomogeneous short-term wave field is necessary to be carried out in this study.

The 3-hour short term simulation of times series at each pontoon requires known wave spectrum and coherence between wave elevations along the fjord. The coherence structure of the waves across the fjord is assumed based on the analysis of collected wave data. The coherence structure along the fjord plays an important role in each simulation since it exists among the wave field objectively and it is essential to compute cross-spectrum. By applying the proposed coherence functions at 19 pontoons, a Matlab code was developed to generate time series of the wave elevations with two methods, Campbell analogy, and Cholesky decomposition. The criterion for evaluating the quality of the wave elevation method is to assess if the wave characteristics such as significant wave height H_s and wave peak period T_p of generated wave elevations can return to the input data. In this paper, four cases are conducted which include 1-year, 100-year homogeneous wave condition, and 1-year, 100-year inhomogeneous wave condition. The inhomogeneity of the input data of four combinations is reflected in significant wave heights while the input data have the same wave directions 288 [°] and homogeneous peak wave periods. The results, wave characteristics, of two methods, are always inhomogeneous due to the constitutional randomness inside the wave simulation procedure. By comparing the results of four cases, the Cholesky decomposition method has better performance than Campbell analogy in general and the simulations perform more accurately for 100-year wave condition with a lower deviation rate below 2 percent.

Furthermore, with the given numerical model of the floating bridge provided by Cheng in the software SIMA, the effects on the global dynamic responses of the floating bridge, including the bridge girder cross-sectional loads, moments of the bridge girder and the rigid body motions. In addition, wave excitation loads are generated by Matlab code on different pontoons considering the inhomogeneous wave condition and are imported as external forces into SIMA simulations.

Table of Contents

List of Tables

List of Figures

Abbreviations

τ	=	Time interval
β	=	Phase angle of filter function
ω	=	Frequency
ω_n	=	Certain frequency
ω_p	=	Wave peak frequency
σ	=	Standard deviation
ρ	=	Correlation coefficient
ζ_a	=	Wave amplitude
$\zeta(x, y, t)$	=	Time series of wave elevations
ϕ	=	Phase angle of wave elevations
θ	=	Wave direction
η	=	Wave elevations
ϵ	=	Random phase angle, uniformly distributed between 0 to 2π
$\mathbf{A}$	=	Hermitian positive matrix
A^{∞}	=	Added mass at infinite frequency
A_{γ}	=	Normalizing factor
a_i	=	Signal amplitude
B	=	Damping of the system
C	=	Stiffness of the system
$Coh_{xy}(\omega)$	=	Coherence function
$\mathbf{D}$	=	Diagonal matrix
$D(\theta)$	=	Directional distribution function
F^{ext}	=	Excitation force
F^{drag}	=	Drag force
F_x	=	Axial force
$G(X)$	=	Transfer function
H_s	=	Significant wave height
$H(\omega)$	=	Filter function
$H(\omega, \theta)$	=	Transfer function
i	=	Order of pontoon, 1 to 19
i	=	Degree of freedom, 1 to 6
j	=	Order of pontoon, 1 to 19
j	=	Degree of freedom, 1 to 6

L	=	Lower triangular matrix with diagonal elements
M	=	Mass of the system
M_x	=	Torsion moment
M_y	=	Moment about bridge girder strong axis, y
M_z	=	Moment about bridge girder strong axis, z
m	=	Mean value
m_i	=	i-th spectral moments
R_x	=	Auto-correlation function of signal x
R_{xy}	=	Cross-correlation function of signal x and y
$S(\omega)$	=	Wave spectrum
S_{ij}	=	Wave spectrum at i,j pontoon
S_y	=	Input wave spectrum with known wave characteristics
S_{yy}	=	Marix form of S_y
$S_x(\omega, \theta)$	=	Directional wave spectrum
$S_{xy}(\omega)$	=	Cross-spectrum
$S_{JONSWAP}(\omega)$	=	Jonswap wave spectrum
T_p	=	Wave peak period
T_z	=	Zero up-crossing wave period
t	=	Time
x	=	Time series of signal
x_i	=	Time series of Gaussian white noise
$X(\omega)$	=	Spectrum of Gaussian white noise
$\ddot{x}$	=	Acceleration
$\dot{x}$	=	Velocity
y	=	Time series of signal
y_i	=	Time series of wave elevations by simulation at no.i pontoon
$Y(\omega)$	=	Spectrum of wave time series

DTU	=	Technical University of Denmark
DWRs	=	Datawell Direc-tional Wave Riders
E39	=	European route E39
JONSWAP	=	JOint North Sea WAve Project
NPRA	=	Norwegian Public Road Administration
NTNU	=	Norwegian University of Science and Technology
RIFLEX	=	A program for hydrodynamic and structural slender marine structures
SIMA	=	A workbench which offers a complete solution for simulation and analysis of marine operations and floating systems
SIMO	=	A time domain simulation program for study of motions and station keeping of multi-body systems
TLP	=	Tension Leg Platform

Introduction

Background

The Norwegian Public Road Administration (NPRA) has announced the National transport plan 2018–2029: The Storting has a long-term goal to develop the E39 as an improved and continuous Coastal Highway Route between Kristiansand and Trondheim. The route shown in Fig. 1.1 runs from Kristiansand in the south to Trondheim in the north and is approximately 1100 km long. The route runs through the cities of Stavanger, Bergen, Ålesund, and Molde. Travel time today is around 21 hours, and road users need to use seven different ferry connections. The aim is to create an improved E39, which will reduce travel time by half. The route will be almost 50 kilometers shorter. The reduction in travel time will be achieved by replacing ferries with bridges and tunnels, or more frequent ferries - in addition to upgrading a number of road sections on land. An improved and continuous route for the efficient transport of people and goods ties the region efficiently together and will also contribute to a more efficient industry.

Figure 1.1: E39 Route

Part of the program [2] [15] [16] includes technical development to find the possibility of crossing the fjords along the highway route. The goal can be achieved by implementing existing technologies to some extent and for the rest part, the new method is supposed to be developed. Some of the technologies which are currently applied in offshore structures field can be used for reference. Fjord crossings differ from each case, and the need for technology must be analyzed specifically for each individual project. The potential technical solutions for fjord crossings [17] are shown in Fig.1.2.

Fjord Crossings	Potential solutions					Technology resolved
	Tunnel	Suspension	Tube	Floating	TLP	
Rogfast	X					Complete
Langenuen		X				Complete
Bjørnafjorden				X	X	Complete
Sognefjorden		X	X		X	2022
Nordfjorden		X				Complete
Vartdalsfjorden		X	X	X	X	2019
Sulafjorden		X	X		X	2020
Romsdalsfjorden	X					Complete
Julsundet		X				Complete
Halsafjorden		X	X	X	X	2019
Familiar technology	Familiar technology further developed			New technology required		

Figure 1.2: Potential crossing methods for the fjords

In this thesis, one of these fjords in this project, Bjørnafjorden is studied located between Bergen and Stavanger. The width of Bjørnafjorden is 5 kilometers and the depth is 500 meters. Due to the rough geographical conditions in fjords, it is difficult and costly to make traditional bridges. Several potential crossing methods were come up for crossing Bjørnafjorden. The Storting proposed to implement a floating bridge and TLP(Tension Leg Platform) as the crossing method. In Sunghun's thesis [11], a submerged floating tube tunnel was introduced shortly.

Challenges

The floating bridge is about 5.3 km with curvilinear shape and contains a cable-stayed high bridge part and a low floating bridge part supported by 19 pontoons in total. The environmental condition in Bjørnafjorden is wind and wave combined conditions. At the initial stage of the project, the floating bridge was designed for homogeneous wave conditions. The before studies[11] were carried out with homogeneous wave conditions which are not rational compared to the real case. Thanks to Cheng et al.[7] worked on processing the data collected with three DWRs for two years in the fjord, some critical wave properties like significant wave height and peak period were obtained. In Cheng et al. studies, the analyzed wave conditions along the fjord lead to inhomogeneity since there exist differences of sea states between three sets of collected data. The challenge is to simulate the wave conditions along the fjord from only three points' data while there are 19 pontoons. The ideal case will be that 19 DWRs are implemented located on the proposed positions of pontoons to collect the time series. In this thesis, the coherence function is applied to simulate the wave condition alone the fjord.

Objective

The main objective of this thesis is to simulate the inhomogeneous wave condition along the fjord by employing the coherence function and carry out the calculation of global dynamic responses. The methodology of applying the coherence function will also be studied.

Pre-thesis

During the third semester, the pre-thesis thesis was prepared for this thesis. The pre-project mainly focused on the literature review which provides background knowledge to the author. The case of the Ferry-Free E39 project and previous wave condition studies were reviewed by Cheng et al.[7] Wind field simulation [13] which has had validated coherence function in use was considered as a reference. Several studies [1] [18] about inhomogeneous wave conditions at Bjørnafjorden come up with some interpolation methods to solve the inhomogeneity. Transfer function used to compute turbulence from Gaussian white noise at more than one point was studied. The numerical model of the given curved floating bridge in SIMO-Riflex from Cheng is used to model the hydrodynamic loads and analyze the bridge responses.

Scope of Thesis

This thesis focuses on another field which is different from the previous study, the main scope of this thesis can be summarized as below:

- Applying stochastic theory for creating filter functions and coherence functions.

- Developing the numerical procedure of generating time series of wave elevation along the fjord.

- Generating the wave elevations and defining the wave conditions at each pontoon.

- Analyzing the global dynamic motion of the floating bridge.

1.1   The Ferry-free E39 Project Plan

The ambition of the Storting is to link Western Norway together with an upgraded high-way E39. The linking of large business regions and housing, labor, and service markets will provide a better basis for developing Norway's largest export region.

Benefits For Freight Transport

The scope of the project is to improve a stretch of the existing E39 highway between the cities of Kristians and Trondheim in Norway, a route that is 1100 kilometers long. Today, the route has seven ferry crossings, the NPRA is considering replacing some of these fjord crossings with alternative structures (i.e. tunnels or bridges) to reduce the travel time along the western coast of Norway. A reduction in distance, travel time, and disruptions will improve conditions for freight transport on this route. Driving costs and time costs will be reduced, whereas toll costs will increase temporarily in the tolling period. All in all, the cost level for heavy vehicles will be lower with a continuous E39 than it is today. When the toll periods for the entire route expire, the costs for heavy vehicles will be significantly reduced compared with today's level.

Benefits For Passenger Cars

Realizing the E39 as an improved and continuous route with fixed links will reduce the travel time from Kristians and to Trondheim by around 11 hours. Reduction in distance, travel time, and disruptions will reduce driving costs and time costs for passenger cars, but toll costs will increase temporarily in the toll periods. All in all, the cost level for passenger vehicles will be reduced by almost half compared to today. When the toll periods for the entire route expire, the costs for passenger cars will be reduced by one third compared to today's level.

Fjords In The Project

There are several fjords in Ferry-Free E39 projects marked in Fig.1.1. Table.1.1 shows the width and depth of all the fjords along the west side of Norway. The widest fjord is 26,700 meters while the shortest one is 1,300 meters. The depth varies from 330 meters to 1,250 meters.

	Width[m]	Depth[m]
Halsafjorden	2,000	500-600
Julsundet	1,600	500-600
Romsdalsfjorden	13,000	330
Sulafjorden	3,800	500
Vartdalsfjorden	2,100	600
Nordfjorden	1,700	300-500
Sognefjorden	3,700	1,250
Bjørnafjorden	5,000	500-600
Langenuen	1,300	500
Boknafjorden (Rogfast Subsea tunnel)	26,700	390

Table 1.1: Fjords in E-39 project

1.2 Bjørnafjorden

1.2.1 Location

Bjørnafjorden Fig.1.3 is located in Hordaland county about 30 km south of Bergen. The width and the depth of the fjord are approximately 5 km and 583 m respectively. As illustrated in Fig.1.3 , the proposed curved floating bridge will be installed over Bjørnafjorden and connect Svarvahella at Rekstern and Søre Øyane.
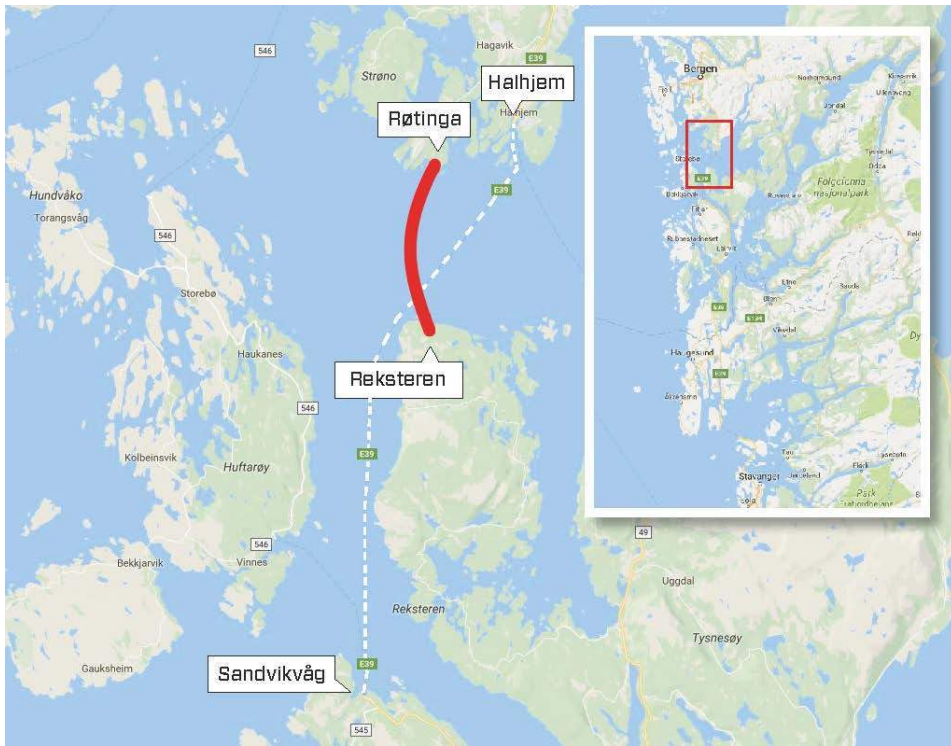
Figure 1.3: Location of Bjørnafjorden Fjord

1.2.2 Crossing Method

According to Fig. 1.2, end-anchored curved floating bridge, and multi-span suspension bridge supported by TLP are considered for Bjørnafjorden which are both required with new technology. The submerged floating tunnel is also introduced here. The illustrations and designs of all the crossing methods are shown below in Fig.1.4, Fig.1.5 and Fig.1.8.In this thesis, the end-anchored cable-stayed curved floating bridge prepared by COWI et al. is discussed.

(a) Illustration
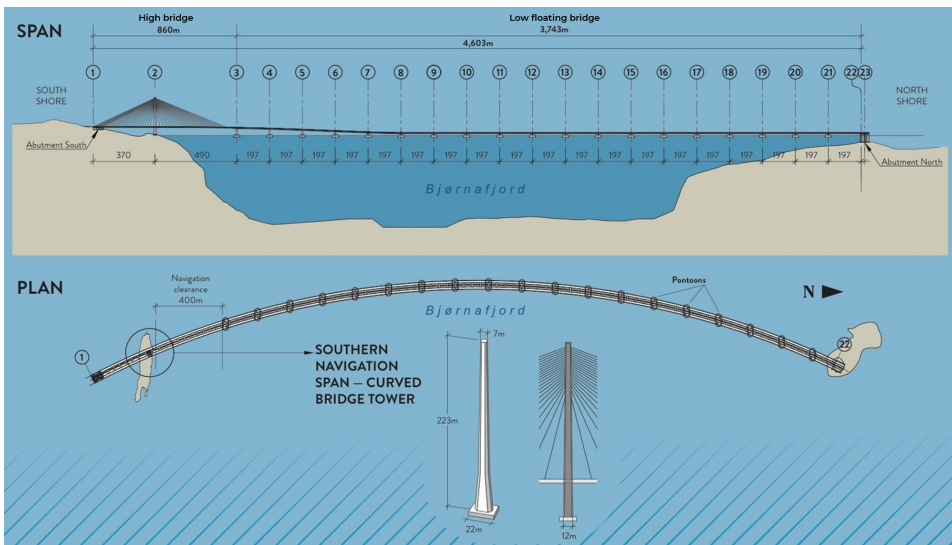
(b) Design

Figure 1.4: End-anchored curved floating bridge:(a)Illustration, (b) Design
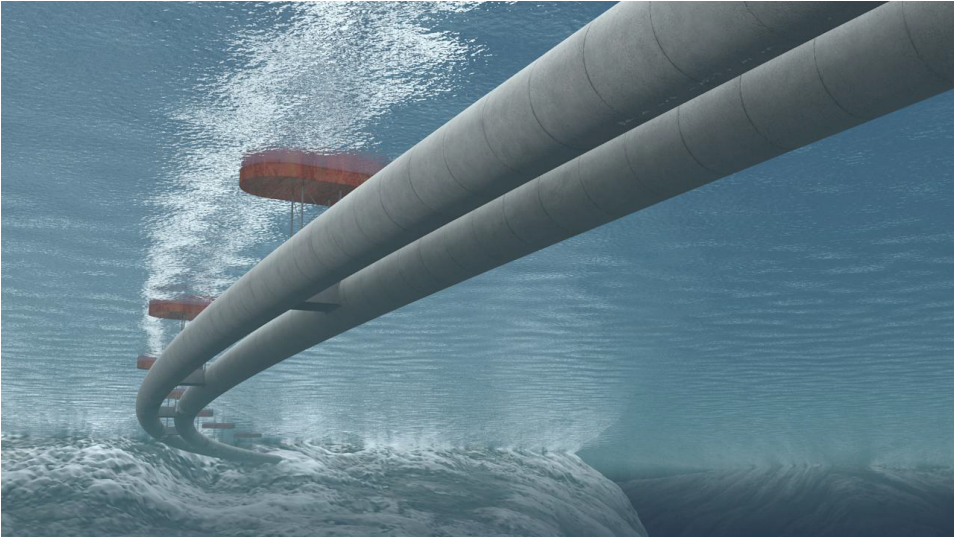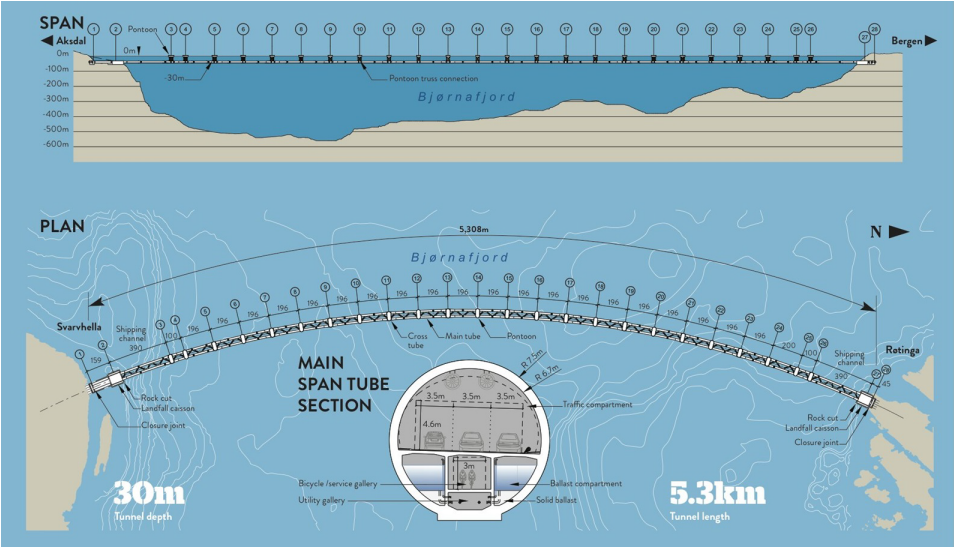
(a) Illustration

(b) Design

Figure 1.5: Submerged floating tunnel:(a)Illustration, (b) Design
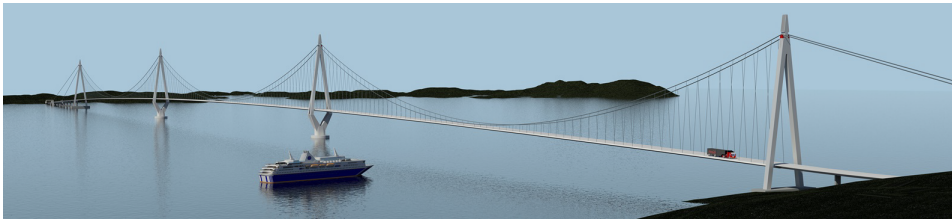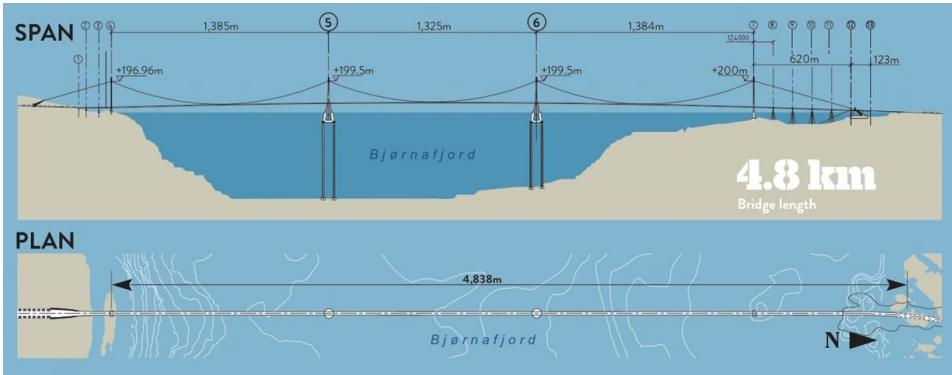
(a) Illustration

(b) Design

Figure 1.6: Multi-span suspension bridge supported by TLP:(a)Illustration, (b) Design

1.2.3 Environmental Conditions

The environmental conditions in Bjørnafjorden are combined with wind and waves. Both wind and waves with directions are taken into account. The bridge experiences various forces due to the combinations of wind and waves. To obtain the rational results of the dynamic response, proper environmental conditions should be computed. In this thesis, the wave conditions will be focused on.

Wind Wave

The 100-years wind wave conditions are displayed in Table.1.2 as below. The estimates are based on the simulation from [14]. The direction $0°$ is waves coming from the north, $90°$ shows waves from east, $180°$ means waves from south, and $270°$ is west. In this estimation, wave conditions are constant within each sector.

Table 1.2: 100-years wind waves in Bjørnafjorden

Sectors	H_s[m]	T_p[s]
$345° - 75°$	1.5	5.0
$75° - 105°$	2.8	6.6
$105° - 165°$	1.6	5.3
$165° - 225°$	1.9	5.3
$225° - 315°$	2.4	5.9
$315° - 335°$	2.5	6.2
$335° - 345°$	2.0	5.6

Wind Condition

The simulation and analysis implemented by Kjeller vindteknikk give the wind condition information. The 1-hour mean wind speed at 10-meter height is 29.5 m/s for a 100-years return period. The Statens vegvesen[14] provides the wind data shown in Table.1.3.

Table 1.3: 100-years wind conditions in Bjørnafjorden

Sectors	U_w[m/s]
$0° - 75°$	20.65
$75° - 225°$	25.08
$225° - 255°$	26.55
$255° - 285°$	29.50
$285° - 345°$	26.55
$345° - 360°$	20.65

Swell

The 100-years swell information is shown in Table.1.4. There are two types of swell at the same direction. For both directions in $205°$ and $320°$, the swell has $0.4m$ significant wave height with 12-16 s peak period while the other swell has 0.2 m significant wave height with 17-20 s peak period.

Table 1.4: 100-years swells in Bjørnafjorden

Directions	H_s[m]	T_p[s]
$205°$	0.4	12-16
$205°$	0.2	17-20
$320°$	0.4	12-16
$320°$	0.2	17-20

1.2.4 Inhomogeneous Wave Field

Since the initial design of the end-anchored floating bridge is under the assumption of homogeneous wave conditions, the uncertainty of inhomogeneity should be considered. Regarding one point along the fjord, the wave elevations there will be affected strongly by many other points nearby and slightly to an extent by distant points. If the difference between phase angle is constant and the amplitudes at any two points are zero for any frequency component in the fjords, then the wave field are regarded as homogeneous; otherwise, it is considered inhomogeneous. Lacking data leads to that the homogeneous wave field was selected before. Due to the complicated topography of the seafloor in Bjørnafjorden, the wave field is supposed to be inhomogeneous. To find out the characters of wave conditions in Bjørnafjorden, NPRA has developed three DWRs (Datawell Directional Wave Riders) to collect the wave elevations and wave direction. The locations of three DWR are shown in Fig.1.7.
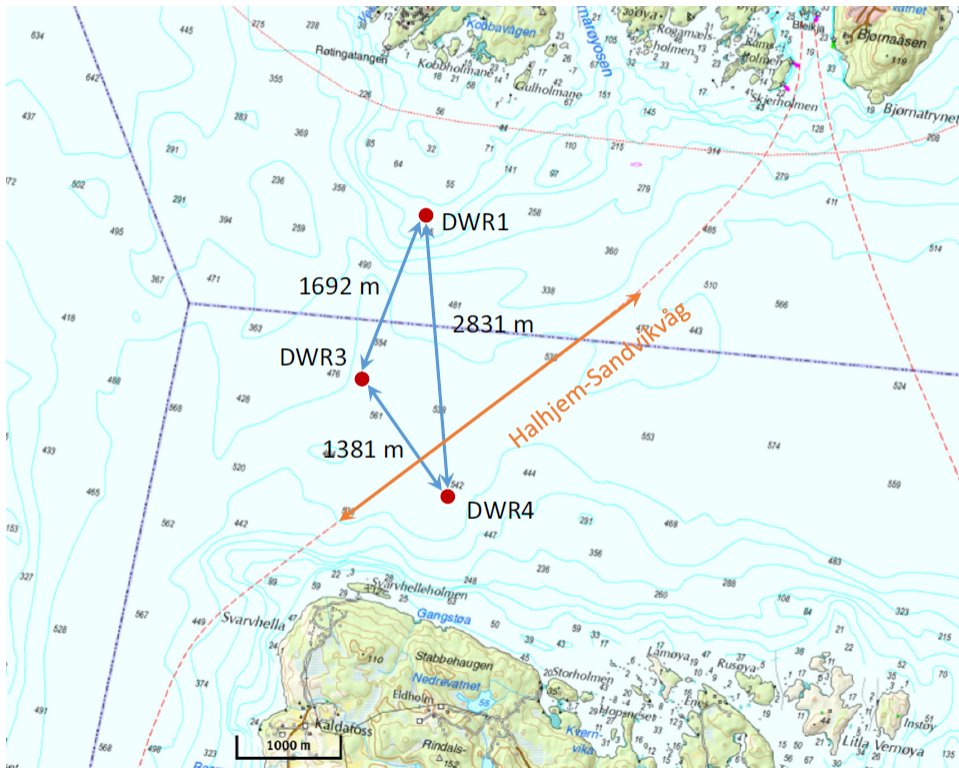
Figure 1.7: Three DWR locations in Bjørnafjorden

The results from Cheng .et al [6] shows the inhomogeneity of the wave conditions in Bjørnafjorden. The significant wave height, peak period, and wave directions at three DWRs' locations are displayed in Table.1.5. The recorded largest significant wave heights at DWR4, DWR3, DWR1 are $1.1m$, $1.12m$, and $1.22m$ respectively which indicates that

the wave conditions are harsher at the location of DWR1 than the location of the other two DWRs. The locations of DWR4, DWR3, and DWR1 are approximately corresponding to the locations of pontoon PonA3, PonA9 and PonA17 respectively which are marked in design diagrammatic drawing, Fig.1.4.

Table 1.5: The characters of wave conditions at DWRs' locations

	H_s[m]	T_p [s]	θ_p [deg]
DWR4 (PonA3)	1.1	3.77	312
DWR3 (PonA9)	1.12	3.77	305
DWR1 (PonA17)	1.22	3.77	288

1.3 End-anchored Curved Floating Bridge

COWI has developed a technical report [8] which indicates that it is feasible to design a floating bridge structure for the crossing of Bjørnafjorden. The design and components of the floating bridge will be introduced briefly in this section. The span of the whole floating bridge is sketched in Fig.1.8 where there are two main parts, high bridge, and pontoon-supported bridge. In this study, both parts of the floating bridge are modeled with rigid pontoons. The cables are modeled by applying bar elements and beam elements are used for the tower and girder of the bridge.
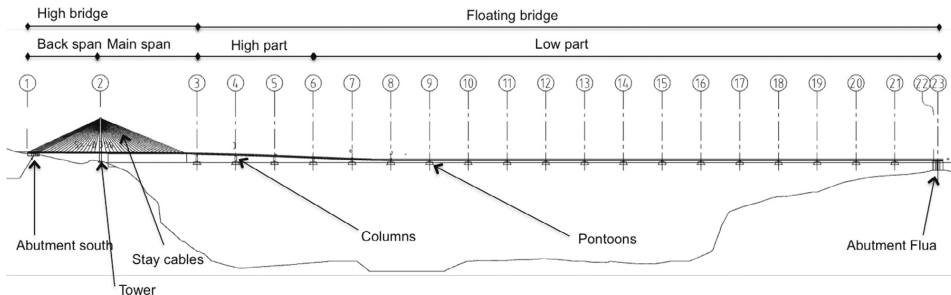
Figure 1.8: Span of the floating bridge

1.3.1 High Bridge

The cable-stayed bridge is located at the south of Bjørnafjorden from axis 1 to axis 3 which has a main span of 450m between axis 2 to axis 3 to provide a required navigation channel. The southern abutment is set up on axis 1 and the tower is built on axis 2.

1.3.2 Pontoon-supported Floating Bridge

The length of the pontoon-supported floating bridge section is about 3700 m and 19 pontoons are set up located on axis 3 to axis 21 and ends on the northern abutment on axis 23.

1.3.3 Design of Pontoons

The low part of the floating bridge is supported by 19 pontoons which are designed with a length of 28 meters, a width of 68 meters, and height of 14 meters. COWI et al. carried out this design of the pontoon. The diagrammatic graph of the design of the pontoon with its dimensions marked is shown in Fig.1.9. The flange at the bottom of the column will provide considerable damping for reducing the heave motion, row, and pitch motion while it will give an increased added mass.
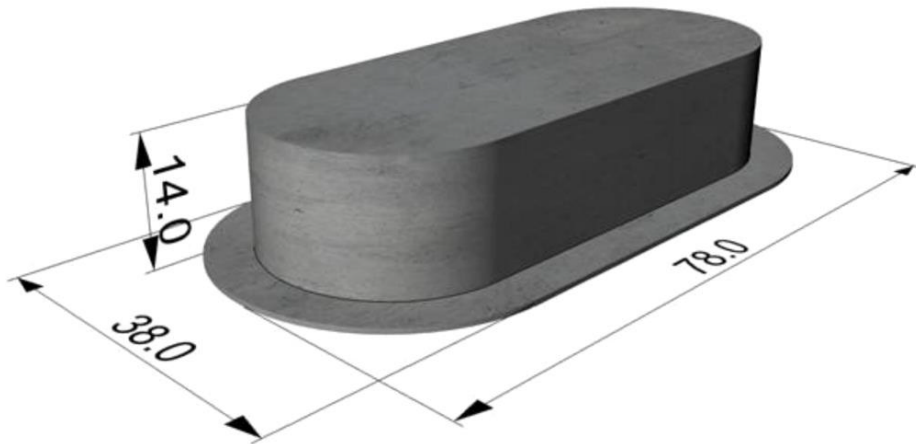
Figure 1.9: Dimensions and Design of the Pontoon

1.3.4 Global Coordinate System

The global coordinate system and orientation of the floating bridge in this study are defined and illustrated in Fig.1.10. The definition of six degree of freedoms is sketched in Fig.1.11 with the strong axis and weak axis marked.
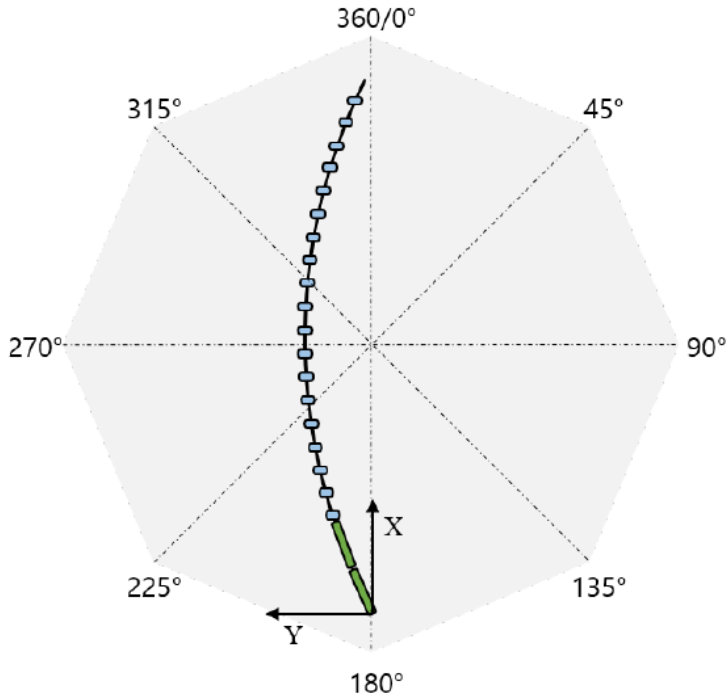
Figure 1.10: Global Coordinate and Orientation of the Floating Bridge
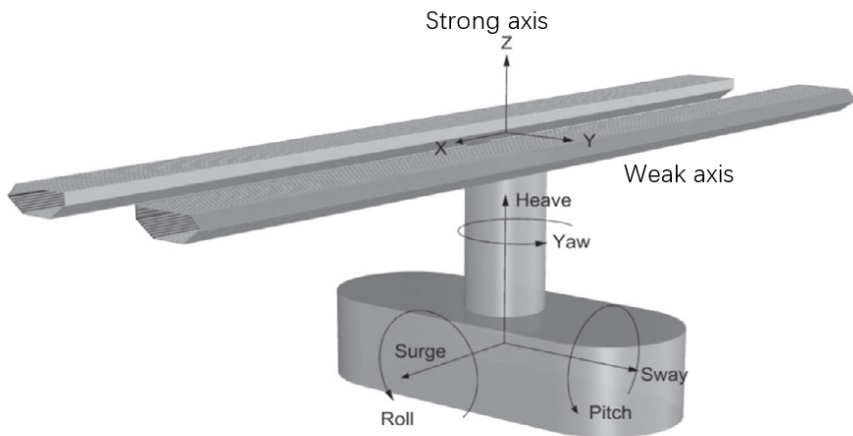
Figure 1.11: 6 DOF of the Pontoon

Chapter 2

Methods And Theories

The goal of this thesis is to investigate the methodology of simulating the inhomogeneous wave field. To compute wave elevations of several locations, the relationship between points should be researched by applying the coherence function. This work is to be done in several steps and based on stochastic theories. After the wave field is simulated, global dynamic response of the floating bridge will be computed by SIMO-RIFLEX.

The flowchart Fig.2.1 below explains the procedure applied in this study. The flowchart starts with 'Input Data' which means the significant wave height H_s [m] and peak period T_p [s] are first provided to begin the procedure. With known H_s and T_p, the Jonswap spectrum depending on frequency can be computed by (2.12). For multiple points involved case, the Jonswap spectra should be transformed into matrix form. After generating the initial wave spectrum, two methods called 'Campbell analogy' [3] and 'Cholesky decomposition' which will be introduced in the following sections are implemented to compute the transfer function matrix. Combining the transfer function matrix and the time series of Gaussian white noise will produce the new-generated time series of wave elevations. The detailed theories will be explained later. By WAFO Matlab function 'dat2spce', the Jonswap spectrum of the new-generated wave elevations can be computed. The wave characteristics of the new-generated wave spectrum are analyzed by applying spectral moments. The comparison between the input data and new obtained wave characteristics will give a visual evaluation of the methods that the smaller deviations are, the better qualities of results are.

After the wave field simulation, the newly generated wave characteristics can be applied to simulate time series of wave force which will be considered in SIMA simulation to carry out the global dynamic analyses.
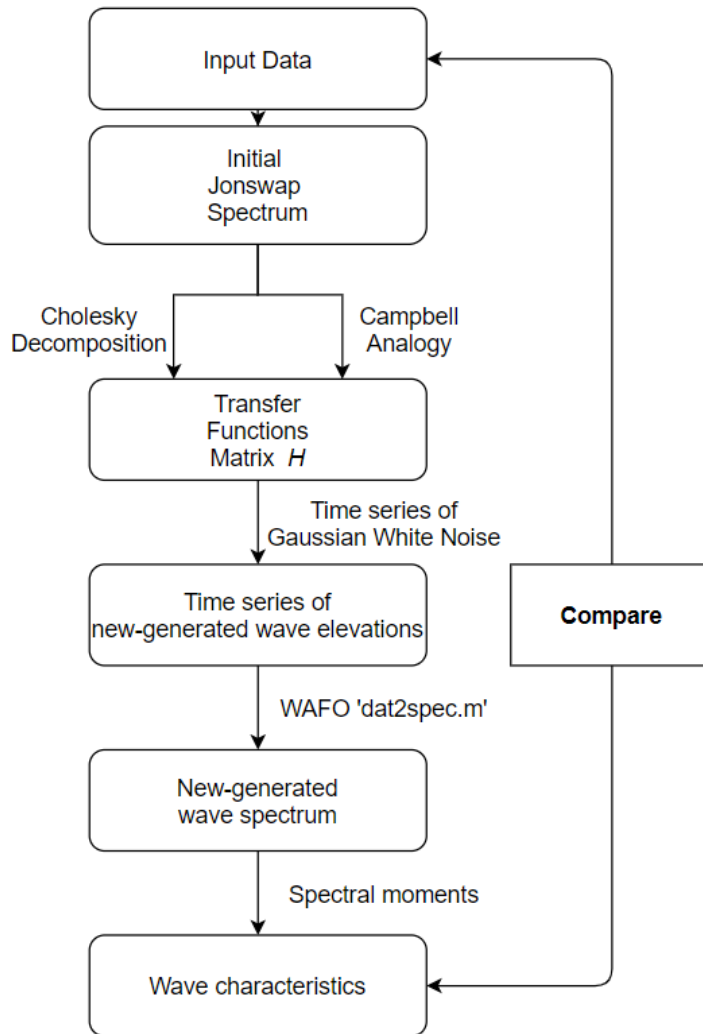
Figure 2.1: Flowchart of wave field simulation procedure

2.1 Numerical Model of the Floating Bridge in SIMO-Riflex

COWI et al. had conducted the detailed design of the floating bridge in this study. The numerical model built in SIMO-Riflex is provided by Cheng. In addition, Cheng's previous study [6] which is about the hydrodynamic loading and inhomogeneous wave field effect on the floating bridge in Bjørnafjorden is used for reference here. To simulate the response and stress condition of the wave load affected bridge, the software SIMO-Riflex which is a module in SIMA which is developed by SINTEF for hydrodynamic calculation is the essential tool in this thesis. The Riflex is a nonlinear FEM (Finite Element Method) solver while SIMO is a solver considering the various hydrodynamic loads based on potential flow theory. The model is illustrated in Fig.2.2 and is displayed in SIMA interface shown in Fig.2.3.
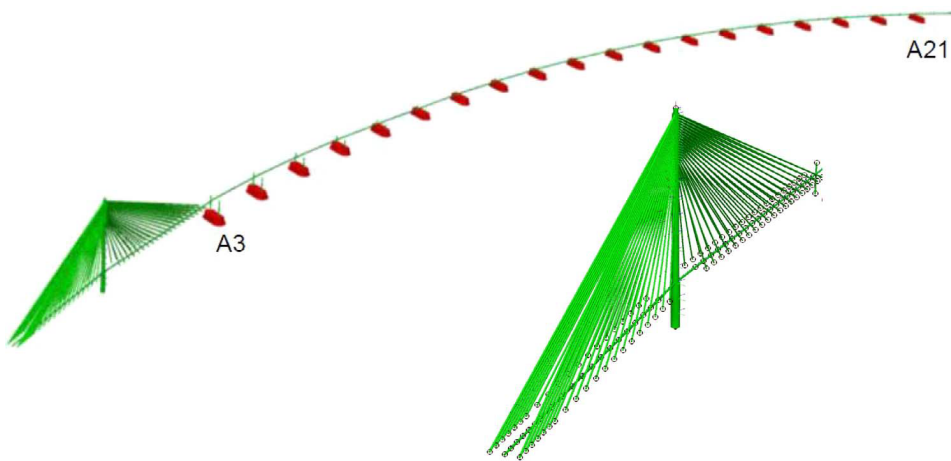
Figure 2.2: Numerical Model of Floating Bridge provided by Cheng [4]
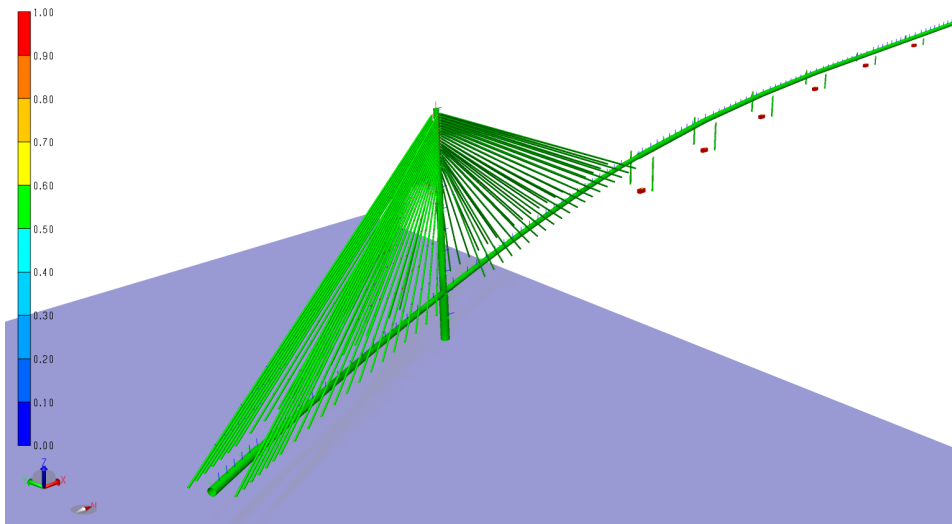
Figure 2.3: Model of Floating Bridge Displayed in SIMA

2.2 Stochastic Theories

Many stochastic theories will be applied in this study from the basic to the Campbell turbulence simulation [3]. The related stochastic theories will be introduced in detail. In this section, two methods named 'Campbell analogy' and 'Cholesky decomposition' are applied to simulate the wave field. To compute the two methods, many computations of the matrix will be included.

2.2.1 Correlation Function

The wave elevations are assumed to be a stochastic process since we only know part of the wave and it occurs randomly. To compute the correlation function, the stochastic process should be ergodic. Ergodicity indicates the properties of one realization from the stochastic process can represent the general stochastic properties. To reach ergodicity, the stochastic process must be strong stationary which indicates the joint probability function only depends on the time difference instead of absolute time.

Auto-correlation Function

The auto-correlation function for a random process $x(t)$ is defined as the average value of the product $x(t)x(t + \tau)$:

$$R_x(\tau) = E[x(t)x(t + \tau)] \tag{2.1}$$

where the $R_x(\tau)$ is the auto-correlation function for x(t). The mean and standard deviation will be independent of t, so that:

$$E[x(t)] = E[x(t + \tau)] = m$$

$$\sigma_{x(t)} = \sigma_{x(t+\tau)} = \sigma$$

The correlation coefficient for $x(t)$ and $x(t)x(t + \tau)$ is defined by:

$$\rho = \frac{E[x(t) - mx(t + \tau) - m]}{\sigma^2} = \frac{R_x(\tau) - m^2}{\sigma^2} \tag{2.2}$$

Hence $R_x(\tau) = \sigma^2\rho + m^2$ and the limit of ρ are 1 and -1.
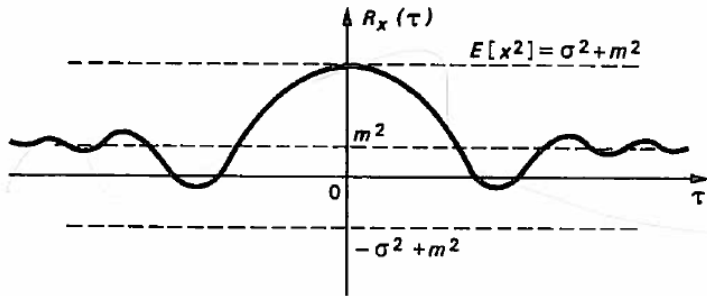
Figure 2.4: Example of Auto-correlation Function

Cross-correlation Function

The cross-correlation functions between two different stationary random functions of time x(t) and y(t) are defined as:

$$R_{xy}(\tau) = E[x(t)y(t+\tau)]$$
$$R_{yx}(\tau) = E[y(t)x(t+\tau)]$$
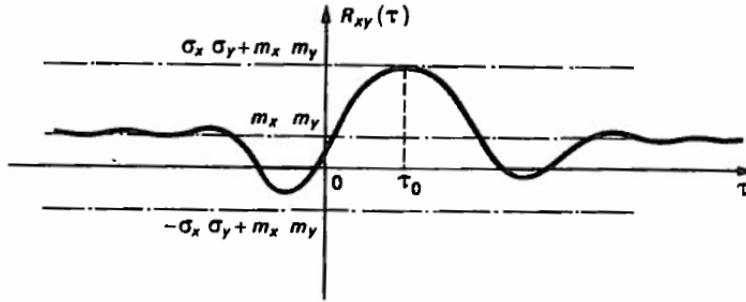
Figure 2.5: Example of Cross-correlation Function

2.2.2 Spectral Density Function

By using Fourier transform of $R_x(\tau)$, and its inverse, are given by:

$$S_x(\omega) = \frac{1}{2\pi} \int_{-\infty}^{\infty} R_x \tau e^{-i\omega\tau} d\tau$$

and

$$R_x(\omega) = \int_{-\infty}^{\infty} S_x \omega e^{-i\omega\tau} d\omega$$

Then the cross spectrum can be defined as:

$$S_{xy}(\omega) = \frac{1}{2\pi} \int_{-\infty}^{\infty} R_{xy} \tau e^{-i\omega\tau} d\tau$$

$$R_{xy}(\omega) = \int_{-\infty}^{\infty} S_{xy} \omega e^{-i\omega\tau} d\omega$$

$$S_{yx}(\omega) = \frac{1}{2\pi} \int_{-\infty}^{\infty} R_{yx} \tau e^{-i\omega\tau} d\tau$$

$$R_{yx}(\omega) = \int_{-\infty}^{\infty} S_{yx} \omega e^{-i\omega\tau} d\omega$$

A spectral representation of stochastic processes requires that the process can be decomposed into harmonic components with stochastic amplitude and phase.
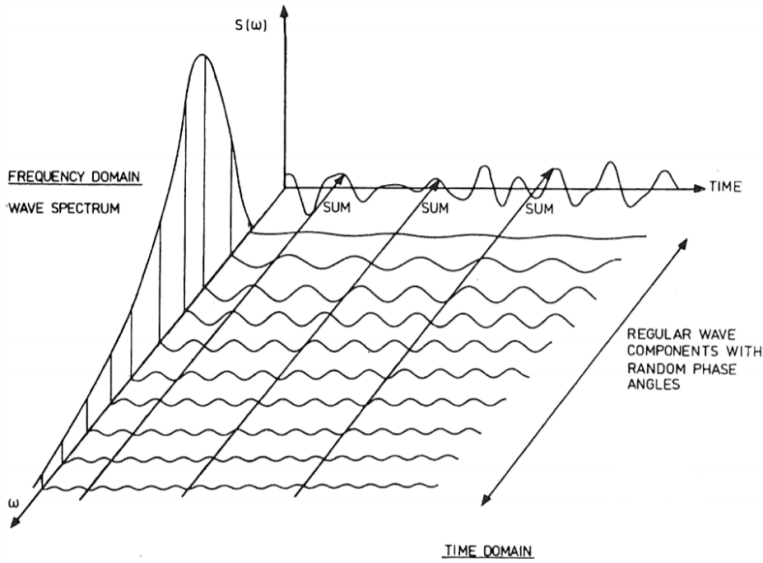
Figure 2.6: Spectrum composed by time series

The corresponding wave elevation at certain frequency is given by:

$$\zeta_a(\omega_n) = \sqrt{2S_\zeta(\omega_n)\Delta\omega} \tag{2.3}$$

$$\zeta(\omega_n, t) = \zeta_a sin(\omega_n t + \phi) \tag{2.4}$$

The phase angle ϕ between each time series is randomly generated between $[0, 2\pi]$. Hence if we have the spectrum for a series of wave at single location, we can compute the time series by linear superposition method.

$$\zeta(t) = \sum_{i=1}^{n} \zeta_a cos(\omega_i t + \phi_i) \tag{2.5}$$

2.2.3 Directional Wave Spectrum

The directional wave spectrum is commonly modeled by:

$$S(f,\theta) = S(f)D(f,\theta)$$

Where S(f) is classical one-sided spectrum and $D(f,\theta)$ is directional spreading function with properties that $D(f,\theta) >= 0$ when θ in $[0,2\pi]$ and the integration on $[0,2\pi]$ is 1. The

$D(f, \theta)$ is give by:

$$\int_0^{2\pi} D(f, \theta) d\theta = 1$$

Since the 3-hour sea state can be regarded as a stationary and Gaussian distributed, the elevation of the short-crested irregular waves at points (x, y) can be expressed as the sum of the wave components in all directions [10]:

$$\zeta(x, y, t) = \Re \left\{ \sum_{n=1}^{N} \sum_{m=1}^{M} \zeta_a(\omega_n, \theta_m) exp(i(\omega_n t - k_n x cos(\theta_m) - k_n y sin(\theta_m) + \epsilon_{nm})) \right\} \tag{2.6}$$

where,

$$\zeta_a(\omega_n, \theta_m) = \sqrt{2S_\zeta(\omega_n, \theta_m)\Delta\omega_n\Delta\theta_m} \tag{2.7}$$

where x and y indicate the location of a pontoon in the global coordinate system and t is time. $\zeta_a(\omega_n, \theta_m)$ is the wave amplitude as a function of wave frequency ω and wave direction θ. $S_\zeta(\omega_n, \theta_m)$ denotes the wave spectrum including directional variations expressed in N and M are the total number of wave frequencies and wave directions, and k is the related wave number. ϵ represents arbitrary phase angles uniformly distributed between 0 to 2π.

2.2.4 Spectral Moments

The spectral moment method is used to characterize the spectrum energy in the frequency domain. The spectral moments can be applied to compute the characters of wave elevations from the spectral density. The function of spectral moments is given by:

$$m_i = \int_{-\infty}^{\infty} \omega^i S(\omega) d\omega \tag{2.8}$$

where m_i is the i-th spectral moment and i could be 0,2,4 ... The essential characters of wave elevations, significant wave height and mean wave period, can be computed and the functions are given by:

$$H_s = 4\sqrt{m_0} \tag{2.9}$$

$$T_0 = \sqrt{\frac{m_0}{m_2}} \tag{2.10}$$

where the H_s is the significant wave height and T_0 is the mean wave period. Note that the definition of significant wave height here is about 5 percent larger than the significant wave height from 'the mean of the one third largest waves in the sea'. Here the zero up-crossing wave period T_z is the same as the mean wave period. The formula (2.11) below is to find the relationship between the mean wave period and the wave peak period.

$$T_p = (0.6673 + 0.05037 * \gamma - 0.00623 * \gamma^2 + 0.0003341 * \gamma^3) * T_z \tag{2.11}$$

By combing both formulas (2.9) and (2.11), the wave peak period can be computed. Formulas from DNV-RP-C205 [9] are used to find the zero up crossing period for JONSWAP with given Tp and gamma.

2.2.5 JONSWAP Spectrum

In this study, the JONSWAP spectrum is implemented to match the short term simulation of wave condition. The JONSWAP spectrum is formulated as a modification of the Pierson-Moskowitz spectrum for a developing sea state in a fetch limited situation. The JONSWAP spectrum is computed by (2.12):

$$S_{JONSWAP}(\omega) = A_\gamma \frac{5}{16} H_s^2 \omega_p^4 \omega^{-5} exp\left(-\frac{5}{4}\left(\frac{\omega}{\omega_p}\right)^{-4}\right)\gamma^{exp\left(-0.5(\frac{\omega-\omega_p}{\sigma\omega_p})^2\right)} \quad (2.12)$$

where,

$$A_\gamma = 1 - 0.287 ln(\gamma) \quad (2.13)$$

$$\omega_p = \frac{2\pi}{T_p} \quad (2.14)$$

$$\sigma = \begin{cases} 0.07 & for \quad \omega < \omega_p \\ 0.09 & for \quad \omega \geq \omega_p \end{cases} \quad (2.15)$$

For $\gamma = 1$ the JONSWAP spectrum reduces to the Pierson-Moskowitz spectrum. Where Tp is peak period in seconds and Hs is the significant wave height in meters, and should be used with caution outside this interval. A_γ is the normalizing factor as a function of $gamma$. The spectral width parameter σ can be emploied with $\sigma_a = 0.07$ and $\sigma_a = 0.07$ when for $\omega \leq \omega_p$ and for $\omega > \omega_p$ respectively. The JONSWAP spectrum is expected to be a reasonable model for $3.6 < \frac{T_p}{\sqrt{H_s}} < 5$. If no particular values are given for the peak shape parameter γ, the following value may be applied:

$$\gamma = \begin{cases} 5 & for \quad \frac{T_p}{\sqrt{H_s}} \leq 3.6 \\ exp\left(5.75 - 1.15\frac{T_p}{\sqrt{H_s}}\right) & for \quad 3.6 < \frac{T_p}{\sqrt{H_s}} < 5 \\ 1 & for \quad 5 \leq \frac{T_p}{\sqrt{H_s}} \end{cases} \quad (2.16)$$

2.2.6 Coherence Function

The coherence function between two time series of waves is defined as:

$$Coh_{xy}(\omega) = \sqrt{\frac{|S_{xy}(\omega)|^2}{S_{xx}(\omega)S_{yy}(\omega)}} \quad (2.17)$$

where $S_{xy}(\omega)$ is the cross-spectral density function between two time series $x(t)$ and $y(t)$. $S_{xx}(\omega)$ and $S_{yy}(\omega)$ is the spectral density of $x(t)$ and $y(t)$ respectively. For two completely same time signals $x(t)$ and $y(t)$, the coherence will be constant 1. In this study, the concept of coherence function $Coh(\omega, r)$ which depends on both frequency ω and separated distance r between two points.

From Chengs' work [7] which focused on the analysis of collected wave field data along Bjørnafjorden, the coherence functions between the three DWRs are obtained. The distances among the three DWRs are from 1381 meters to 2831 meters which contain obvious gaps. The results of each combination of two pontoons are presented below in Fig.2.7, Fig.2.8 and Fig.2.9 respectively. The analyses are based on the collected short-term data with the highest significant wave height H_s. The results from analyzed collected data are interesting. In theory, the farther the distance is, the lower the coherence is. But in practice, the three combinations between DWRs lead to similar results. The mean value of coherence for three combinations is all around 0.2 which can be regarded as a low dependency. Another conclusion can be drawn that there is no specific functional relationship between coherence and frequency.
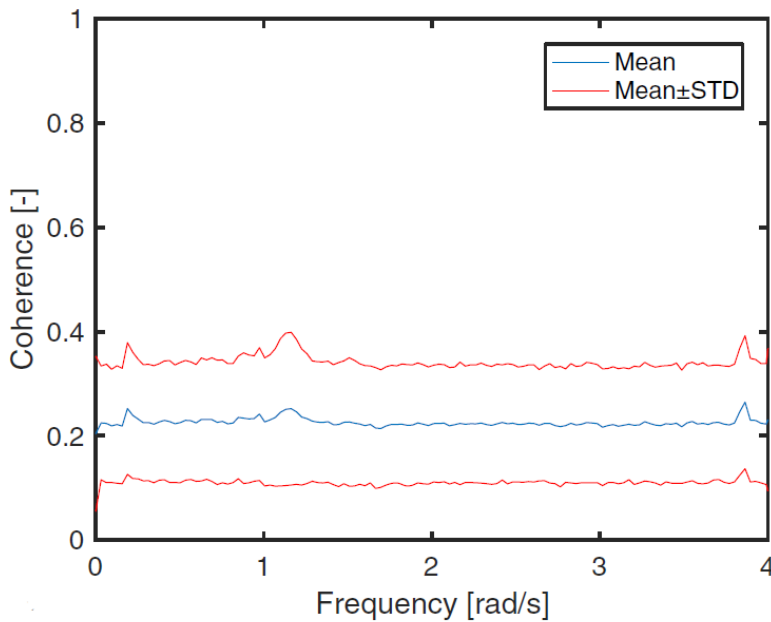
Figure 2.7: Coh_{13}, the mean value and STD of coherence between DWR 1 and DWR 3
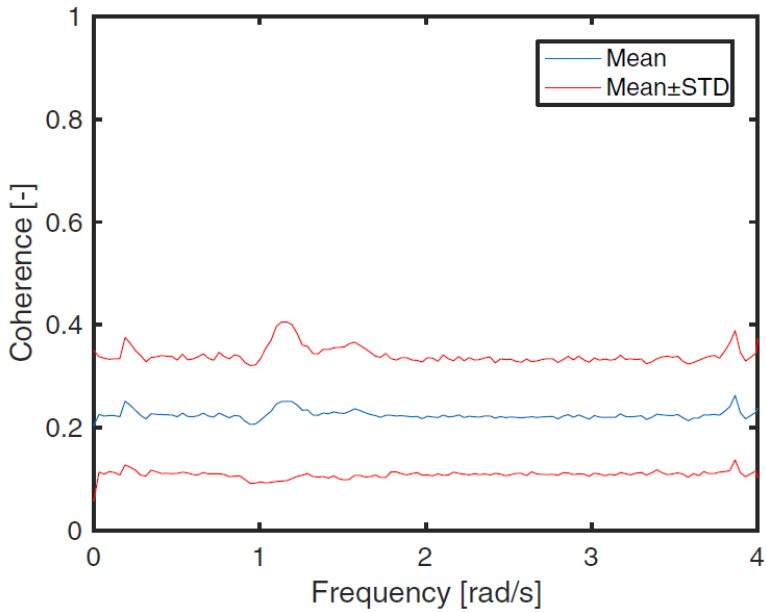
Figure 2.8: Coh_{14}, the mean value and STD of coherence between DWR 1 and DWR 4
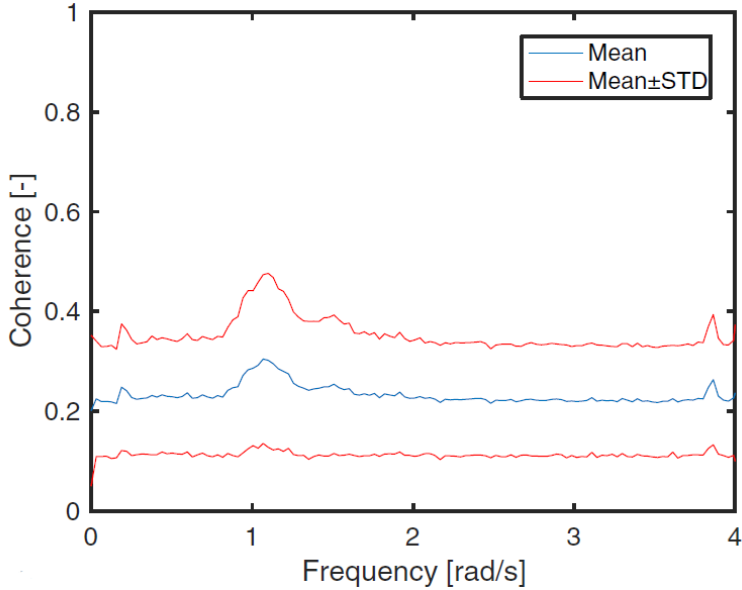
Figure 2.9: Coh_{34}, the mean value and STD of coherence between DWR 3 and DWR 4

The most reasonable method to determine the coherence function is to set up DWR at each point where there is a pontoon but it consumes too much money and time. In this study, the coherence function is assumed to decay as an exponential function depending on separated distance from the proposed first pontoon Pon A3 to the current pontoon. Since the mean value of coherence is around 0.2 between the three DWRs and the distances are from 1381 meters to 2831 meters, it is rational to suppose a function with its value will be about 0.2 in the domain from 1000 to 3000. According to experience, the decay function is conducted with an exponential decay coefficient. The exponent part of the coherence function can be discussed. The function should be monotonic and decrease slower at the coherence value reaching about 0.2 than the beginning. To meet that demand, $e^{(-ax^{1/b})}$ is introduced. The 'a' controls the location of the curve while the 'b' is in charge of the trend of the curve. In this study, the function $e^{(-0.6x^{1/8})}$ shown in Fig.2.10 is used in this study. The red '*' represent the mean coherence value of collected data at certain distances which fit the assumed coherence function. In fact, the coherence function of collected data fluctuates around a certain value and varies depending on the frequency. But in this thesis, for each location away from the position of first pontoon Pon A3, the coherence will be a constant number with respect to frequency.
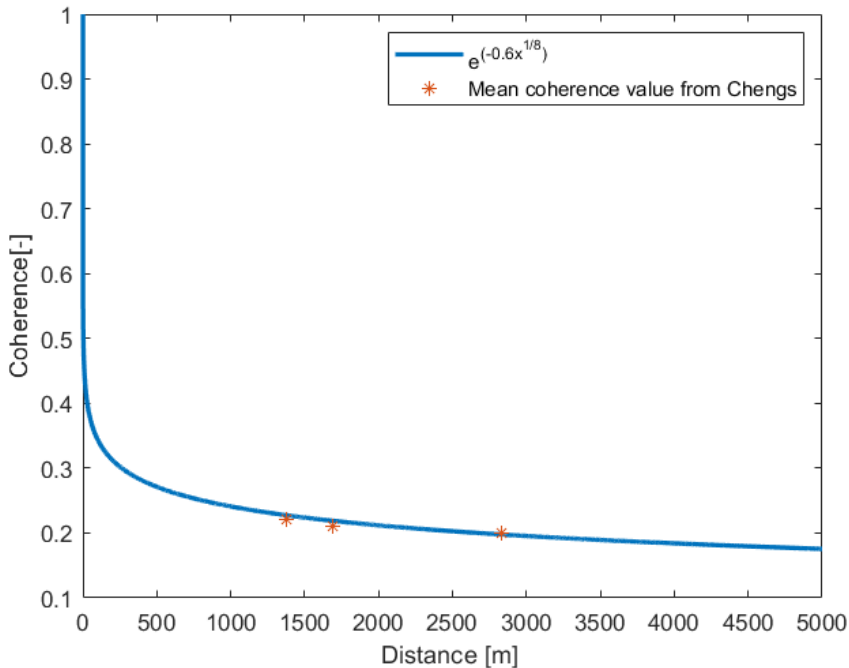
Figure 2.10: Assumed coherence function

2.3 Monte Carlo Turbulence Simulation

The basic theories and concepts about generating wave elevations by stochastic methods are introduced in this section. According to the technical report conducted by Campbell [3], one of the methods applied in this study is derived from the contents so that it is named 'Campbell analogy' in this thesis. Another method to generate filter functions is an application of Cholesky decomposition, therefore it is named 'Cholesky decomposition' in this thesis.

2.3.1 White Noise

In this study, Gaussian white noise with 0 mean value and unit standard deviation is considered. For the spectral density of Gaussian white noise, the spectrum is regarded as constant 1. The Gaussian white noise is defined as a stationary and ergodic random process with zero mean and follows the principle:' any two values of Gaussian white noise are statistically independent no matter how close they are in time.'

From (2.5), the time series of Gaussian white noise is shown as:

$$x(t) = \sum_{i=1}^{n} a_i cos(\omega_i t + \phi_i) = \sum_{i=1}^{n} \Re \left\{ a_i e^{i(\omega_i t + \phi_i)} \right\} \tag{2.18}$$

where the a_i represents the amplitude of the Gaussian white noise at frequency ω_i. The a_i is obtained by (2.19).

$$a_i = \sqrt{2 S_{xx}(\omega_i) \Delta \omega} \tag{2.19}$$

Where the $S_{xx}(\omega)$ represents the spectral density function depending on frequency. The ϕ_i is the phase angle of white noise at certain frequency. The phase angle is randomly distributed between $[0, 2\pi]$

2.3.2 Filter Function

Gaussian white noise is filtered by a linear filter whose filter function is chosen so that the spectrum of the output signal is the desired spectrum of turbulence. Because the filter is linear, the output signal is Gaussian distributed. The concept of filter function is described by Fig2.11. Many different approaches may be used to achieve the simulated turbulence.
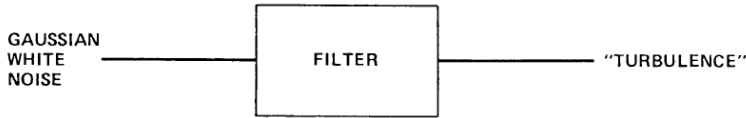
Figure 2.11: Monte Carlo turbulence simulation

The filter function for time series can be expressed as a transfer function in (2.20) which contains a RAO (Response Amplification Operator) term and phase angle term:

$$H(\omega_i) = |H(\omega_i)| e^{\beta_i} \tag{2.20}$$

where ω_i represents a certain frequency, $H(\omega_i)$ is the filter function and β_i is the phase angle which is randomly distributed between $[0, 2\pi]$. By multiplying filter function with white noise and take the real part of it since the filter function is complex, then the time series can be obtained:

$$Y(\omega) = \Re\{H(\omega)X(\omega)\} = \Re\{|H(\omega)|e^{\beta_i}X(\omega)\} \tag{2.21}$$

where $Y(\omega)$ is the spectrum of time series. $X(\omega)$ is the spectral density function of white noise which is constant 1. Filter function here does not take the influence of the location the fjord into consideration. Since the value of filter function varies along the fjord, the relationship between the location and the filter function will be studied in later sections.

To generate the time series, decomposing the spectrum which is mentioned before is needed. By multiplying the filter function (2.20) with Gaussian white noise. (2.18) :

$$\begin{aligned} x(t) &= \sum_{i=1}^{n} \Re\left\{|H(\omega_i)|a_i e^{i(\omega_i t + \phi_i + \beta(\omega_i))}\right\} \\ &= \sum_{i=1}^{n} |H(\omega_i)|a_i cos(\omega_i t + \phi_i + \beta(\omega_i)) \end{aligned} \tag{2.22}$$

2.3.3 Monte Carlo Simulation For Stochastic Process

For a known stochastic process X, we have its CDF(Cumulative Distribution Function) given as below:
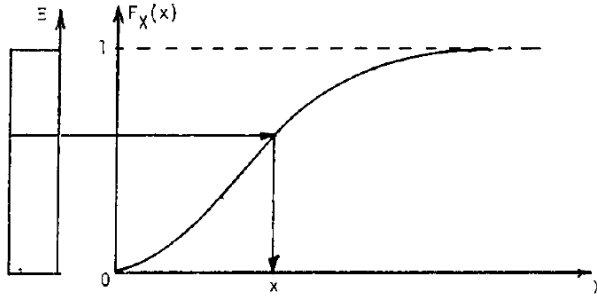
Figure 2.12: Cumulative Distribution Function for X

For each x, there is a corresponding y which is defined as:

$$y = G(x)$$

$$x = G^{-1}(y)$$

The Monte Carlo method is to generate a series of variable u which represent the probability of process x.

Value, X	x_1	x_2	x_3	......	x_n
Probability	p_1	p_2	p_3	.....	p_n

Figure 2.13: Probability mass for X

Then for each x, y value shares the same probability. Hence we could drive the CDF for value y. We could regard the X as wave elevation depending on time and Y will be the motion of the structure. Once we have the transfer function (equation of motion) between the elevation and amplitude of motion, we could compute the distribution of the motion. Monte Carlo method will be applied regarding that each amplitude in Gaussian white noise does correspond to an amplitude of generated wave elevations. The thinking of Monte Carlo simulation is going to be implemented during the wave elevation simulation.

2.3.4 Two and Three Points Turbulence Simulation by Campbell Analogy

The problem addressed in this section is to generate many time series with known spectrum and cross-spectrum. The matrix form of filter functions will be developed for two series and three series by applying the Campbell's theory [3].

Two-point Case

The two series problem is sketched in Fig 2.14. The indicated filter functions are unknown, i.e. $H_1(\omega)$, $H_{12}(\omega)$, and $H_2(\omega)$. These are to be found in terms of S_{11}, S_{12}, and S_{22}, which are known quantities. Assuming that the Gaussian white noise inputs,x_1 and x_2, are independent and have unit variance, the three spectra are given by the following equations:

$$
\begin{aligned}
S_{11} &= |H_1(\omega)|^2 * S_{x_1 x_1} = |H_1(\omega)|^2 \\
S_{12} &= |H_{12}(\omega)|S_{11} \\
S_{22} &= |S_{12}|^2/S_{11} + |H_2(\omega)|^2 * S_{x_2 x_2} = |S_{12}|^2/S_{11} + |H_2(\omega)|^2
\end{aligned}
\tag{2.23}
$$

The white noise gives constant spectrum indicated in (2.24) which explains the $S_{x_i x_i}$ disappeared in formula (2.23). Note that $S_{x_i x_i} = 1$ will be conducted in following sections.

$$
\begin{aligned}
S_{x_1 x_1} &= 1 = const. \\
S_{x_2 x_2} &= 1 = const.
\end{aligned}
\tag{2.24}
$$

Then the $|H_2|^2$ is derived:

$$
|H_2|^2 = S_{22} - |S_{12}|^2/S_{11} = S_{22}(1 - coh_{12}(\omega))
\tag{2.25}
$$

where the coh_{12} represents the coherence function between point 1 and point 2.
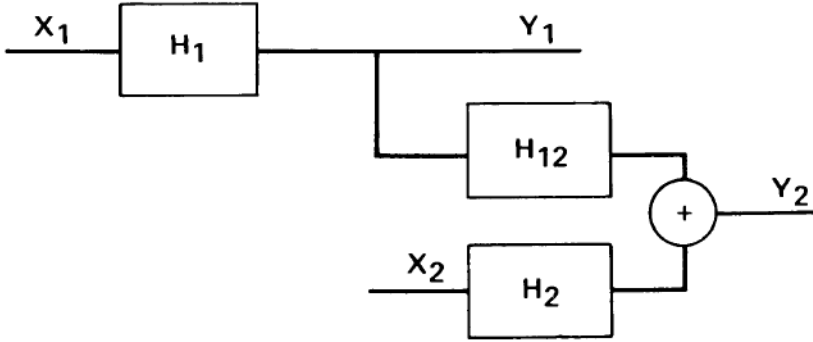
Figure 2.14: Block diagram for generating two correlated time series

The congruent relationship in flow chart shown in Fig.**??** is explained in (2.26).

$$
\begin{array}{ccccccc}
x_1 & \rightarrow & H_1 & \rightarrow & y_1 & & \\
x_1 & \rightarrow & H_1 & \rightarrow & H_{12} & \rightarrow & y_2 \\
x_2 & \rightarrow & H_2 & \rightarrow & y_2 & & \\
x_2 & \rightarrow & 0 & \rightarrow & y_1 & &
\end{array}
\tag{2.26}
$$

With computed filter function, the time series can be generated regarding (2.22). The wave elevations at point 1 are obtained by (2.27):

$$
\begin{aligned}
y_1(t) &= \sum_{i=1}^{n} \Re \left\{ |H_1(\omega_i)||x_1(t)|e^{i(\omega_i t + \phi_{1i} + \beta_1(\omega_i))} \right\} \\
&= \sum_{i=1}^{n} |H_1(\omega_i)||x_1(t)|cos(\omega_i t + \phi_{1i} + \beta_1(\omega_i))
\end{aligned}
\tag{2.27}
$$

where the $|x_1(t)|$ represents the amplitude of the white noise which can be computed by:

$$
|x_1(t)| = \sqrt{2S_{x_1 x_1}(\omega)\Delta\omega}
\tag{2.28}
$$

where the $S_{x_1 x_1}(\omega)$ is the spectrum function of Gaussian white noise at point 1 which is constant 1. The wave elevations at point 2 are obtained by (2.29):

$$
\begin{aligned}
y_2(t) &= \sum_{i=1}^{n} \Re \left\{ |H_1(\omega_i)||H_{12}(\omega_i)||x_1(t)|e^{i(\omega_i t + \phi_{1i} + \beta_1(\omega_i))} \right\} \\
&+ \sum_{i=1}^{n} \Re \left\{ |H_2(\omega_i)||x_2(t)|e^{i(\omega_i t + \phi_{2i} + \beta_2(\omega_i))} \right\} \\
&= \sum_{i=1}^{n} |H_1(\omega_i)||H_{12}(\omega_i)||x_1(t)|cos(\omega_i t + \phi_i + \beta_1(\omega_i)) + \\
&+ \sum_{i=1}^{n} |H_2(\omega_i)||x_2(t)|cos(\omega_i t + \phi_{2i} + \beta_2(\omega_i))
\end{aligned}
\tag{2.29}
$$

Where the $|x_i(t)|$ indicates the amplitude of white noise. The phase angles, β_i , from the filter functions which are depending on both locations and frequency. The relationship of locations will be explained by the coherence function.

Three-point Case

The block diagram for generating three correlated time series is shown as below:
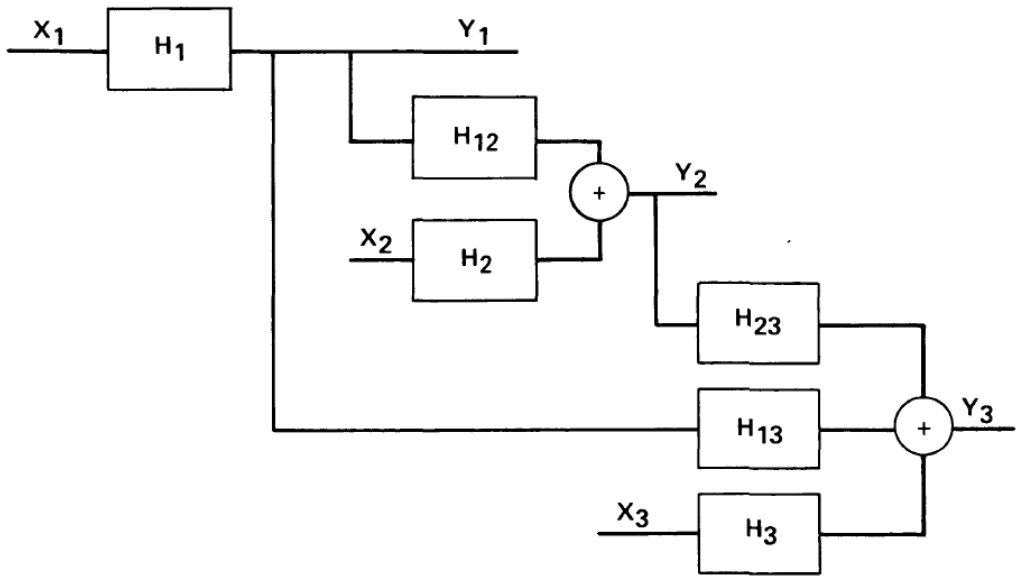
Figure 2.15: Block diagram for generating three correlated time series

The Fig. 2.15 depicts the block diagram for the three-point time series case. In the figure all information flows from top to bottom, i.e., y_1 influences y_2 and y_3, and y_2 influences y_3, but y_1 is not affected by y_2 or y_3 and so on. The one-way flow of information means that values of H_1, H_{12}, and H_2 keep the same form that they had in the two signal case and was as given in two series problem. For the three signal case, only solutions of H_{13}, H_{23}, and H_3 must be obtained. The flow chart Fig.2.15 is explained in (2.30) for a

clear look. The filter functions are shown below in (2.31).

$$
\begin{aligned}
x_1 &\rightarrow H_1 \rightarrow y_1 \\
x_1 &\rightarrow H_1 \rightarrow H_{12} \rightarrow y_2 \\
x_2 &\rightarrow H_2 \rightarrow y_2 \\
x_2 &\rightarrow 0 \rightarrow y_1 \\
x_2 &\rightarrow H_2 \rightarrow H_{23} \rightarrow y_3 \\
x_3 &\rightarrow 0 \rightarrow y_1 \\
x_3 &\rightarrow 0 \rightarrow y_2 \\
x_3 &\rightarrow H_3 \rightarrow y_3
\end{aligned}
\tag{2.30}
$$

$$
\begin{aligned}
H_{13} &= (S_{13}S_{22} - S_{12}S_{23})/DEL \\
H_{23} &= (S_{11}S_{23} - S_{21}S_{13})/DEL \\
H_3 &= DET[S_{ij}]/DEL \quad \textbf{where} \quad i = 1:3, \quad j = 1:3
\end{aligned}
\tag{2.31}
$$

where DET means the determinant and $DEL = S_{11}S_{22} - |S_{12}|^2$. DEL is always non-negative. For more points case, the principle can be analogical but not proved. The time series at point 3 will be obtained by:

$$
\begin{aligned}
y_3(t) &= \sum_{i=1}^{n} \Re \left\{ |H_1(\omega_i)||H_{13}(\omega_i)||x_1(t)|e^{i(\omega_i t + \phi_{1i} + \beta_1(\omega_i))} + \right\} + \\
&+ \sum_{i=1}^{n} \Re \left\{ |H_2(\omega_i)||H_{23}(\omega_i)||x_2(t)|e^{i(\omega_i t + \phi_{2i} + \beta_2(\omega_i))} + \right\} + \\
&+ \sum_{i=1}^{n} \Re \left\{ |H_3(\omega_i)||x_3(t)|e^{i(\omega_i t + \phi_{3i} + \beta_3(\omega_i))} \right\} \\
&= \sum_{i=1}^{n} |H_1(\omega_i)||H_{13}(\omega_i)||x_1(t)| cos(\omega_i t + \phi_i + \beta_1(\omega_i)) + \\
&+ \sum_{i=1}^{n} |H_2(\omega_i)||H_{23}(\omega_i)||x_2(t)| cos(\omega_i t + \phi_{2i} + \beta_2(\omega_i)) + \\
&+ \sum_{i=1}^{n} |H_3(\omega_i)||x_3(t)| cos(\omega_i t + \phi_{3i} + \beta_3(\omega_i))
\end{aligned}
\tag{2.32}
$$

2.3.5   Preparation of Wave Field Simulation For 19-point Case

According to the two-points case and three-points case, the methodology to simulate the wave field for 19 pontoons of the floating bridge can be deduced. The 19-point wave field simulation can be regarded as the reference case for all the potential cases. Additionally, the 19-point case is the simulation for the floating bridge in Bjørnafjorden.

Note that the spectrum matrix S_{ij} and coherence function matrix are employed in this section. The accomplishment of the third and subsequent filter functions can be explained by the following.

Matrix Form of Wave Spectrum

The matrix of the wave spectrum should be applied to compute the matrix of filter function promptly. The basic idea to create matrix of wave spectrum is to use vector of wave spectrum and matrix of coherence function. The vector of wave spectrum and the matrix of coherence are defined below in (2.33) and (2.34) respectively.

$$S_y = \begin{bmatrix} S_1 & S_2 & \cdots & S_{19} \end{bmatrix} \tag{2.33}$$

$$\mathbf{Coh} = \begin{bmatrix} Coh_{11} & Coh_{12} & \cdots & Coh_{1\,19} \\ Coh_{21} & Coh_{22} & \cdots & Coh_{2\,19} \\ \vdots & \vdots & \ddots & \vdots \\ Coh_{19\,1} & Coh_{19\,2} & \cdots & Coh_{19\,19} \end{bmatrix} \tag{2.34}$$

The matrix of the wave spectrum can be derived by following formula (2.35). Note here the definition of coherence function (3.1.2) should be applied. Then the matrix of wave spectrum can be used to compute the matrix of the filter function.

$$S_{yy} = \sqrt{S'_y * S_y} . * \mathbf{Coh} \tag{2.35}$$

Auto-correlated Filter Function

To create the filter function matrix, the diagonal elements are firstly focused. It can be recorded as H_i or H_{ii} which has the same meaning. Since the front points influence the latter points while the effects are not mutual so that when the i-th point is to be considered, only points from the first to i-th should be taken into account. Therefore, when computing i-th auto-correlated filter function, the size of the wave spectrum matrix is up to $i \times i$ and for this case, i is up to 19. Assuming $i = j$, the i-th filter function can be explained by

(2.36).

$$H_{ii} = \mathbf{DET}(S_{yy})/\mathbf{DEL}$$

$$= \frac{\textbf{Determinant of the wave spectrum}}{\textbf{Determinant of the wave spectrum with its last column and last line removed}}$$

$$= \frac{\textbf{DET(Spectrum matrix of size n} \times \textbf{n)}}{\textbf{DET(Spectrum matrix of size size n-1} \times \textbf{n-1)}}$$

$$= \mathbf{DET} \begin{bmatrix} S_{11} & S_{12} & \cdots & S_{1n} \\ S_{21} & S_{22} & \cdots & S_{2n} \\ \vdots & \vdots & \ddots & \vdots \\ S_{n1} & S_{n2} & \cdots & S_{nn} \end{bmatrix} \Big/ \mathbf{DET} \begin{bmatrix} S_{11} & S_{12} & \cdots & S_{1(n-1)} \\ S_{21} & S_{22} & \cdots & S_{2(n-1)} \\ \vdots & \vdots & \ddots & \vdots \\ S_{(n-1)1} & S_{(n-1)2} & \cdots & S_{(n-1)(n-1)} \end{bmatrix}$$

$$\textbf{where} \quad i = 3:19 \quad j = 3:19 \quad n = max([i,j])$$

$$(2.36)$$

Cross-correlated Filter Function

For the cross-correlated filter function H_{ij}, the method expressed in (2.37) has some differences from (2.36). The sizes of the wave spectra in numerator and denominator are the same. Note that in (2.37), $i \neq j$. Therefore, the matrix of filter function is derived.

$$H_{ij} = \frac{\textbf{Determinant of the wave spectrum with its i-th column and j-th line removed}}{\textbf{Determinant of the wave spectrum with its last column and last line removed}}$$

$$= \frac{\textbf{DET(Spectrum matrix of size n-1} \times \textbf{n-1)}}{\textbf{DET(Spectrum matrix of size size n-1} \times \textbf{n-1)}}$$

$$= \mathbf{DET} \begin{matrix} & \textbf{i-th} & \\ \begin{bmatrix} S_{11} & S_{12} & [\ ] & S_{1n} \\ S_{21} & S_{22} & [\ ] & S_{2n} \\ [\ ] & [\ ] & \ddots & [\ ] \\ S_{n1} & S_{n2} & [\ ] & S_{nn} \end{bmatrix} \end{matrix} \Big/ \mathbf{DET} \begin{bmatrix} S_{11} & S_{12} & \cdots & S_{1(n-1)} \\ S_{21} & S_{22} & \cdots & S_{2(n-1)} \\ \vdots & \vdots & \ddots & \vdots \\ S_{(n-1)1} & S_{(n-1)2} & \cdots & S_{(n-1)(n-1)} \end{bmatrix}$$

(with **j-th** labelling the third row)

$$\textbf{where} \quad i = 3:19 \quad j = 3:19 \quad n = max([i,j])$$

$$(2.37)$$

2.3.6 Campbell Analogy Method For Wave Elevations Generation For 19-point Case

The formula (2.38) to derive the wave elevation at the 19th pontoon position is deduced from the two-points and three-points analysis based on Campbell's theory [3] and the method applied here is named Campbell analogy. The Campbell analogy method will be implemented in wave field simulation at Bjørnafjorden. The expression of wave elevations at the location of the 19th pontoon is derived as an explanation here.

$$
\begin{aligned}
y_{19}(t) = & \sum_{i=1}^{n} \Re \left\{ |H_1(\omega_i)||H_{1\ 19}(\omega_i)||x_1(\omega_i)|e^{i(\omega_i t + \phi_{1i} + \beta_1(\omega_i))} \right\} + \\
& + \sum_{i=1}^{n} \Re \left\{ |H_2(\omega_i)||H_{2\ 19}(\omega_i)||x_2(\omega_i)|e^{i(\omega_i t + \phi_{2i} + \beta_2(\omega_i))} \right\} + \\
& \qquad\qquad\qquad\qquad \vdots \\
& + \sum_{i=1}^{n} \Re \left\{ |H_{19}(\omega_i)||x_{19}(\omega_i)|e^{i(\omega_i t + \phi_{19\ i} + \beta_{19}(\omega_i))} \right\} \\
= & \sum_{i=1}^{n} |H_1(\omega_i)||H_{1\ 19}(\omega_i)||x_1(\omega_i)|cos(\omega_i t + \phi_i + \beta_1(\omega_i)) + \\
& + \sum_{i=1}^{n} |H_2(\omega_i)||H_{2\ 19}(\omega_i)||x_2(\omega_i)|cos(\omega_i t + \phi_{2i} + \beta_2(\omega_i)) + \\
& \qquad\qquad\qquad\qquad \vdots \\
& + \sum_{i=1}^{n} |H_{19}(\omega_i)||x_{19}(\omega_i)|cos(\omega_i t + \phi_{19\ i} + \beta_{19}(\omega_i))
\end{aligned}
\tag{2.38}
$$

To achieve the formula in the script, each line of the lower triangular matrix of filter function should multiply the corresponding diagonal element. It is explained in (2.39) where H_{ii}^{wave} denotes the matrix of filter functions for generating multi-point wave elevations. The $x_i(t)$ and $y_i(t)$ are Gaussian white noise time series and newly generated wave elevations at positions of 19 pontoons.

$$
\begin{aligned}
y_i(t) &= H_{ii}^{wave} \times x_i(t) \\
&= \begin{bmatrix}
H_{11} & 0 & 0 & \cdots & 0 \\
H_1 H_{21} & H_{22} & 0 & \cdots & 0 \\
H_1 H_{31} & H_2 H_{32} & H_{33} & \cdots & 0 \\
\vdots & \vdots & \vdots & \ddots & 0 \\
H_1 H_{19\,1} & H_2 H_{19\,2} & H_3 H_{19\,3} & \cdots & H_{19\ 19}
\end{bmatrix}
\begin{bmatrix}
x_1(t) \\ x_2(t) \\ x_3(t) \\ \vdots \\ x_{19}(t)
\end{bmatrix}
= \begin{bmatrix}
y_1(t) \\ y_2(t) \\ y_3(t) \\ \vdots \\ y_{19}(t)
\end{bmatrix}
\end{aligned}
\tag{2.39}
$$

2.3.7 Cholesky Decomposition Method For Wave Field Simulation

The Cholesky decomposition can be explained by (2.40) where $\mathbf{A}$ represents a Hermitian positive matrix and $\mathbf{L}$ is a lower triangular matrix with diagonal elements. The Hermitian matrix is a square matrix that is equal to its conjugate transformation.

$$\mathbf{A} = \mathbf{LL}^* \tag{2.40}$$

The 'LDL' variant of Cholesky decomposition is derived by (2.41) where $\mathbf{D}$ is a diagonal matrix.

$$\mathbf{A} = \mathbf{LDL}^* \tag{2.41}$$

Two-point Simulation

The Cholesky decomposition is a less computation method compared to generating the matrix of filter function manually mention in (2.39). Taking the two-point wave field simulation as an example, the (2.23) can be transformed into the (2.42). And the (2.42) can be rewritten into (2.43).

$$
\begin{aligned}
S_{11} &= |H_1(\omega)|^2 * S_{x_1 x_1} = |H_1(\omega)|^2 \\
S_{12} &= |H_{12}(\omega)|S_{11} = |H_{12}(\omega)||H_1(\omega)|^2 \\
S_{12} &= S_{21} \\
S_{22} &= |S_{12}|^2/S_{11} + |H_2(\omega)|^2 * S_{x_2 x_2} = |S_{12}|^2/S_{11} + |H_2(\omega)|^2 \\
&= \frac{|H_{12}(\omega)|^2 S_{11}^2}{S_{11}} + |H_2(\omega)|^2 = |H_{12}(\omega)|^2|H_1(\omega)|^2 + |H_2(\omega)|^2
\end{aligned}
\tag{2.42}
$$

$$
\begin{bmatrix} S_{11} & S_{12} \\ S_{21} & S_{22} \end{bmatrix} = \begin{bmatrix} |H_1|^2 & |H_1|^2|H_{12}| \\ |H_1|^2|H_{12}| & |H_1|^2|H_{12}|^2 + |H_2|^2 \end{bmatrix} \begin{bmatrix} S_{x_1 x_1} & 0 \\ 0 & 1 S_{x_2 x_2} \end{bmatrix}
\tag{2.43}
$$

The formula (2.44) which is carried out with Cholesky decomposition and the equation (2.45) in matrix form shown below. Three components are lower triangular matrix, unit matrix, and the upper triangular matrix. The S_{xx} equals the unit matrix since the spectral density should be constantly 1 for the Gaussian white noise.

$$S_{yy} = \mathbf{L} S_{xx} \mathbf{L}^* \tag{2.44}$$

$$
\begin{bmatrix} S_{11} & S_{12} \\ S_{21} & S_{22} \end{bmatrix} = \begin{bmatrix} |H_1| & 0 \\ |H_1||H_{21}| & |H_2| \end{bmatrix} \begin{bmatrix} 1 & 0 \\ 0 & 1 \end{bmatrix} \begin{bmatrix} |H_1| & |H_1||H_{21}| \\ 0 & |H_2| \end{bmatrix}
\tag{2.45}
$$

Three-point Simulation

The three-point simulation case can be analogized from the two-point case. The formula of deducing the matrix of the spectrum is derived in (2.46) and the formula in matrix form

is shown in (2.47)

$$
\begin{aligned}
S_{11} &= |H_1(\omega)|^2 * S_{x_1 x_1} = |H_1(\omega)|^2 \\
S_{12} &= |H_{12}(\omega)|S_{11} = |H_{12}(\omega)||H_1(\omega)|^2 = S_{21} \\
S_{13} &= |H_{13}(\omega)|S_{11} = |H_{13}(\omega)||H_1(\omega)|^2 = S_{31} \\
S_{22} &= |H_{12}(\omega)|^2|H_1(\omega)|^2 + |H_2(\omega)|^2 \\
S_{32} &= |H_{12}(\omega)||H_{13}(\omega)||H_1(\omega)|^2 + |H_2(\omega)|^2|H_{23}(\omega)| = S_{23} \\
S_{33} &= |H_{13}(\omega)|^2|H_1(\omega)|^2 + |H_{23}(\omega)|^2|H_2(\omega)|^2 + |H_3(\omega)|^2
\end{aligned}
\tag{2.46}
$$

$$
\begin{bmatrix} S_{11} & S_{12} & S_{13} \\ S_{21} & S_{22} & S_{23} \\ S_{31} & S_{32} & S_{33} \end{bmatrix} = \begin{bmatrix} S_{x_1 x_1} & 0 & 0 \\ 0 & 1S_{x_2 x_2} & 0 \\ 0 & 0 & S_{x_3 x_3} \end{bmatrix} \times
$$
$$
\times \begin{bmatrix} |H_1|^2 & |H_1|^2|H_{12}| & |H_1|^2|H_{13}| \\ |H_1|^2|H_{12}| & |H_1|^2|H_{12}|^2 + |H_2|^2 & |H_1|^2|H_{12}||H_{13}| + |H_2|^2|H_{23}| \\ |H_1|^2|H_{13}| & |H_1|^2|H_{12}||H_{13}| + |H_2|^2|H_{23}| & |H_1|^2|H_{13}|^2 + |H_2|^2|H_{23}|^2 + |H_3|^2 \end{bmatrix}
\tag{2.47}
$$

Based on Cholesky decomposition, the matrix of the spectrum is decomposed into two upper and lower triangular matrices and a unit square matrix shown in (2.49). Here the S_{xx} is regarded as the unit square matrix since the spectral density of the Gaussian white noise is constantly 1.

$$
S_{yy} = \mathbf{L} S_{xx} \mathbf{L}^*
\tag{2.48}
$$

$$
\begin{bmatrix} S_{11} & S_{12} & S_{13} \\ S_{21} & S_{22} & S_{23} \\ S_{31} & S_{32} & S_{33} \end{bmatrix} = \begin{bmatrix} |H_1| & 0 & 0 \\ |H_1||H_{21}| & |H_2| & 0 \\ |H_1||H_{31}| & |H_2||H_{32}| & |H_3| \end{bmatrix} \begin{bmatrix} 1 & 0 & 0 \\ 0 & 1 & 0 \\ 0 & 0 & 1 \end{bmatrix} \begin{bmatrix} |H_1| & |H_1||H_{21}| & |H_1||H_{31}| \\ 0 & |H_2| & |H_2||H_{32}| \\ 0 & 0 & |H_3| \end{bmatrix}
\tag{2.49}
$$

2.3.8 19-point Simulation

Regarding the 2-point and 3-point case, it is clear that the $\mathbf{L}$ matrix is exactly same as the filter function H_{ii} in (2.39). The formula for the derivation of the wave spectrum and the matrix form of the 19-point case is given in (2.50) and (2.51). The 19-point case can be assumed as an example for all the potential cases with a different number of points. Note that in (2.51), the latter matrix on the right hand is too huge to write it on the same row so that it is separated.

$$S_{11} = |H_1(\omega)|^2 * S_{x_1 x_1} = |H_1(\omega)|^2$$

$$S_{12} = |H_{12}(\omega)|S_{11} = |H_{12}(\omega)||H_1(\omega)|^2 = S_{21}$$

$$S_{13} = |H_{13}(\omega)|S_{11} = |H_{13}(\omega)||H_1(\omega)|^2 = S_{31}$$

$$S_{22} = |H_{12}(\omega)|^2|H_1(\omega)|^2 + |H_2(\omega)|^2$$

$$S_{32} = |H_{12}(\omega)||H_{13}(\omega)||H_1(\omega)|^2 + |H_2(\omega)|^2 H_{23}(\omega)| = S_{23}$$

$$S_{33} = |H_{13}(\omega)|^2|H_1(\omega)|^2 + |H_{23}(\omega)|^2|H_2(\omega)|^2 + |H_3(\omega)|^2$$

$$S_{1\,19} = |H_{1\,19}(\omega)||H_1(\omega)|^2 = S_{1\,19}$$

$$S_{2\,19} = |H_{1\,19}(\omega)||H_{2\,19}(\omega)||H_1(\omega)|^2 + |H_2(\omega)|^2|H_{2\,19}(\omega)| = S_{19\,1}$$

$$S_{19\,19} = |H_{1\,19}(\omega)|^2|H_1(\omega)|^2 + |H_{1\,19}(\omega)|^2|H_2(\omega)|^2 + \cdots + |H_{19}(\omega)|^2$$

$$\dots \tag{2.50}$$

$$
\begin{bmatrix}
S_{11} & S_{12} & \cdots & S_{1\,19} \\
S_{21} & S_{22} & \cdots & S_{2\,19} \\
\cdots & \cdots & \ddots & \cdots \\
S_{19\,1} & S_{19\,2} & \cdots & S_{19\,19}
\end{bmatrix}
=
\begin{bmatrix}
S_{x_1 x_1} & 0 & \cdots & 0 \\
0 & S_{x_2 x_2} & \cdots & 0 \\
\cdots & \cdots & \ddots & \cdots \\
0 & 0 & \cdots & S_{x_{19} x_{19}}
\end{bmatrix}
\times
$$

$$
\times
\begin{bmatrix}
|H_1|^2 & |H_1|^2|H_{12}| & \cdots & |H_1|^2|H_{1\,19}| \\
|H_1|^2|H_{12}| & |H_1|^2|H_{12}|^2+|H_2|^2 & \cdots & |H_1|^2|H_{12}||H_{1\,19}|+|H_2|^2|H_{2\,19}| \\
\cdots & \cdots & \ddots & \cdots \\
|H_1|^2|H_{1\,19}| & |H_1|^2|H_{12}||H_{1\,19}|+|H_2|^2|H_{2\,19}| & \cdots & |H_1|^2|H_{1\,19}|^2+|H_2|^2|H_{2\,19}|^2+|H_3|^2|H_{3\,19}|^2+\cdots+|H_{19\,19}|^2
\end{bmatrix}
$$

(2.51)

Still, by implementing Cholesky decomposition, the wave spectrum of generated wave elevations can be decomposed into three parts shown in (2.52)

$$S_{yy} = \mathbf{L}S_{xx}\mathbf{L}^*$$

$$
\begin{bmatrix}
S_{11} & S_{12} & \cdots & S_{1\,19} \\
S_{21} & S_{22} & \cdots & S_{2\,19} \\
\vdots & \vdots & \ddots & \vdots \\
S_{19\,1} & S_{19\,2} & \cdots & S_{19\,19}
\end{bmatrix}
=
$$

$$
\begin{bmatrix}
H_{11} & 0 & 0 & \cdots & 0 \\
H_1H_{21} & H_{22} & 0 & \cdots & 0 \\
H_1H_{31} & H_2H_{32} & H_{33} & \cdots & 0 \\
\vdots & \vdots & \vdots & \ddots & \vdots \\
H_1H_{191} & H_2H_{192} & H_3H_{193} & \cdots & H_{19\,19}
\end{bmatrix}
\begin{bmatrix}
1 & 0 & \cdots & 0 \\
0 & 1 & \cdots & 0 \\
\vdots & \vdots & \ddots & \vdots \\
0 & 0 & \cdots & 1
\end{bmatrix}
\begin{bmatrix}
H_{11} & H_1H_{21} & H_1H_{31} & \cdots & H_1H_{191} \\
0 & H_{22} & H_2H_{32} & \cdots & H_2H_{192} \\
0 & 0 & H_{33} & \cdots & H_3H_{193} \\
\vdots & \vdots & \vdots & \ddots & \vdots \\
0 & 0 & 0 & \cdots & H_{19\,19}
\end{bmatrix}
$$

$$(2.52)$$

2.4 Hydrodynamic Load

The simulation of hydrodynamic loads for the floating bridge in this study was provided and verified by Cheng et al. [7][4]. In SIMA numerical simulation, the pontoons of the floating bridge are regarded as large volume constructions. Therefore, the hydrodynamic coefficients of the pontoons such as added mass, damping coefficient, and wave excitation forces are computed based on the potential flow theory. Note that, the interaction between adjacent pontoons and the wall effect is not taken into consideration when estimating the hydrodynamic coefficients in this thesis since there is long enough distance between each pontoon and fjord wall. In this thesis, the theory of hydrodynamic load part is less focused compared to the theory of wave field simulation part. Several basic theories and definitions are introduced here. The various damping effects are detailed introduced in Sunghun's thesis [11].

2.4.1 Equation of Motion

The pontoons are considered as rigid bodies and the response can be calculated by the general form of the equation of motion [4] which is expressed in (2.53).

$$\sum_{i=1}^{6} \left[(M_{ij} + A_{ij}^{\infty})\ddot{x}_j(t) + \int_{-\infty}^{\infty} B_{ij}(\tau)\dot{x}_j((t-\tau))d\tau + C_{ij}x_j(t) \right] = F_j^{exc}(t) \quad (2.53)$$

where the i,j = [1,6] represent the degree of freedom (DOF). The $\ddot{x}_j(t)$, $\dot{x}_j(\tau)$ and $x_j(t)$ are the acceleration, velocity and displacement of the pontoon respectively. M_{ij} means the mass of the pontoon, $A_{ij}^{\infty})$ represents the added mass of the pontoon at the infinity frequency. The damping force is given by the combination of the retardation function $B_{ij}(\tau)$ and the velocity of the pontoon. C_{ij} is the restoring coefficient which includes hydrostatic restoring coefficient contributed by buoyancy and the nonlinear restoring force due to the girder stiffness. The excitation force is express in (2.54). The excitation force $F_j^{exc}(t)$ contains the first order $F^1(t)$ and second order mean drift force $F^2(t)$. The $F^{drag}(t)$ means the drag force. The first order wave force and second order wave force will be expressed briefly in the following sections. Note that the drag force $F^{drag}(t)$ will not be studied in this thesis.

$$F^{exc}(t) = F^1(t) + F^2(t) + F^{drag}(t) \quad (2.54)$$

2.4.2 First Order Wave Force

Based on the linear potential flow theory, the first order wave force [4] consists of the first order wave transfer function $|H(\omega_n, \theta_m)|$ and the wave elevation expressed in (2.55). The wave transfer function will be estimated in the frequency domain.

$$\begin{aligned} F^1(x,y,t) = \Re \Bigg\{ &\sum_{n=1}^{N} \sum_{m=1}^{M} |H(\omega_n, \theta_m)| \sqrt{2S_\eta(\omega_n)D(\theta_m)\Delta\omega\Delta\theta} \\ &exp\big(i(\omega_n t - k_n x cos(\theta_m) - k_n y sin(\theta_m) + \epsilon_{nm} + \phi_{H_{nm}^1})\big) \Bigg\} \end{aligned} \quad (2.55)$$

where the $\sqrt{2S_\eta(\omega_n)D(\theta_m)\Delta\omega\Delta\theta}$ means the exact same as (2.19) but for a wave eleva-
tions. $\phi_{H^1_{nm}}$ represents the phase angle of the transfer function. By applying the stochastic
definition, the spectrum of the first order wave force for the long crest wave is derived in
(2.56)

$$S_{F^1}(\omega) = H^{(1)}(\omega_n)H^{(1)*}(\omega_n)S_\eta(\omega) \tag{2.56}$$

where the $H^{(1)*}(\omega_n)$ denotes the complex conjugate of $H^{(1)}(\omega_n)$, $S_\eta(\omega)$ gives the spec-
trum of the wave elevation.

2.4.3 Second Order Wave Force

Second order wave force is considered in this thesis since the first two eigenmodes in [4]
are significant which means the difference-frequency wave force may affect. Additionally,
the second order wave force is calculated the numerical model in SIMA. Note that the
directions interaction effect is neglected here as well as mentioned in [4]. The second
order wave force is derived in with Newman's approximation.

$$\begin{aligned}
F^2(x,y,t) = \Re\Big\{ \sum_{n=1}^{N}\sum_{m=1}^{M} |H(\omega_n,\theta_m)|\sqrt{2S_\eta(\omega_n)D(\theta_m)\Delta\omega\Delta\theta} \\
exp\big(i(\omega_n t - k_n x cos(\theta_m) - k_n y sin(\theta_m) + \epsilon_{nm} + \phi_{H^1_{nm}})\big)\Big\}
\end{aligned} \tag{2.57}$$

2.4.4 Drag Force

The viscous drag force is computed by Morison's equation:

$$F^{drag}(t) = \frac{1}{2}\rho C_d A \dot{u}_r(t)|\dot{u}_r(t)| \tag{2.58}$$

where ρ means the density of water, C_d is the quadratic drag coefficient, A is the projected
area of the body, and $\dot{u}_r(t)$ represents the relative velocity between the incident wave
velocity and body response velocity. The Morison's equation is essential to estimate the
drag force correctly.

2.4.5 Imported Excitation Forces

In (2.53), the excitation force $F_j^{exc}(t)$ is the only component related to the incident wave
field. Thanks to Chengs et al. [6] , the method of importing the excitation force from the
external data has been proved available and contributory to this thesis. Taking account of
all the wave loads due to the inhomogeneous wave field, the excitation force $F_j^{exc}(t)$ of
each pontoon is generated by MATLAB script separately since it is impossible to generate
time series of excitation force in SIMA. Note that the time series of excitation forces are
generated based on known sea state characters which include significant wave height and
peak period. The incident wave characters are computed by implementing the spectral
moments in section 2.2.4 and using the wave elevations generated in section 2.3.6. To ac-
complish the whole procedure, the wave condition in SIMA for the simulation is assumed

rather low significant wave height and the time series of excitation force created by MAT-LAB script should be imported before running the simulation by the code in user's manual [12].

Chapter 3

Results And Discussion

The results of the 3-hour short term simulations are presented in this chapter. The contents include: input environmental conditions, the verification of Campbell analogy and Cholesky decomposition, the analyses of applied theories, the simulation results of multi-point case based on different wave conditions, comparison of results by two Campbell analogy and Cholesky decomposition, and global dynamic responses analyses.

Methodologies

In this thesis, two methods to generate the filter function matrix H_{ii} are mentioned in section2.3. One is to compute the filter functions by implementing the experience mentioned in Compbell Mento Carlo simulation [3], another is to compute the matrix by Cholesky decomposition. The accuracy of the two methods will be examined in the results chapter.

Comparison

In the previous section 2.3, several multi-point cases of generating wave elevation were presented. The results of 1-point, 2-point, and 19-point simulations will be compared with each other by various means. Additionally, there are results of other interesting cases which include two independent wave series and two fully correlated wave elevations. Regarding the dynamic response of the floating bridge, all types of incident wave conditions will be conducted as input data for SIMA simulation. The comparison will be carried out between the homogeneous wave field, the inhomogeneous wave field, the newly simulated homogeneous wave field, and the newly simulated inhomogeneous wave field.

3.1 Verification of The Wave Field Simulation Procedure

In this section, the one-point and two-point simulations will be presented to verify that the simulation procedure is sufficient. Regarding the one-point case, the Campbell analogy will be applied to conduct the simulation. In terms of two-point with assumed coherence function, both Campbell analogy and Cholesky decomposition will be applied for generating time series of wave elevations.

3.1.1 One-point Case Examination

For the one-point case, it is essential to confirm that the whole procedure will run successfully and return to rational results. The basic idea is to compare the wave characteristics of wave spectra which are computed by various means. Since it is mentioned that the wave spectrum should be known before deriving the filter functions, the initial wave characteristics are needed for every simulation.

The initial data is assumed that significant wave height is 2 m and wave peak period is 5.9 s. The initial Jonswap spectrum is created by the definition (2.12) with $\gamma = 3.3$ assumed.

There are two methods to simulate the corresponding time series of wave elevations. One is to decomposing the initial Jonswap spectrum with (2.3) and (2.4). The other one is to produce the transfer function H_1 by (2.23) and the time series is derived by (2.27). Note here, the phase angles are randomly generated between $[0, 2\pi]$ but the phase angles are the same for both methods. The wave elevations based on two means are displayed in 3.1. Since the wave elevations from same wave spectrum should be the same as long as the phase angles are synchronous, the results are rational that two time series overlaps entirely.

To confirm that the wave elevations can return to the same spectrum, the WAFO function 'dat2spec' is implemented to compute the wave spectrum of the time series. The wave characteristics are calculated by the spectral moments mentioned in 2.2.4. In Fig.3.2, the two wave spectrum are quite close. The wave characteristics of different wave spectra are shown in Table.3.1. The maximum difference in significant wave height is 0.01 while the peak periods seem to be magnified by about 0.03. The differences are acceptable in both significant wave height and wave peak period and the one-point case is examined feasible.

Table 3.1: Characteristics of wave spectrum calculated by several means

height	H_s	T_p
initial data	2.0	5.9
initial Jonswap spectrum	1.99	5.897
Spectrum based on initial wave elevations	1.998	5.854
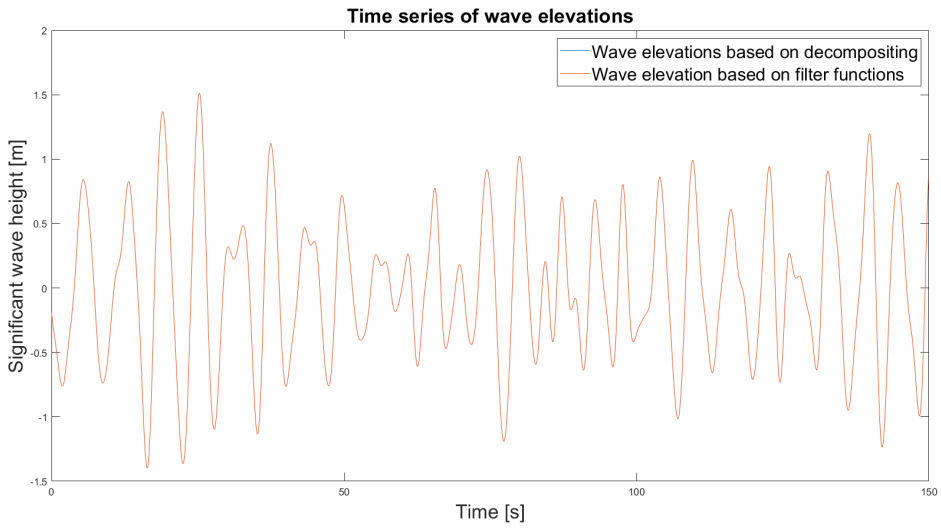
Figure 3.1: Time series of wave elevations generated based on decomposing and filter functions
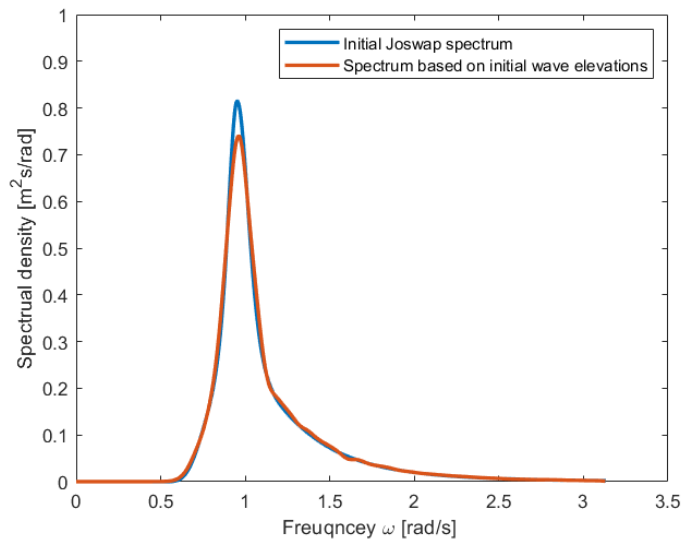
Figure 3.2: Comparison between wave spectrum calculated by several means

3.1.2   Simulation Results of The Two-point Case

In this section, three simulations are conducted which include wave simulation of independent two points, wave simulation of correlated two points, and wave simulation of fully correlated two points. The two methodologies including the Campbell analogy and the Cholesky decomposition will be implemented for the correlated two points case. The input data are shown in Table.3.2.

Table 3.2: Wave characteristics of wave spectrum at two points

	Two point case	
	H_s	T_p
Point 1	2.0	5.9
Point 2	2.0	5.9

Wave Simulation of Independent Two-point Case

The significant wave heights H_s are both 2.0 m while the wave peak periods T_p are the same, 5.9 s. The method for simulating two independent time series of wave elevations is to decompose the initial Jonswap spectrum and compute the coherence function between the two wave elevations. Since the two points are independent of each other, the coherence between their times series should be significant low. Matlab function 'mscohere' is applied to compute the coherence between the two elevations sketched in Fig.3.3. It is spotted that the coherence is below 0.03 that can be regarded as mutual independence.
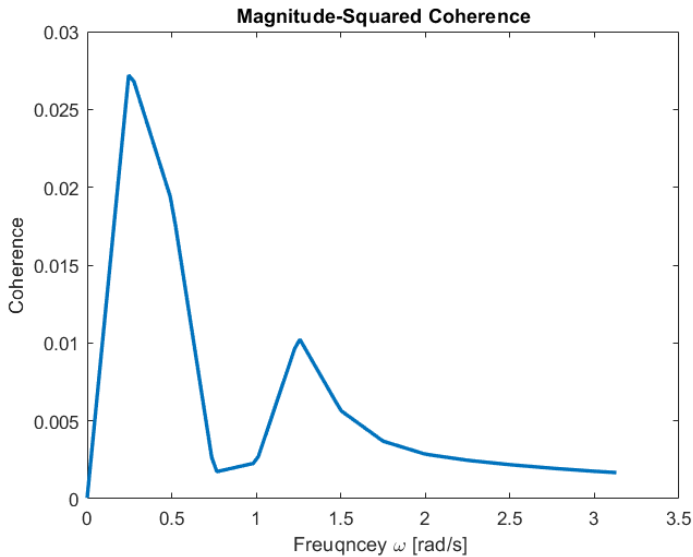
Figure 3.3: Coherence between wave elevations at two points

Then the spectrum can be computed from the two time series of wave elevations. The initial Jonswap spectrum and the spectrum based on wave elevations decomposed from the initial Jonswap spectrum are compared in Fig.3.4. The wave characteristics are displayed in Table.3.4. The differences between the input data and the wave characteristics of two spectra are rather low, only 0.006 which can be considered returning to the initial data. The whole procedure is proved sufficient.
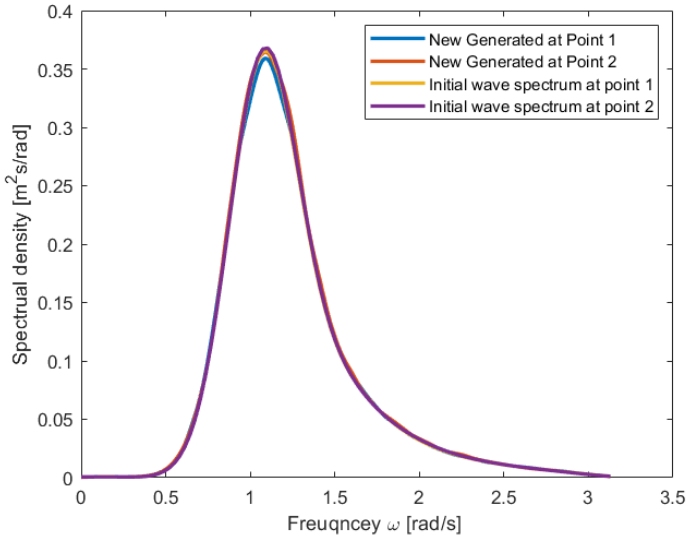
Figure 3.4: Initial spectrum at two points and regenerated spectrum at two points

Table 3.3: Wave characteristics of wave spectrum at two points

	Independent two point case	
	H_s	T_p
Input data	2.0	5.9
Newly generated at point 1	1.993	5.729
Newly generated at point 2	2.003	5.851

The auto-correlated spectrum and cross-spectrum are computed by applying and sketched in Fig.3.5. The two auto-correlated spectra are the same ones as newly generated at Point 1 and 2 plotted in Fig.3.4. Independence leads to low coherence and low H_{12}. The cross-spectrum is almost about zero that is caused by low coherence between the two wave elevations.

Implementing the Campbell analogy method, the times series are computed based on the combinations of filter functions and time series of Gaussian white noise. Part of the time series are depicted in Fig.3.7 and the total time is 3 hours long.
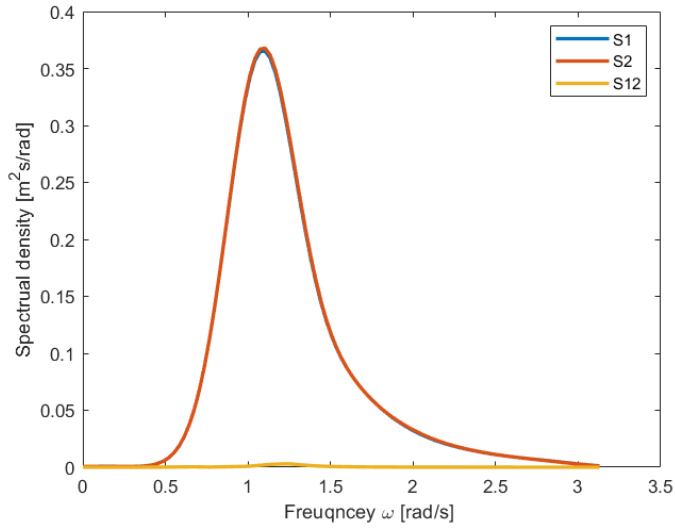
Figure 3.5: Spectrum at two points and cross-spectrum between two points
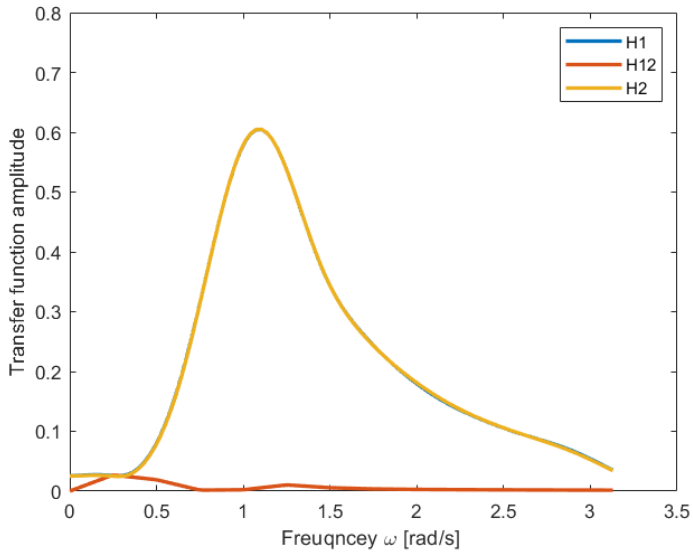
Figure 3.6: Filter functions for independent two-point case
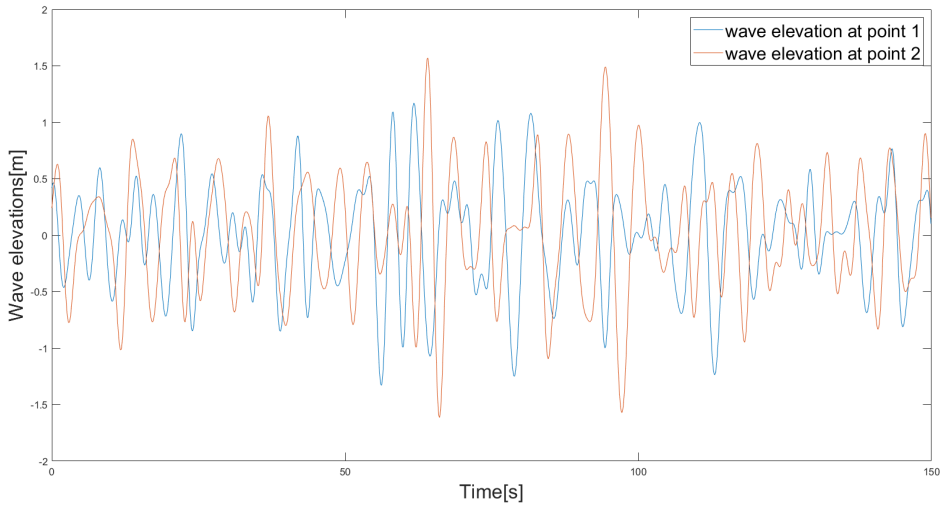
Figure 3.7: Wave elevations at two points

Wave Simulation of Fully Correlated Two-point Case

The fully correlated two-point case is introduced in this section. 'Fully correlated' means that the coherence between the wave elevations at different points has the same amplitude, same phase angle, and same wave characteristics consequently. Typically, the coherence is constantly 1 with respect to the frequency. The coherence function between two points is illustrated in Fig.3.8.
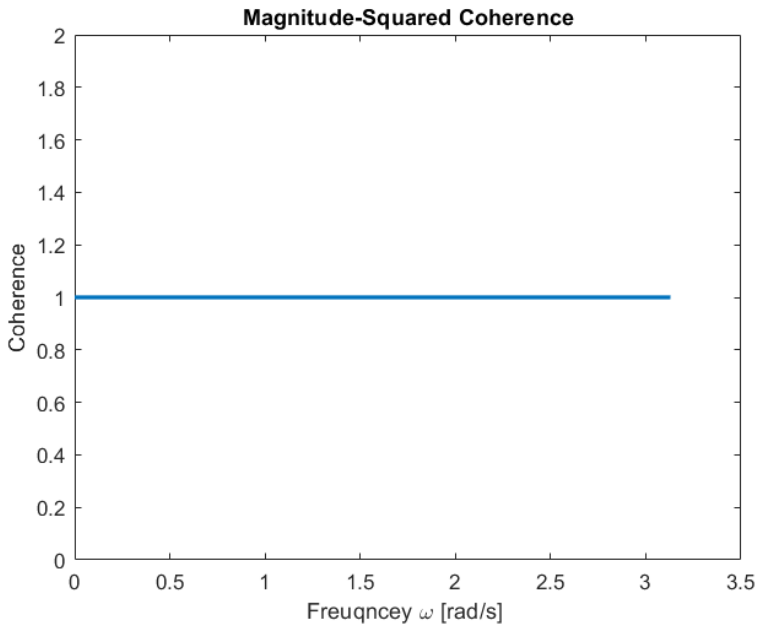
Figure 3.8: Coherence between fully correlated wave elevations at two points

The spectrum of point 1 and point 2 should be the same since the input wave characteristics are the same. By the definition of the coherence function (3.1.2), the cross-spectrum is equal to both of the auto-correlated spectrum since the coherence is 1. The auto-correlated spectrum and cross-spectrum of fully correlated wave elevations at two points are displayed in Fig.3.9 and the results are reasonable.
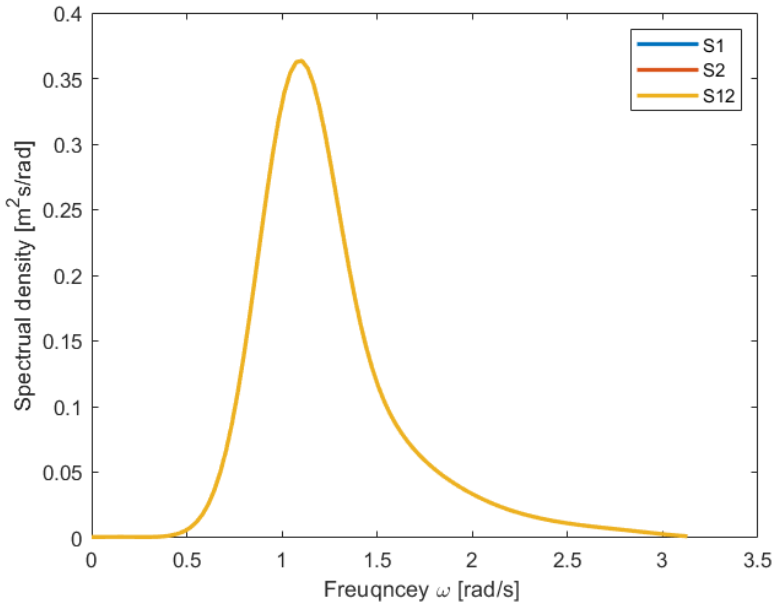
Figure 3.9: Auto-correlated spectrum and cross spectrum of fully correlated wave elevations at two points

Table 3.4: Wave characteristics of wave spectrum at two points with assumed coherence

	Fully correlated two point case	
	H_s	T_p
Input data	2.0	5.9
Newly generated at point 1	2.006	5.851
Newly generated at point 2	2.006	5.851

Regarding $coh_{12}(\omega) = 1$, the filter functions can be computed by $|H_1(\omega)| = \sqrt{S_{11}}$, $|H_{12}(\omega)| = S_{12}/S_{11} = 1$, $|H_2(\omega)| = S_{22}(1 - coh_{12}(\omega)) = S_{22}(1 - 1) = 0$. The filter functions are sketched in Fig.3.10.

Likewise, the one-point case, the wave elevations generated from two spectra at two points are the same according to the fully correlated definition. The time series are illustrated in Fig. 3.11. Since the two wave elevations are fully correlated, the significant wave height H_s, wave peak period T_p, and phase angle ϕ are the same for two simulations. Therefore, the two wave elevations overlap completely.
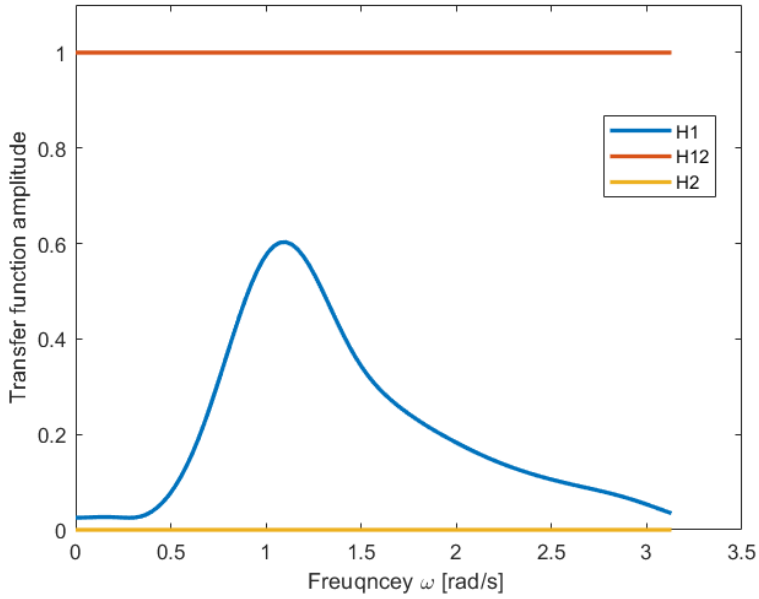
Figure 3.10: Filter functions for fully correlated two-point case
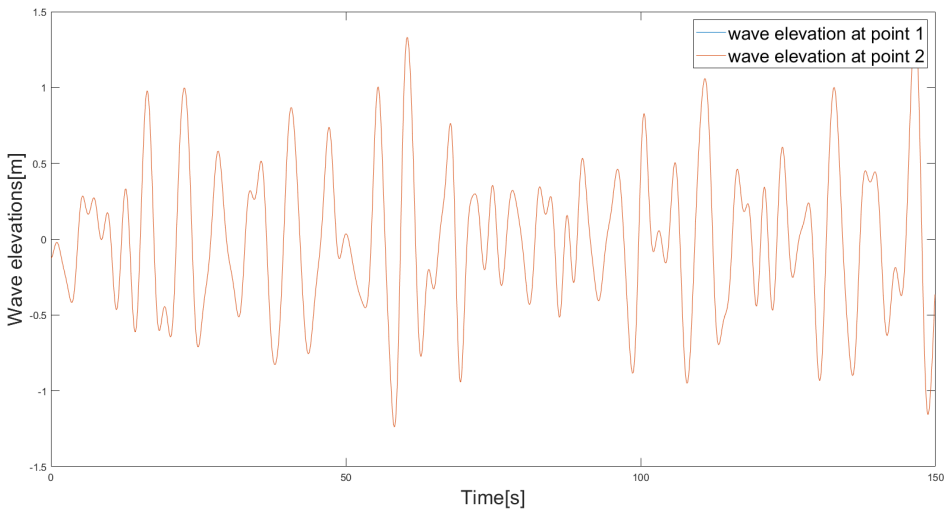
Figure 3.11: Fully correlated wave elevations at two points

Wave Simulation of Correlated Two-point Case With Assumed Coherence Function

The distance between the two points is 197 meters which is the interval distance between adjacent pontoons. The coherence between the two points is obtained from the function shown in Fig. 2.10. The coherence remains constantly 0.3131 in this case which does not vary with respect to frequency. By the definition of coherence function and the cross-spectrum, the cross transfer function is the same value as the coherence. All filter functions are depicted in Fig.3.12. The H_{12} curve has a noticeable jump from 0 to 0.3131 remaining straight line. The H_{12} is supposed to be 0.3131 for this case but the 0 value is to assumed to avoid the potential numerical error due to the low function value of S_1 and S_{12} at low frequencies.
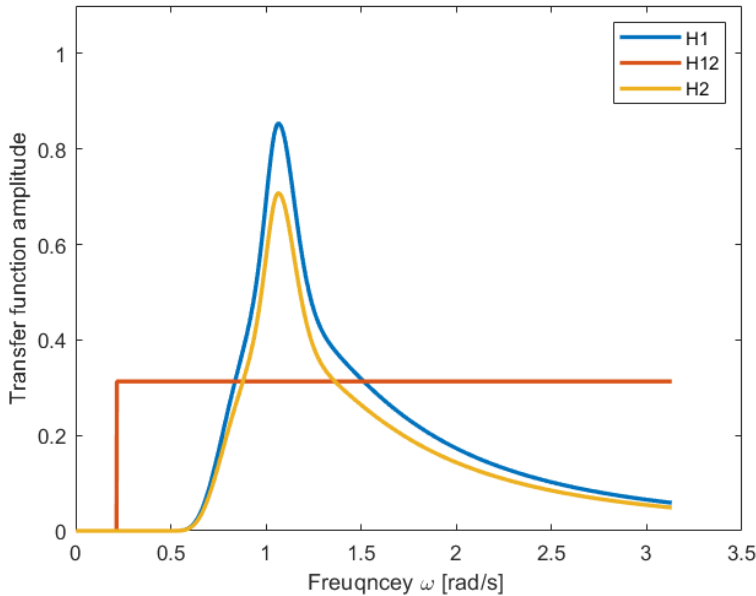
Figure 3.12: Filter functions for realistic two-point case

Regarding the involved two points, the spectra of two points are generated by the two methods Campbell analogy and Cholesky decomposition. The comparison of the spectra from the two methods and initial Jonswap spectrum is illustrated in Fig.3.13 and Fig.3.14. In Fig.3.13, the spectrum at point 2 has an obvious difference while the spectrum at point 1 is quite close to the initial Jonswap spectrum. In terms of Fig.3.14, the two spectra by application of methods have a low deviation between the initial Jonswap spectrum. It can draw a conclusion that the Cholesky decomposition gives better simulation results that the generated wave characteristics are close to the input data. The comparisons of wave characteristics of the spectra by Campbell analogy and Cholesky decomposition are listed in Table.3.5 and 3.6 respectively. The biggest difference is about 0.24 and occurs

when generating the wave spectrum at point two by Campbell analogy. The Cholesky decomposition gives better results that the wave characteristics are pretty close to the initial input data.
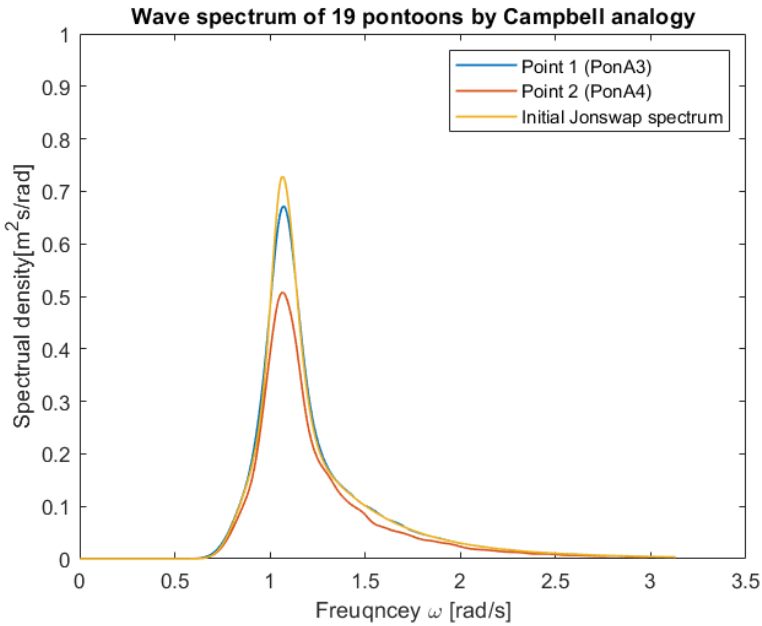
Figure 3.13: Comparison of wave spectra at two points by Campbell analogy

Table 3.5: Wave characteristics of wave spectrum at two points by Campbell analogy

	Realistic two-point case by Campbell analogy	
	H_s	T_p
Input data	2.0	5.9
Newly generated at point 1	1.998	5.851
Newly generated at point 2	1.764	5.894
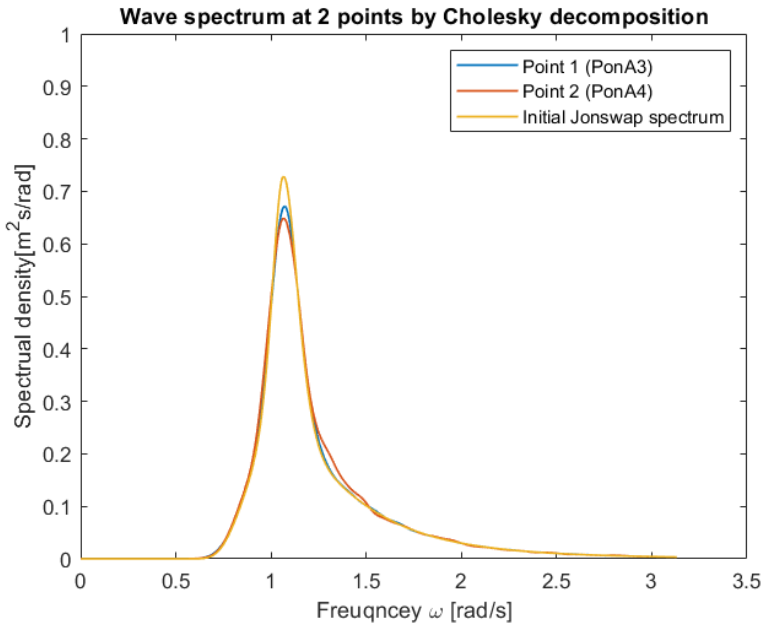
Figure 3.14: Comparison of wave spectra at two points by Cholesky decomposition

Table 3.6: Wave characteristics of wave spectrum at two points by Cholesky decomposition

	Realistic two-point case by Cholesky decomposition	
	H_s	T_p
Input data	2.0	5.9
Newly generated at point 1	1.998	5.851
Newly generated at point 2	1.991	5.894

The wave elevations are generated by the combination of the filter functions and Gaussian white noise. The times series by two methods are plotted in Fig.3.15 and Fig.3.16. The phase angles of each simulation based at a certain point are the same. Therefore, every wave crest at point 1 or point 2 by different methods happens at the same time.
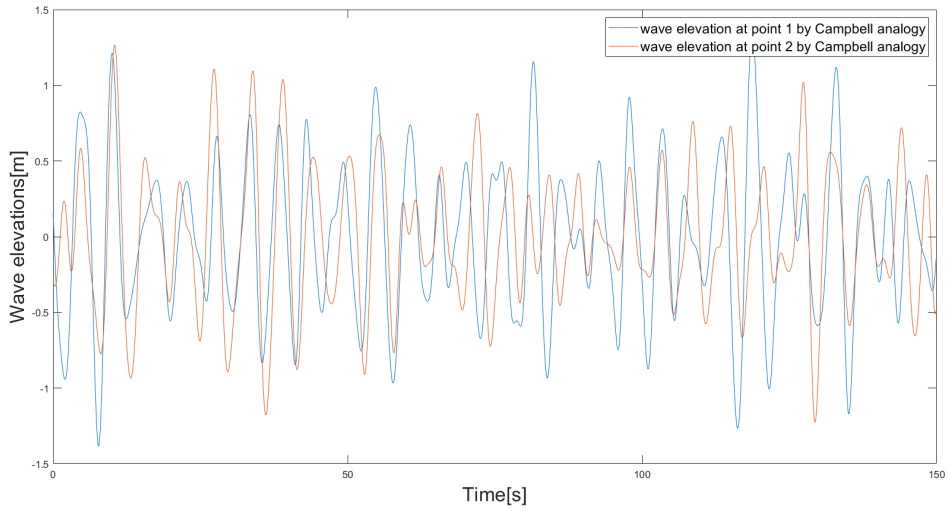
Figure 3.15: Wave elevations at two points by Campbell analogy
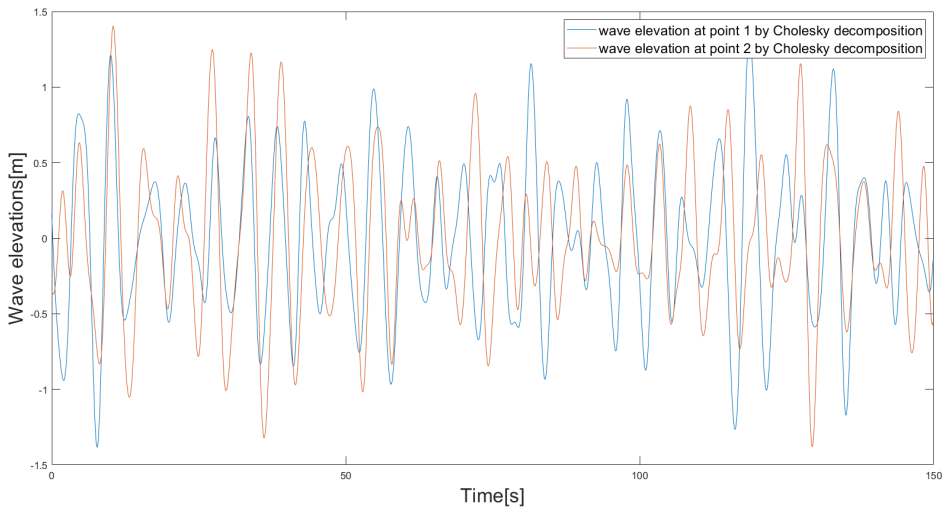
Figure 3.16: Wave elevations at two points by Cholesky decomposition

3.2   Simulation of Wave Field at Bjørnafjorden

In this section, the simulation of wave field at Bjørnafjorden will be conducted. As described in the previous part, the input wave characteristics should be collected or assumed before the wave field simulation. The meaning of the simulation of wave field is that times series of wave elevations can be generated numerically instead of collecting real-time wave elevation by devices set up in the ocean. The simulation can be considered as a procedure to estimate the real-time series of wave elevations.

The results of several cases will be presented as follows. Based on the Cheng's studies [7][6], both one-year wave condition and 100-year wave condition are taken into account. Besides, homogeneous and inhomogeneous wave conditions are carried out for comprehensive results. Therefore, four combinations of different wave conditions including 1-year homogeneous wave condition, 100-year homogeneous wave condition, 1-year inhomogeneous wave condition, and 100-year inhomogeneous wave condition will be used as input data for the simulation of the wave field at the fjord.

To define the inhomogeneity and homogeneity, some parameters such as significant wave height H_s, wave peak period T_p, wave direction θ_p, and phase angle ϕ in (2.7) and (2.2.5) should be considered. For every simulation of the floating bridge in this thesis, the wave direction θ_p is considered constantly 288 [°] while the phase angle ϕ is randomly generated independently. The wave field is homogeneous if the significant wave height H_s and wave peak period T_p are identical for all pontoons; otherwise, the wave field is regarded as inhomogeneous.

According to the hindcast wind data of Bjørnafjorden, the 100-year wind wave condition including the significant wave heights and peak periods were estimated in Table.1.2. But the 100-year wave condition of Bjørnafjorden can not be estimated based on the known data right now. The inhomogeneous wave field of the 100-year wave condition should be assumed rationally. The input wave characteristics of 1-year and 100-year homogeneous wave conditions are listed in Table.3.7 including the significant wave height, peak period, and wave direction.

The hypothesis of the simulation is that the Pon A3 is assumed as the first point which is mentioned in the 19-points case in theory part meaning that the wave elevations at Pon A3 will not be affected by wave elevations at other pontoons but will affect the rest wave elevations. The second wave elevations at Pon A4 has the same property.

Table 3.7: 1-year and 100-year homogeneous Wave Field

Pontoon NO.	1-year homogeneous wave cond.			100-year homogeneous wave cond.		
	$H_s[m]$	$T_p[s]$	$\theta_p[°]$	$H_s[m]$	$T_p[s]$	$\theta_p[°]$
A3-A19	1.15	3.77	288	2.4	5.9	288

3.2.1   1-year Homogeneous Wave Field Simulation

The homogeneous wave field provides a uniform input data including significant wave height and peak period. For 1-year homogeneous wave condition [4], the significant wave height and peak period are assumed as 1.15 m and 3.77 s respectively in this study.

Applying the two methods, time series of wave elevations at 19 pontoons are generated. By 'dat2spec.m', the wave characteristics are computed. The mean wave characteristics of ten times independent simulations are listed in Table.3.8. The comparison of significant wave heights at 19 pontoons between initial data, Campbell analogy, and Cholesky decomposition is depicted in Fig.3.17. The results computed by two methods are inhomogeneous actually since the significant wave heights of newly generated wave elevations at 19 pontoons are diverse. That is due to the randomness inside the numerical simulation which leads to inhomogeneous results. Theoretically, the results should be homogeneous based on many times simulations.

Table 3.8: 1-year homogeneous wave condition : initial data, results by Campbell analogy and Cholesky decomposition

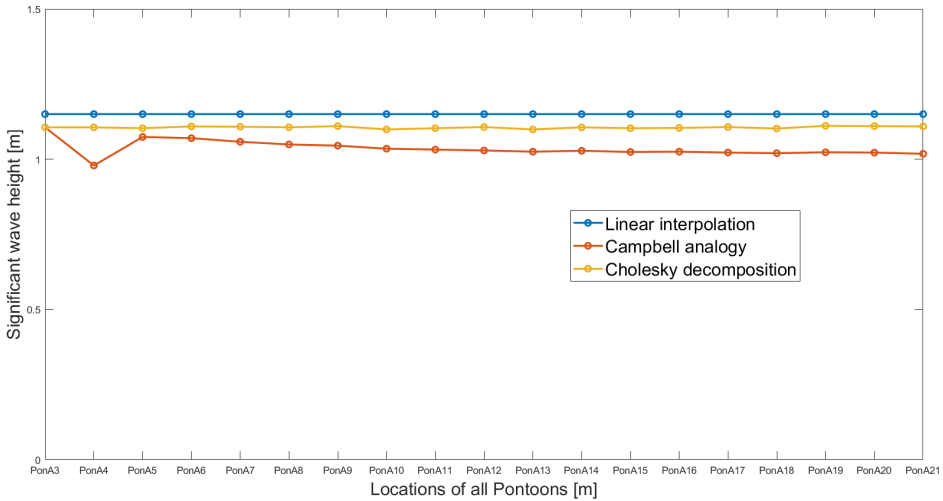| 1-year wave cond.	Initial data		Campbell analogy		Cholesky decomposition	
Pontoon NO.	H_s	T_p	H_s	T_p	H_s	T_p
A3	1.15	3.77	1.106	3.758	1.106	3.758
A4	1.15	3.77	0.979	3.828	1.106	3.828
A5	1.15	3.77	1.074	3.758	1.103	3.758
A6	1.15	3.77	1.070	3.758	1.109	3.775
A7	1.15	3.77	1.058	3.758	1.108	3.775
A8	1.15	3.77	1.049	3.758	1.106	3.741
A9	1.15	3.77	1.045	3.775	1.110	3.793
A10	1.15	3.77	1.035	3.775	1.099	3.793
A11	1.15	3.77	1.032	3.758	1.103	3.810
A12	1.15	3.77	1.029	3.793	1.107	3.828
A13	1.15	3.77	1.025	3.775	1.099	3.793
A14	1.15	3.77	1.028	3.741	1.106	3.758
A15	1.15	3.77	1.024	3.741	1.103	3.741
A16	1.15	3.77	1.025	3.758	1.104	3.775
A17	1.15	3.77	1.022	3.758	1.107	3.775
A18	1.15	3.77	1.020	3.724	1.102	3.724
A19	1.15	3.77	1.023	3.758	1.111	3.758
A20	1.15	3.77	1.022	3.793	1.110	3.810
A21	1.15	3.77	1.018	3.775	1.109	3.810

Figure 3.17: Comparison between significant wave height at 19 pontoons of 1-year homogeneous wave condition

Comparing with the results from Campbell analogy, the results from Cholesky decomposition are closer to the initial data especially in terms of the significant wave height H_s. At pontoon A9, A19, and A20, the newly generated significant wave heights are 1.110 m, 1.111 m, and 1.110 m respectively which approach 1.15 m nearly. By the definition of the wave peak period, the T_p is the frequency when the spectral density function of newly generated wave spectrum has its maximum value. Regarding the wave peak period, both methods have good performance in the simulation. The results fluctuate around the input T_p 3.77 s with a small range. The ideal situation is that the newly generated wave elevations have the same wave characteristics as the input data. Therefore, the results of better mean are supposed to return to the initial wave characteristics.

To illustrate a clear understanding of the accuracy of the two methods, the deviations between the three kinds of data are sketched in Fig.3.18. The percentage of deviations by both Campbell analogy and Cholesky decomposition is the same value at Pon A3 due to the transfer functions H_1 are the same value for both methods. The deviation rate of the results of Campbell analogy has a sudden increase at Pon A4 from about 4 percent to about 15 percent which indicates the accuracy is quite low and the deviation rate increase to almost 12 percent along with the separated distance from the pontoon Pon A3. On the contrary, the deviation rate of results of Cholesky decomposition maintain around 4 percentage which is rather low and has small fluctuation.
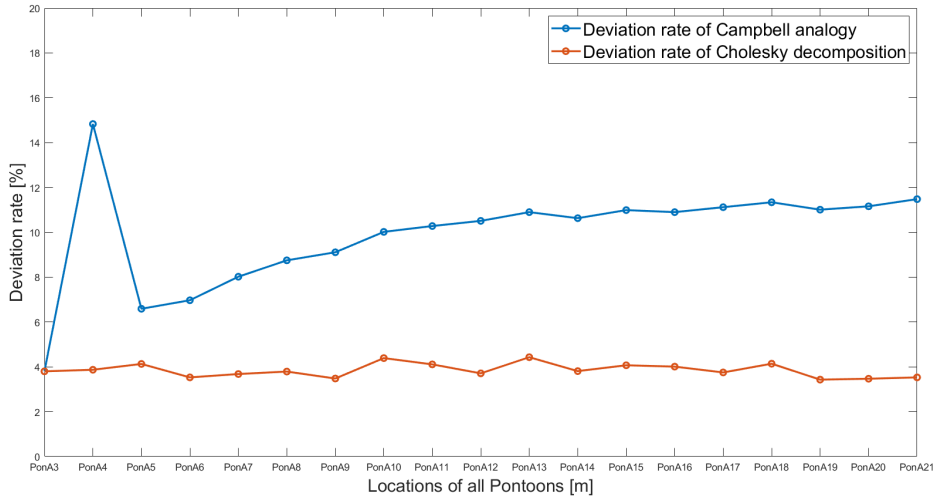
Figure 3.18: Deviation rate of significant wave height of 1-year homogeneous wave condition by two methods

Taking the spectrum of 19 pontoons from one of ten times simulation as an example, the results of Campbell analogy and Cholesky decomposition are illustrated in Fig.3.19 and Fig.3.20 respectively. Besides the spectra at 19 pontoons, the initial Jonswap spectrum generated from input data is illustrated to indicate a clear comparison. It can be seen that the spectra generated by Cholesky decomposition assemble closer to the initial Jonswap spectrum compared to the spectra generated by Campbell analogy.

According to DNV-RP-C205, the peak period is defined as the inverse of the frequency where the maximum value of spectral density function occurs. From the spectra illustrated in Fig.3.19 and Fig.3.20, the spectrum has its maximum value at around 1.7 rad/s so that the reverse is about 3.7 s which approach the input data 3.77 s. It is rational that the results wave peak periods which are computed by the definition are quite near to the input data 3.77 s. But during the test of coding, the peak periods calculated by the spectral moments are bigger than the input data by 0.7 s. I think this may result from the numerical error when calculating the spectral moments in Matlab.

The mean values of 19 spectra computed by Campbell analogy and Cholesky decomposition are compared in Fig.3.21. The mean value of the spectra generated by Cholesky decomposition is closer to the initial Jonswap spectrum and has larger energy than the other one.

The criterion of judging the performance of the method is to verify if the results can return to the input wave condition with the same wave characteristics. It can draw the conclusion that the Cholesky decomposition gives better results in 1-year homogeneous wave field simulation since the results of Cholesky decomposition have less deviation compar-

ing with the input data especially in terms of significant wave heights.

The newly generated times series of wave elevations at three locations (Pon A3, A9 and, A17) by Campbell analogy and Cholesky decomposition are illustrated in Fig.3.22 and Fig.3.23 respectively. Since the three DWRs are located near to the three pontoons, Pon A3, A9, and A17 pf what three time series are selected as examples. When generating the time series, the phase angles are randomly generated for each simulation but same values for two methods so that the two wave crests occur at the same frequencies in both Fig.3.22 and Fig.3.23.
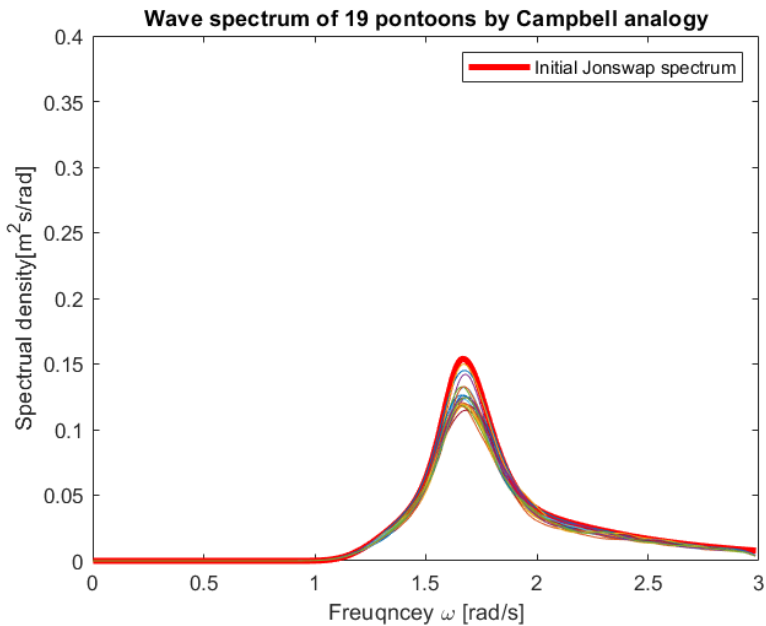
Figure 3.19: Wave spectrum at 19 pontoons of 1-year homogeneous wave condition based on Campbell analogy
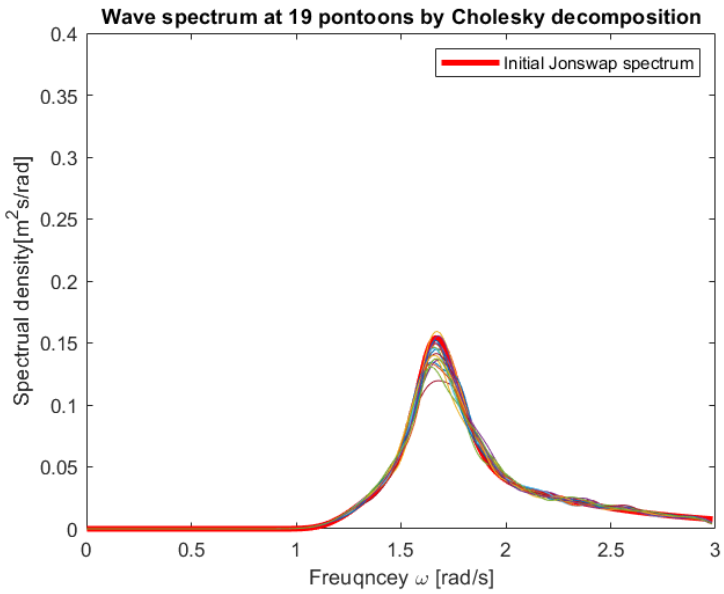
Figure 3.20: Wave spectrum at 19 pontoons of 1-year homogeneous wave condition based on Cholesky decomposition

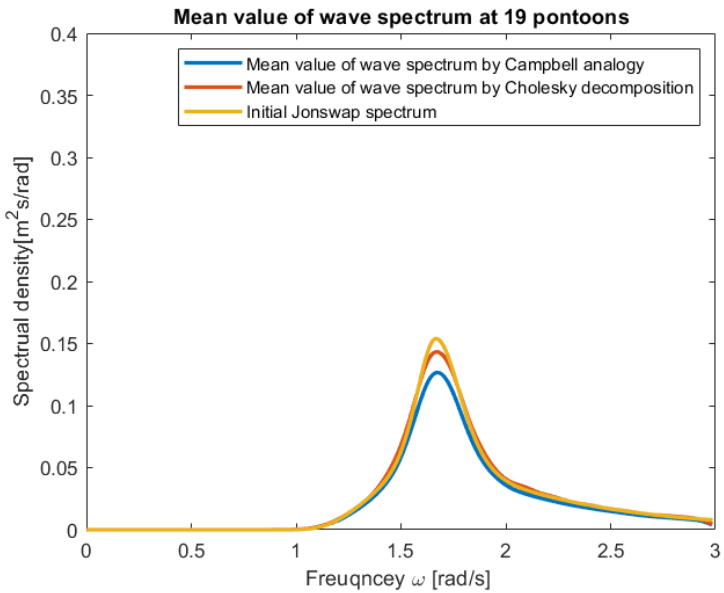**Figure 3.21:** Comparison between mean value of wave spectrum at 19 pontoons of 1-year inhomogeneous wave condition based on Campbell analogy and Cholesky decomposition
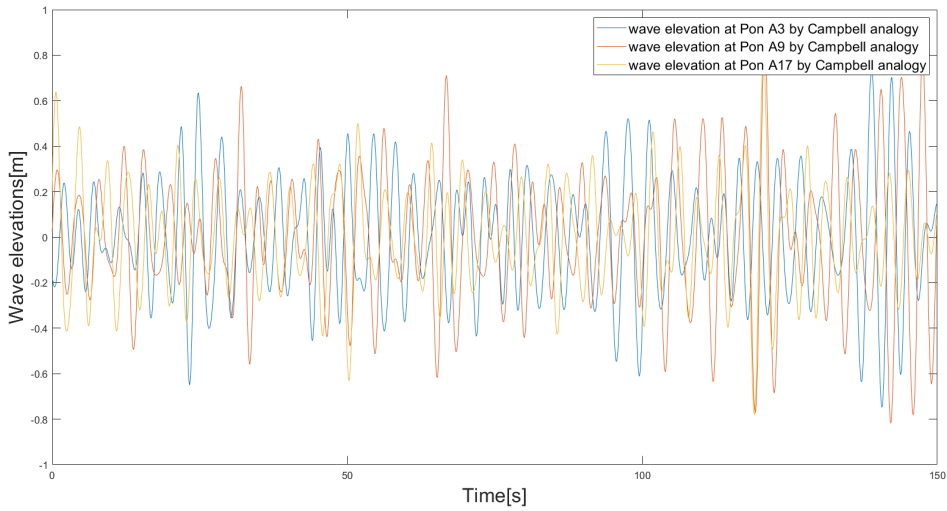
Figure 3.22: Newly generated time series of wave elevations of Pon A3, A9 and A17 by Campbell analogy
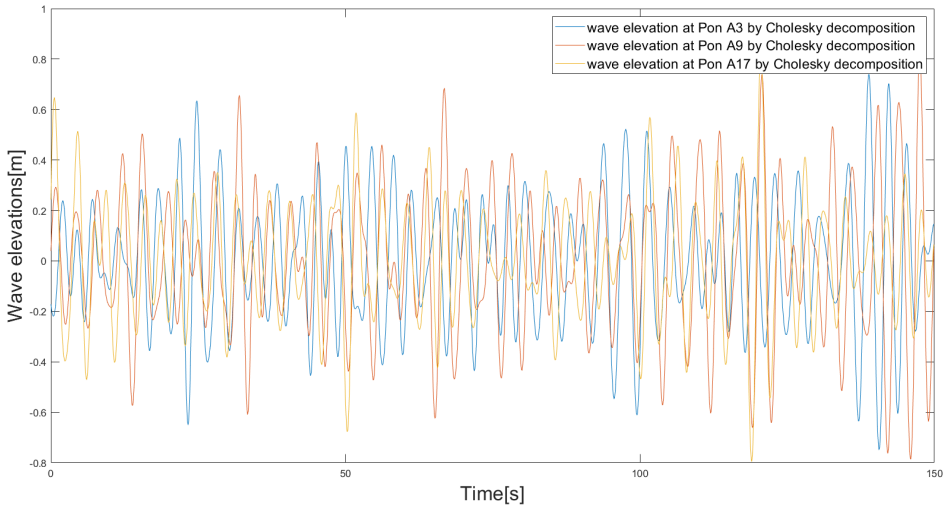

Figure 3.23: Newly generated time series of wave elevations of Pon A3, A9 and A17 by Cholesky decomposition

3.2.2 100-year Homogeneous Wave Field Simulation

For the 100-year homogeneous wave field simulation, the input data significant wave height H_s and peak period T_p are 2.4 m and 5.9 s severally. The input data are quoted from Cheng's work [4]. Note that the wave directions are the same for all the simulations at 19 pontoons and the phase angles are randomly generated for each simulation.

Using this input data to run the same procedure introduced before, the mean value of independent ten times 3-hour short-term simulations wave characteristics of spectra of 19 pontoons are presented in Table.3.9. The wave characteristics generated from Campbell analogy have differences in comparison with the initial data while the results from the Cholesky decomposition have smaller gaps. Newly generated H_s by Cholesky decomposition have good results which are 2.403, 2.403, and 2.398 at pontoon A7 A15, and A17 respectively. The wave peak periods computed by the wave spectra by both methods can nearly return to the input data 5.9 s.

Table 3.9: 100-year homogeneous wave condition : initial data, results by Campbell analogy and Cholesky decomposition

100-year wave cond.	Initial data		Campbell analogy		Cholesky decomposition	
Pontoon NO.	H_s	T_p	H_s	T_p	H_s	T_p
A3	2.4	5.9	2.387	5.851	2.387	5.851
A4	2.4	5.9	2.101	5.894	2.373	5.894
A5	2.4	5.9	2.324	5.894	2.384	5.894
A6	2.4	5.9	2.304	5.851	2.394	5.851
A7	2.4	5.9	2.289	5.851	2.403	5.851
A8	2.4	5.9	2.267	5.894	2.393	5.980
A9	2.4	5.9	2.239	5.894	2.371	5.936
A10	2.4	5.9	2.242	5.894	2.393	5.936
A11	2.4	5.9	2.232	5.851	2.396	5.894
A12	2.4	5.9	2.226	5.894	2.387	5.894
A13	2.4	5.9	2.220	5.894	2.392	5.936
A14	2.4	5.9	2.208	5.894	2.369	5.980
A15	2.4	5.9	2.220	5.894	2.400	5.894
A16	2.4	5.9	2.212	5.851	2.386	5.894
A17	2.4	5.9	2.211	5.851	2.398	5.851
A18	2.4	5.9	2.191	5.851	2.358	5.810
A19	2.4	5.9	2.202	5.851	2.383	5.894
A20	2.4	5.9	2.192	5.851	2.368	5.936
A21	2.4	5.9	2.200	5.851	2.396	5.810

The significant wave heights of spectra of 19 pontoons are illustrated in Fig.3.24. The gap between H_s of initial data and the results of Cholesky decomposition is narrow. And the Cholesky decomposition performs quite well at Pon A6 - A7, A10 - A11, A15 , A17,

and A21 that the newly generated wave spectra have almost the same significant wave height as input data. To give a clearer evaluation of the results, the percentage of deviation between results and input data is given in Fig.3.26. The deviation rate of the results of Campbell has a sudden jump at Pon A4 due to the numerical transfer function error and increases gradually with the interval distance increases from about 1 percent to a bit bigger than 8 percent. Meanwhile, the Cholesky decomposition is the better method since the deviation rates at locations of 19 pontoons are always below 1 percent and there is no obvious monotone rise trend. Due to the randomness of simulation and only ten times 3-hour short term simulation are carried out, the accuracy may be higher with more conducted cases.

One of ten times short term 100-year homogeneous wave field simulation which is randomly picked is taken as an example here. The spectra of Campbell analogy have smaller integral values than the integral value of the initial Jonswap spectrum that means the spectral energy of the spectra of Campbell analogy is lower. The results of Cholesky decomposition are closer to the initial Jonswap spectrum that is corresponding to the low deviation rate. The mean value of the spectra of two methods is compared with the initial spectrum in Fig.3.28. Regarding the wave peak period, the frequencies where the spectra have their maximum value center on 1.065 rad/s which is the wave peak period of the initial Jonswap spectrum. The frequencies when newly generated wave spectra have their maximum values centering on 1.065 rad/s meaning that the newly generated wave spectra have similar peak periods to the initial data.
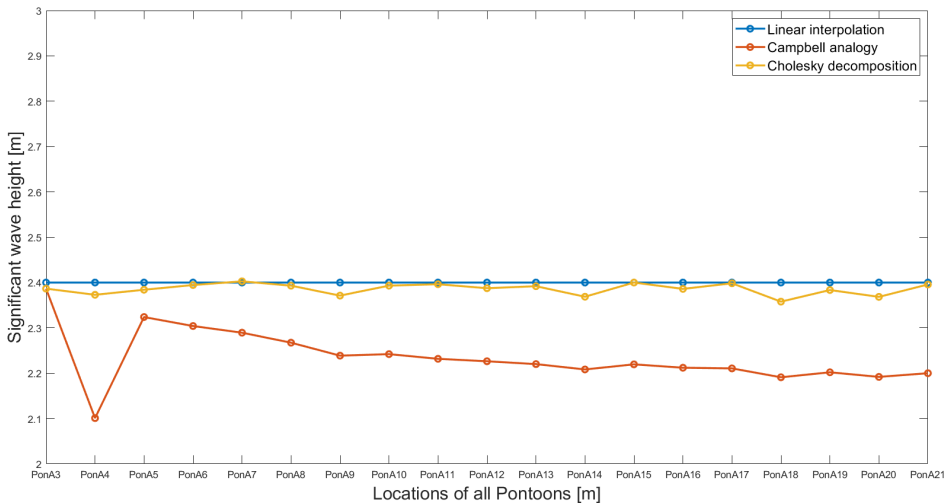
Figure 3.24: Comparison between significant wave height at 19 pontoons of 100-year homogeneous wave condition
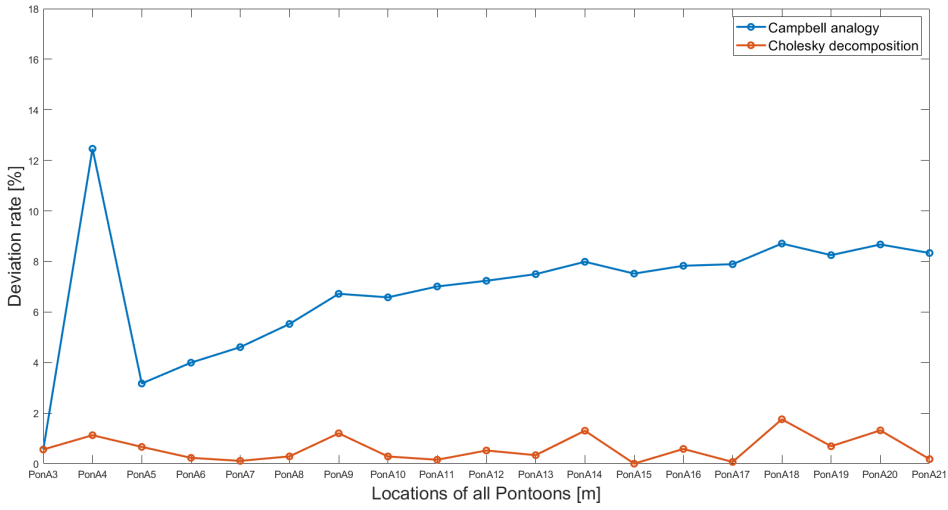
Figure 3.25: Deviation rate of significant wave height of 100-year homogeneous wave condition by two methods
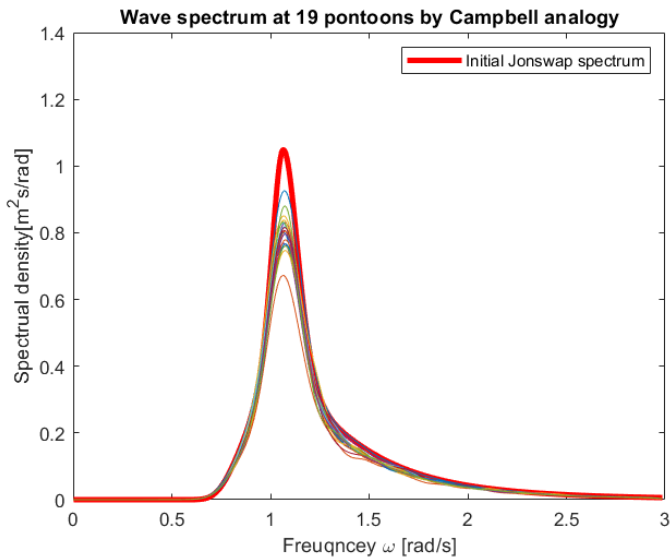
Figure 3.26: Wave spectrum at 19 pontoons of 100-year homogeneous wave condition based on Campbell analogy
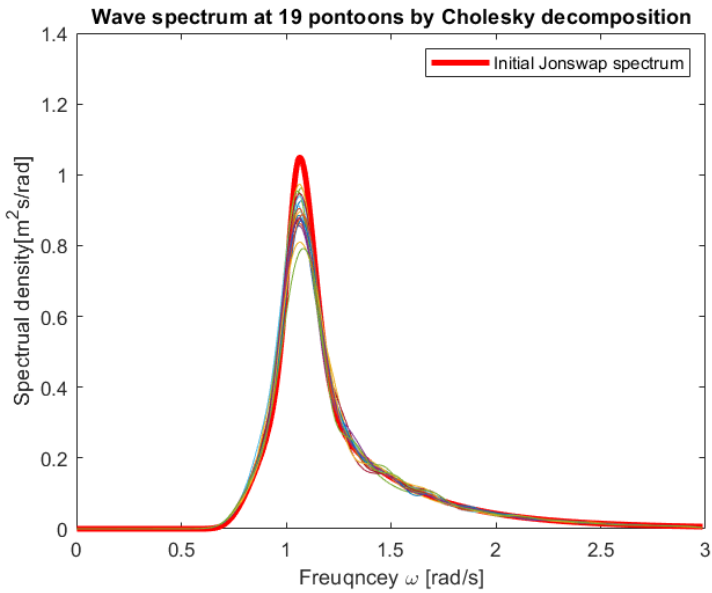
Figure 3.27: Wave spectrum at 19 pontoons of 100-year homogeneous wave condition based on Cholesky decomposition

Figure 3.28: Comparison between mean value of wave spectrum at 19 pontoons of 100-year homogeneous wave condition based on Campbell analogy and Cholesky decomposition
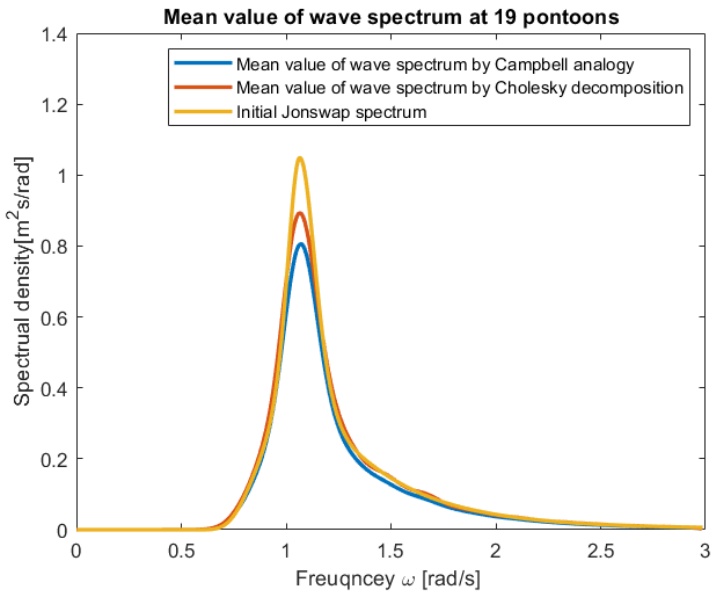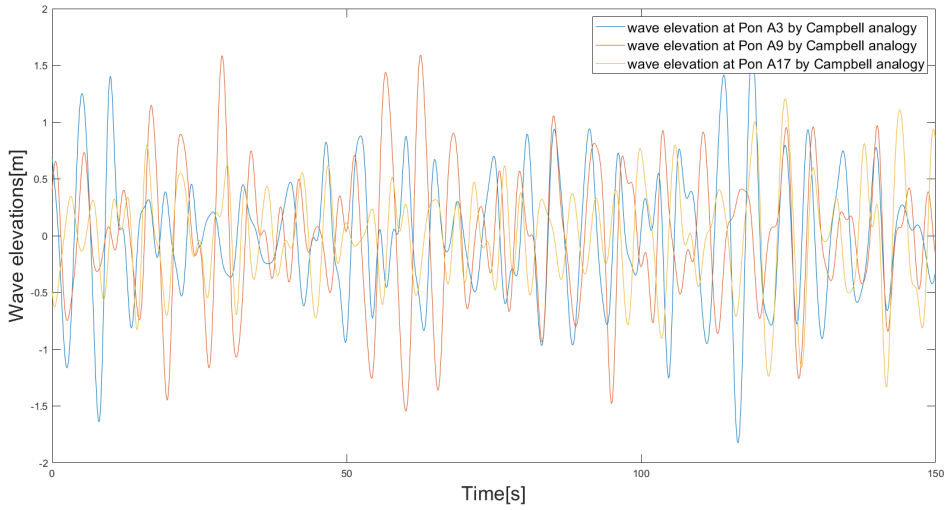
Figure 3.29: Newly generated time series of wave elevations of Pon A3, A9 and A17 by Campbell analogy
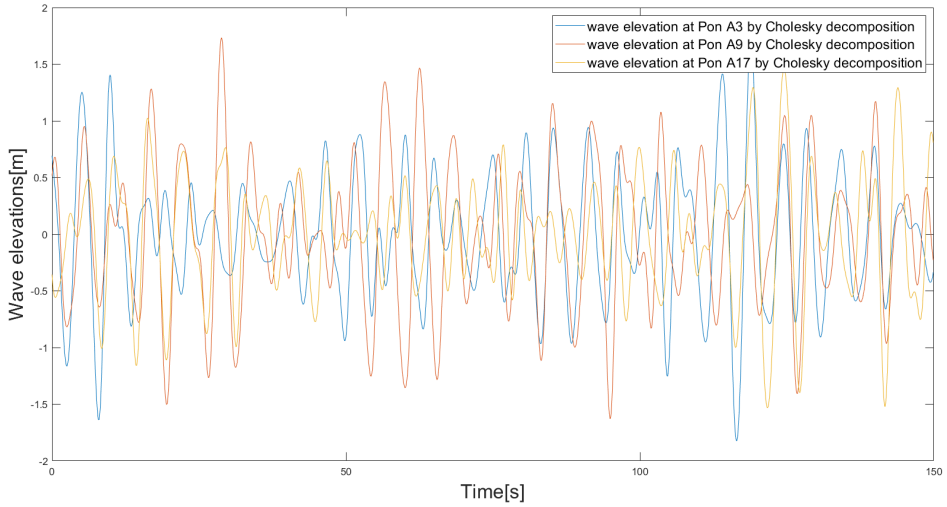

Figure 3.30: Newly generated time series of wave elevations of Pon A3, A9 and A17 by Cholesky decomposition

3.2.3   1-year Inhomogeneous Wave Field Simulation

The inhomogeneous wave field is more realistic compared to the homogeneous wave field simulated before since the inhomogeneity of the wave condition has been proved by the collected data by three DWRs in Cheng's work [7]. The inhomogeneous wave condition by linear interpolation has been studied in Cheng's work [4]. The main difference between 1-year inhomogeneous wave field simulation and 1-year homogeneous wave field simulation is that the input significant wave height H_s for 1-year inhomogeneous wave field simulation are computed by linear interpolation of collected data listed in Table.1.5. In terms of the wave peak period T_p, the input data of inhomogeneous wave conditions are the same as homogeneous wave conditions at 3.77 s. The whole procedure remains the same as before.

The input data by linear interpolation and results generated by Campbell analogy and Cholesky decomposition are tabulated in Table.3.10. The peak wave period of results by both methods are around 3.77 s and the differences are low.

Table 3.10: 1-year inhomogeneous wave condition based on linear interpolation, Campbell analogy and Cholesky decomposition

1-year wave cond.	Linear Interpolation		Campbell analogy		Cholesky decomposition	
Pontoon NO.	H_s	T_p	H_s	T_p	H_s	T_p
A3	1.1	3.77	1.058	3.758	1.058	3.758
A4	1.103	3.77	0.938	3.724	1.059	3.724
A5	1.107	3.77	1.034	3.741	1.061	3.741
A6	1.11	3.77	1.025	3.707	1.064	3.707
A7	1.113	3.77	1.019	3.724	1.066	3.724
A8	1.117	3.77	1.021	3.741	1.080	3.707
A9	1.12	3.77	1.018	3.741	1.085	3.741
A10	1.121	3.77	1.009	3.793	1.075	3.793
A11	1.123	3.77	1.006	3.741	1.074	3.724
A12	1.124	3.77	1.010	3.724	1.084	3.707
A13	1.125	3.77	1.009	3.775	1.087	3.775
A14	1.126	3.77	1.002	3.741	1.080	3.707
A15	1.128	3.77	1.006	3.758	1.088	3.724
A16	1.129	3.77	1.005	3.758	1.088	3.724
A17	1.22	3.77	1.081	3.724	1.169	3.690
A18	1.193	3.77	1.060	3.741	1.153	3.674
A19	1.167	3.77	1.038	3.741	1.124	3.724
A20	1.14	3.77	1.011	3.793	1.102	3.793
A21	1.11	3.77	0.977	3.741	1.060	3.741

The input data and significant wave heights are sketched with respect to the locations of pontoons in Fig.3.31, The results generated by two methods fluctuate with the tendency of the linear interpolation data. It can be seen that the results by Cholesky decomposition are closer to the initial linear interpolation results which indicate that Cholesky decomposition has a better performance than Campbell analogy. Still, the H_s at Pon A4 by Campbell analogy has a significant drop due to the numerical error in programming.

The deviation rate between the results of two methods and the input data are illustrated in Fig.3.32. The error rate of the Cholesky decomposition is about 4 for simulations of all the pontoons. The biggest deviation occurs at the last pontoon Pon A21 with deviation a rate of 4.5 percent. The deviation rate of results computed by Campbell analogy is increasing from 4 percent to about 12 percent depending on the distance separated from the first pontoon, Pon A3 except for the sudden increase at Pon A4 which is corresponding to the drop in Fig.3.31. The average deviation rate, 4 percent, of the Cholesky decomposition for 1-year inhomogeneous wave field is similar to it for 1-year homogeneous wave field shown in Fig.3.18. It can draw a conclusion that the deviation rates of 1-year homogeneous or 1-year inhomogeneous wave condition are at the same level.

Taking one of ten times simulation as an example, the 19 wave spectra computed by Campbell analogy and Cholesky decomposition are sketched in Fig.3.33 and Fig.3.34 respectively. The mean values of the spectra are displayed in Fig.3.35. The mean spectrum of Cholesky decomposition contains higher energy. The newly generated time series of wave elevations of Pon A3, A9, and A17 by Campbell analogy and Cholesky decomposition is shown in Fig.3.36 and Fig.3.37 respectively.
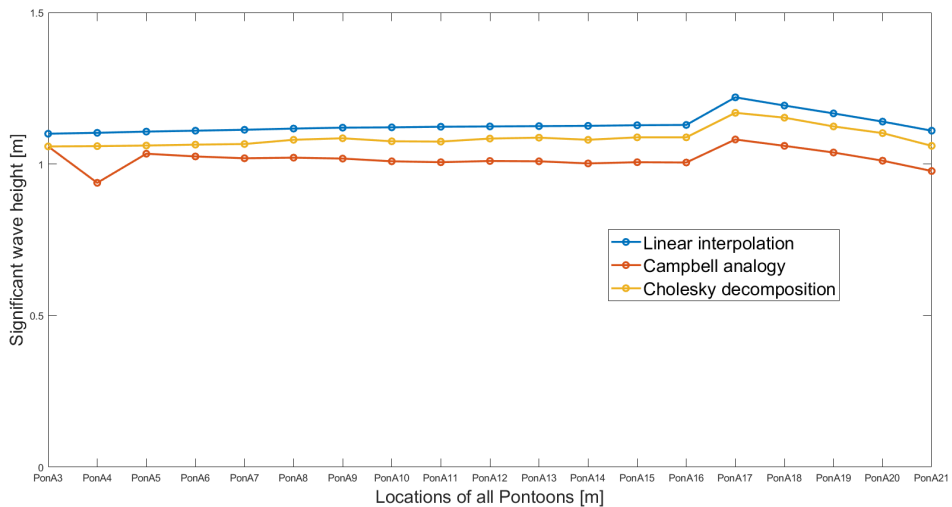
Figure 3.31: Comparison between significant wave height at 19 pontoons of 1-year inhomogeneous wave condition

Figure 3.32: Deviation rate of significant wave height of 1-year inhomogeneous wave condition by two methods
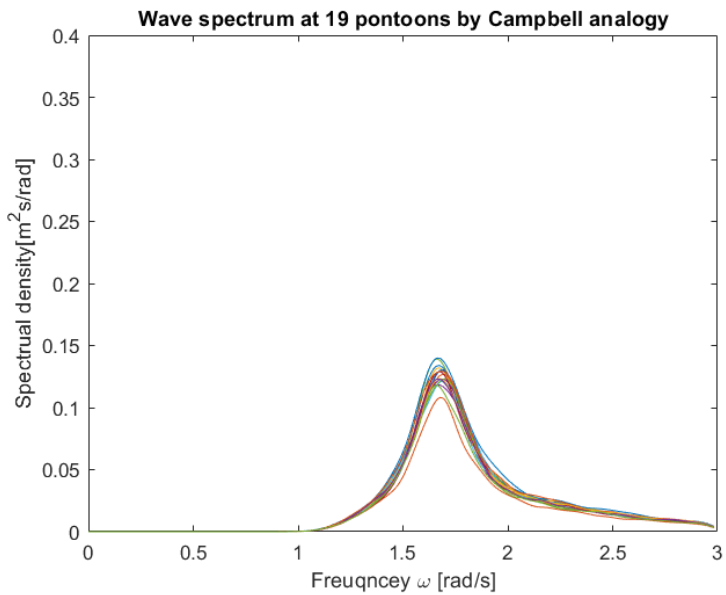
Figure 3.33: Wave spectrum at 19 pontoons of 1-year inhomogeneous wave condition based on Campbell analogy
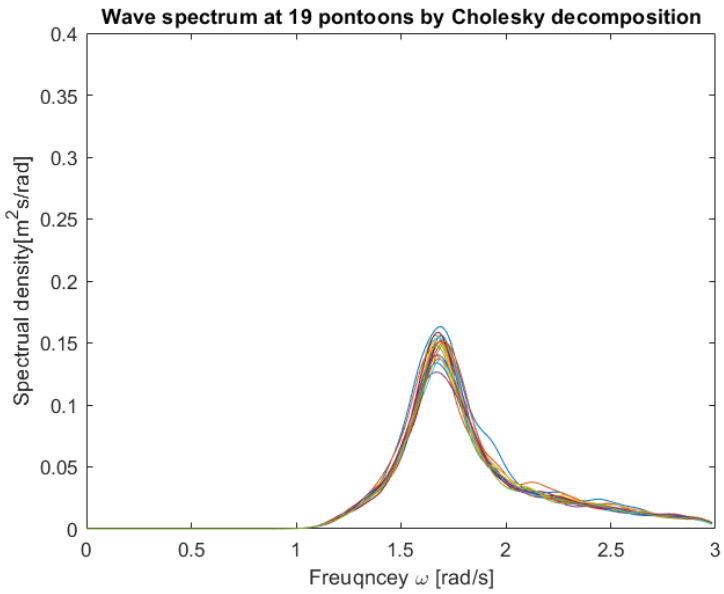
Figure 3.34: Wave spectrum at 19 pontoons of 1-year inhomogeneous wave condition based on Cholesky decomposition
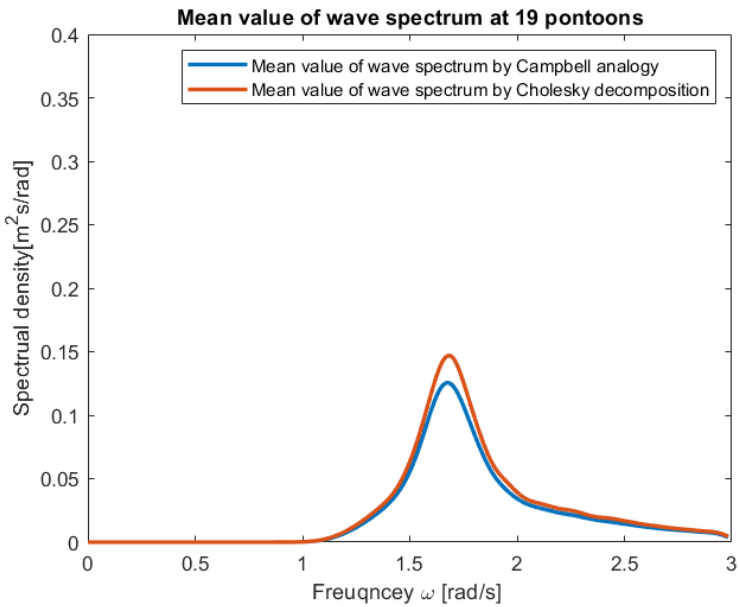
Figure 3.35: Comparison between mean value of wave spectrum at 19 pontoons of 1-year Inhomogeneous wave condition based on Campbell analogy and Cholesky decomposition
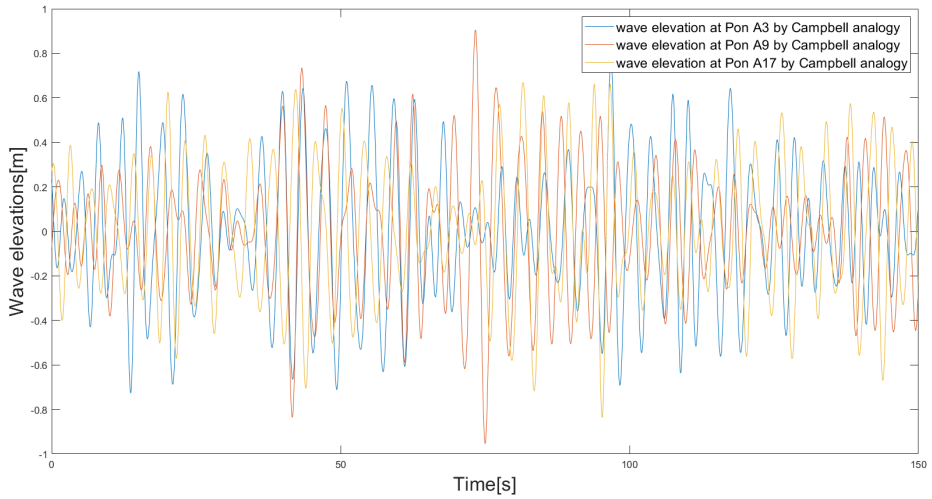
Figure 3.36: Newly generated time series of wave elevations of Pon A3, A9 and A17 by Campbell analogy
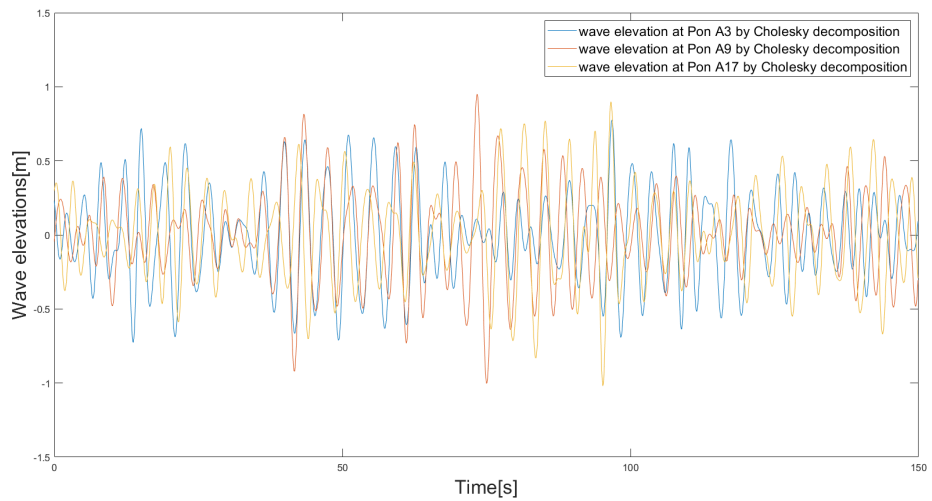
Figure 3.37: Newly generated time series of wave elevations of Pon A3, A9 and A17 by Cholesky decomposition

3.2.4 100-year Inhomogeneous Wave Field Simulation

The initial data of the 100-year inhomogeneous wave condition are computed by linear interpolation of assumed data based on hindcast estimation. The significant wave height varies from the lowest 2.164 m at first pontoon Pon A3 to the highest 2.4 m at pontoon Pon A17. The wave peak period T_p is constantly 5.9 s as before. The results of Campbell analogy and Cholesky decomposition are listed in Table.3.11. The peak periods of newly generated wave spectra are close to the input data since the largest difference is about 0.13 at Pon A12 by Cholesky decomposition.

The significant wave heights of spectra at 19 pontoons generated by two methods are illustrated in Fig.3.38 and the results follow the same trend as the data by linear interpolation. The deviation rates of both results are sketched in Fig.3.39. The results of Cholesky decomposition are better than Campbell analogy since the deviation rate of results of Cholesky decomposition is around 1 percent and the largest error rate is even lower than 2 percent. On the contrary, the deviation rate of Campbell analogy increased from about one percent to a bit over 8 percent which is a rather big gap.

Table 3.11: 100-year inhomogeneous wave condition based on linear interpolation, Campbell analogy and Cholesky decomposition

| 100-year wave cond.	Linear Interpolation		Campbell analogy		Cholesky decomposition	
Pontoon NO.	H_s	T_p	H_s	T_p	H_s	T_p
A3	2.164	5.9	2.151	5.851	2.151	5.851
A4	2.17	5.9	1.910	5.851	2.155	5.851
A5	2.177	5.9	2.101	5.810	2.154	5.810
A6	2.183	5.9	2.090	5.810	2.171	5.810
A7	2.19	5.9	2.071	5.810	2.170	5.810
A8	2.196	5.9	2.052	5.810	2.160	5.810
A9	2.203	5.9	2.053	5.851	2.173	5.810
A10	2.206	5.9	2.053	5.851	2.184	5.851
A11	2.208	5.9	2.039	5.851	2.182	5.851
A12	2.211	5.9	2.040	5.851	2.182	5.769
A13	2.213	5.9	2.043	5.894	2.191	5.851
A14	2.216	5.9	2.044	5.894	2.201	5.851
A15	2.218	5.9	2.042	5.894	2.208	5.894
A16	2.22	5.9	2.040	5.894	2.200	5.894
A17	2.4	5.9	2.206	5.894	2.380	5.851
A18	2.347	5.9	2.152	5.851	2.325	5.810
A19	2.295	5.9	2.102	5.851	2.277	5.851
A20	2.242	5.9	2.061	5.851	2.236	5.851
A21	2.184	5.9	1.999	5.894	2.171	5.851
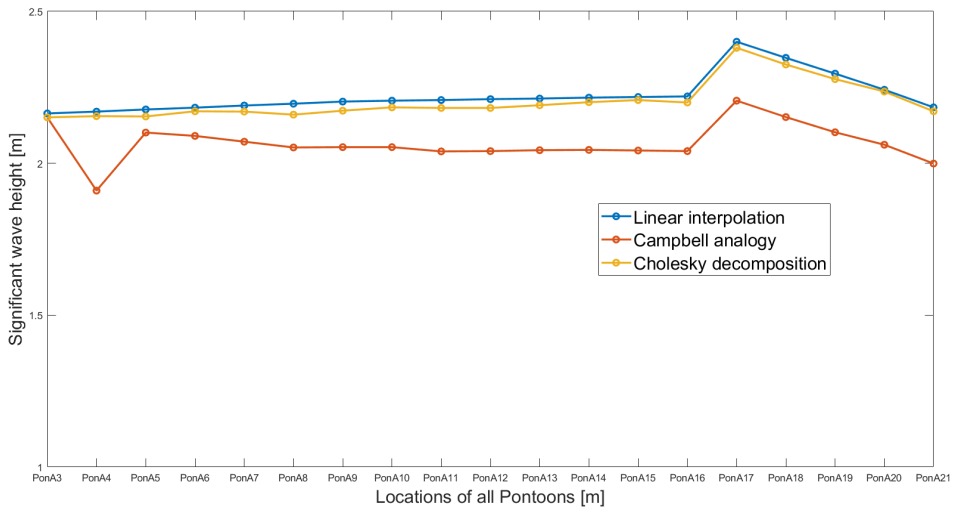
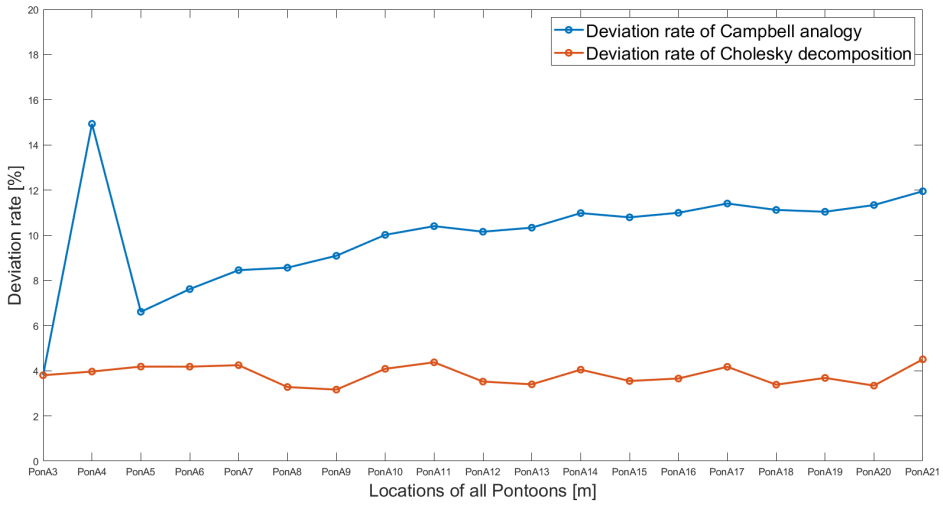**Figure 3.38:** Comparison between significant wave height at 19 pontoons of 100-year inhomogeneous wave condition
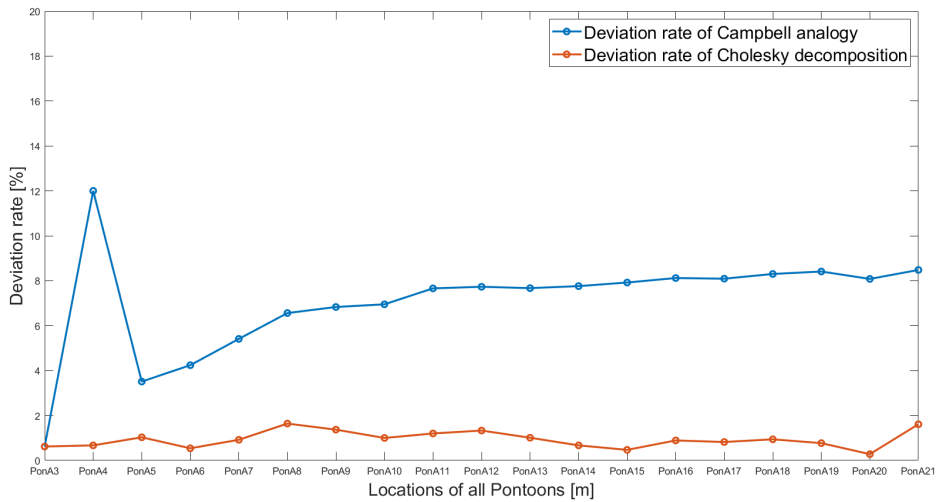
**Figure 3.39:** Deviation rate of significant wave height of 100-year inhomogeneous wave condition by two methods

The wave spectra of 19 pontoons by both methods are displayed in Fig.3.40 and Fig.3.41. The mean values are illustrated in Fig.3.42. Similar as cases analyzed before, the 150 seconds time series of wave elevations generated by Campbell analogy and Cholesky decomposition are depicted in Fig.3.43 and Fig.3.44 respectively.
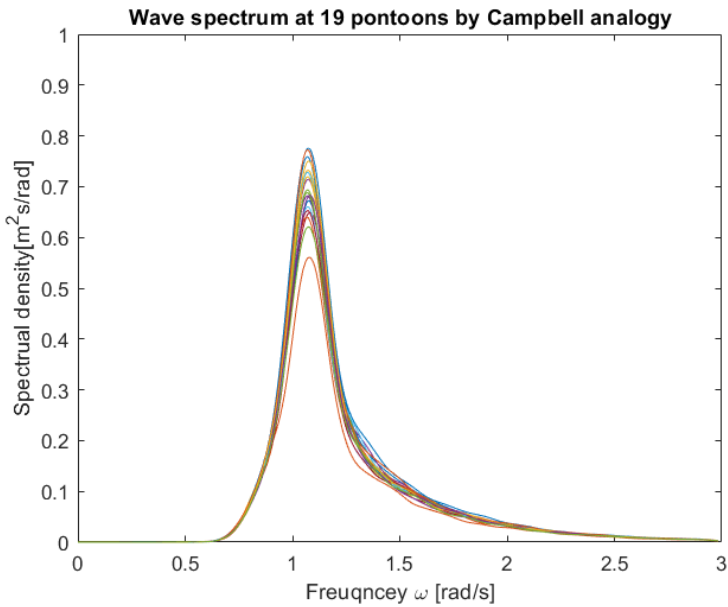
Figure 3.40: Wave spectrum at 19 pontoons of 100-year inhomogeneous wave condition based on Campbell analogy
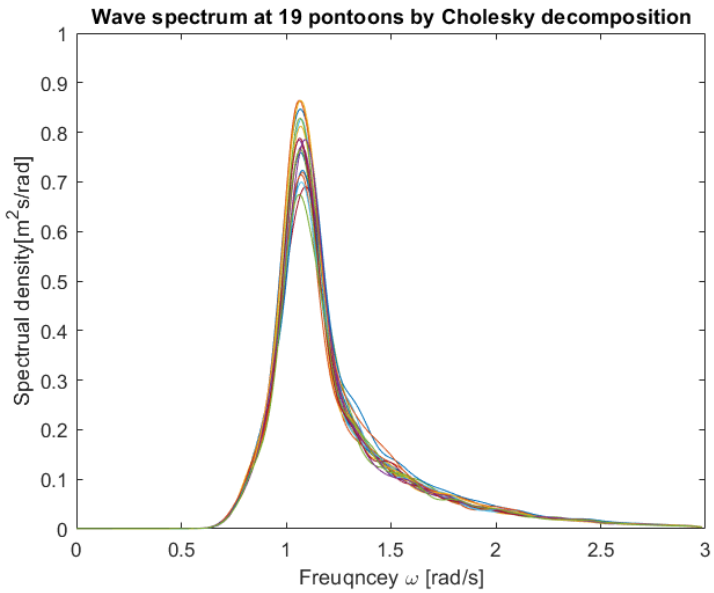
Figure 3.41: Wave spectrum at 19 pontoons of 100-year inhomogeneous wave condition based on Cholesky decomposition

Figure 3.42: Comparison between mean value of wave spectrum at 19 pontoons of 100-year inhomogeneous wave condition based on Campbell analogy and Cholesky decomposition

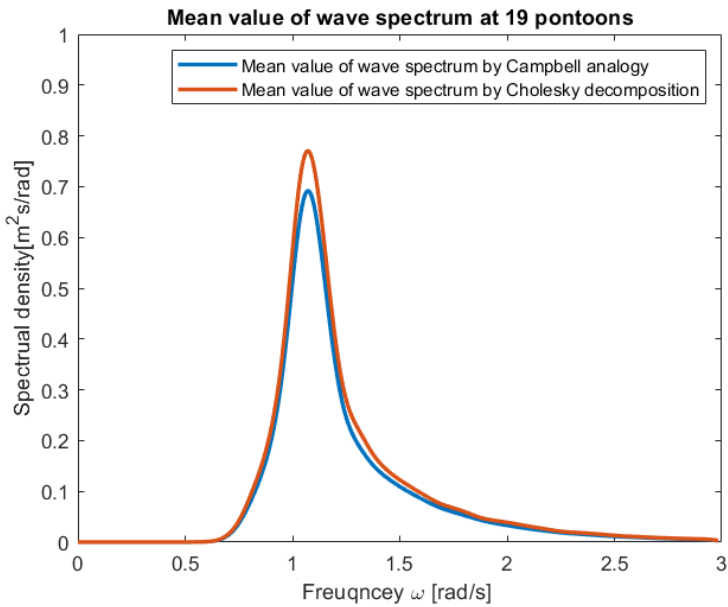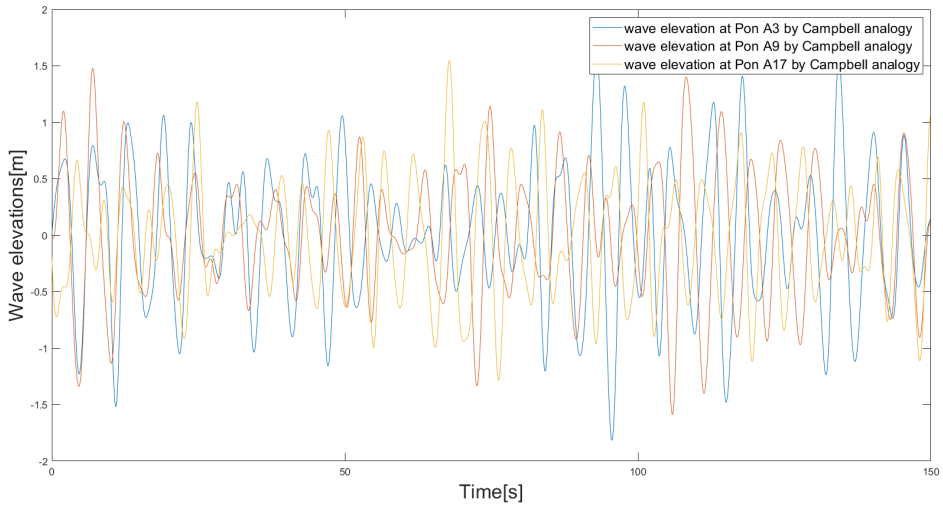**Figure 3.43:** Newly generated time series of wave elevations of Pon A3, A9 and A17 by Campbell analogy
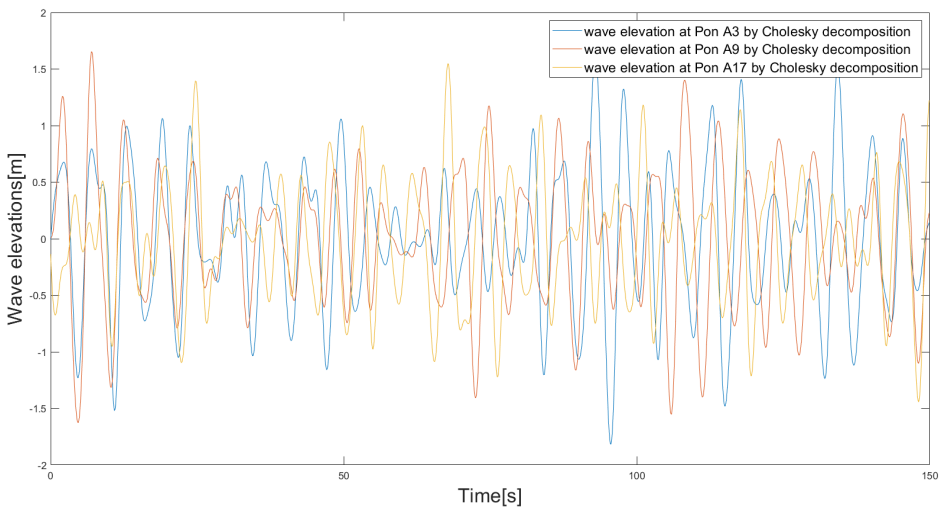

Figure 3.44: Newly generated time series of wave elevations of Pon A3, A9 and A17 by Cholesky decomposition

3.3 Global Dynamic Analysis of The Floating Bridge

In this section, the results of numerical simulation in SIMA will be presented and discussed. The global dynamic response analyses are conducted under both 1-year and 100-year wave conditions including the heave motion, sway motion, axial force along bridge girder, moment about bridge girder strong axis z, bending moment about bridge girder weak axis y, and torsional moment. The simulations were carried out with 4000 s simulation period and 0.1 s simulation step while the time series of wave force contain 4600 s time span which are sufficient to cover the SIMA simulation. The time series of wave force are generated based on identical wave direction 288 [°] for each simulation. The waves are modeled as short crested waves and the second order wave loads were considered.

3.3.1 Wave Load Effects Under 1-year Wave Condition

The wave load effects under 1-year homogeneous wave condition and 1-year inhomogeneous wave condition on the floating bridge are presented as following. Regarding the 1-year wave condition, the wave load effects analyses consist four cases:

Condi. 1) 1-year homogeneous wave condition based on the identical initial data

Condi. 2) 1-year inhomogeneous wave condition based on the inhomogeneous linear interpolated input data

Condi. 3) 1-year inhomogeneous wave condition based on the results computed by the wave field simulation of 1-year homogeneous input data applying Cholesky decomposition method

Condi. 4) 1-year inhomogeneous wave condition based on the results data generated by the wave field simulation of 1-year linear interpolation inhomogeneous input data applying Cholesky decomposition method

To generate time series of wave force, the wave characteristics are supposed to be define first. The Condi. 1 means that the wave force simulation is based on identical H_s and T_p. The Condi. 2 represents that the wave force is simulated by interpolated input data. The Condi. 3 means that the wave force simulation is conducted by results of Cholesky decomposition wave field simulation which is based on the 1-year identical H_s and T_p. The wave force of Condi. 4 is generated based on by results of Cholesky decomposition wave field simulation which is based on the 1-year interpolated input data.

Regarding the wave force simulation, the only homogeneous wave condition is Condi. 1 of what the H_s and T_p are the identical for all pontoon locations and the coherence function is constantly 1 while the coherence function Condi. 2 is constantly 1 as well. In terms of Condi. 3 and Condi. 4, the coherence functions are defined based on the assumed exponential decay coherence structure along the floating bridge.

Table 3.12: 1-year wave condition of generating wave force

| 1-year wave cond.	Condi. 1		Condi. 2		Condi. 3		Condi. 4	
Pontoon NO.	H_s	T_p	H_s	T_p	H_s	T_p	H_s	T_p
A3	1.15	3.77	1.1	3.77	1.106	3.758	1.058	3.758
A4	1.15	3.77	1.103	3.77	1.106	3.828	1.059	3.724
A5	1.15	3.77	1.107	3.77	1.103	3.758	1.061	3.741
A6	1.15	3.77	1.11	3.77	1.109	3.775	1.064	3.707
A7	1.15	3.77	1.113	3.77	1.108	3.775	1.066	3.724
A8	1.15	3.77	1.117	3.77	1.106	3.741	1.080	3.707
A9	1.15	3.77	1.12	3.77	1.110	3.793	1.085	3.741
A10	1.15	3.77	1.121	3.77	1.099	3.793	1.075	3.793
A11	1.15	3.77	1.123	3.77	1.103	3.810	1.074	3.724
A12	1.15	3.77	1.124	3.77	1.107	3.828	1.084	3.707
A13	1.15	3.77	1.125	3.77	1.099	3.793	1.087	3.775
A14	1.15	3.77	1.126	3.77	1.106	3.758	1.080	3.707
A15	1.15	3.77	1.128	3.77	1.103	3.741	1.088	3.724
A16	1.15	3.77	1.129	3.77	1.104	3.775	1.088	3.724
A17	1.15	3.77	1.22	3.77	1.107	3.775	1.169	3.690
A18	1.15	3.77	1.193	3.77	1.102	3.724	1.153	3.674
A19	1.15	3.77	1.167	3.77	1.111	3.758	1.124	3.724
A20	1.15	3.77	1.14	3.77	1.110	3.810	1.102	3.793
A21	1.15	3.77	1.11	3.77	1.109	3.810	1.060	3.741

The wave characteristics which are applied for wave force simulations under four wave condition are shown in Table.3.12. Basically, the significant wave heights and wave peak period for Condi. 1, Condi. 2, Condi. 3, and Condi. 4 are corresponding to the marked column in Table.3.12.

Here the results by Cholesky decomposition methods are considered since the deviation rates are sufficient low comparing with results by Campbell analogy. The time series of wave forces for the four cases are generated by Matlab script provided by Cheng and imported into SIMA simulation.

Inspired by Cheng's work [6] [5], the mean values of the global dynamic analyses are first to be compared in this study. Similarly, the mean values of the heave motion, sway motion, axial force along bridge girder and all the moments analyses are almost identical for these four cases. The mean values of moment about bridge girder strong axis z, moment about bridge girder weak axis y, and torsional moment are taken as examples shown in Fig.3.45(a), Fig.3.45(b), and Fig.3.45(c) respectively. The mean value of the axial force is illustrated in appendix Fig.4.1. In general, the mean values of global dynamic responses of the floating bridge are not sensitive to the inhomogeneous wave condition and the wave condition simulated by newly generated data. Therefore, the analyses are mainly focused on the dynamic part of the global responses.
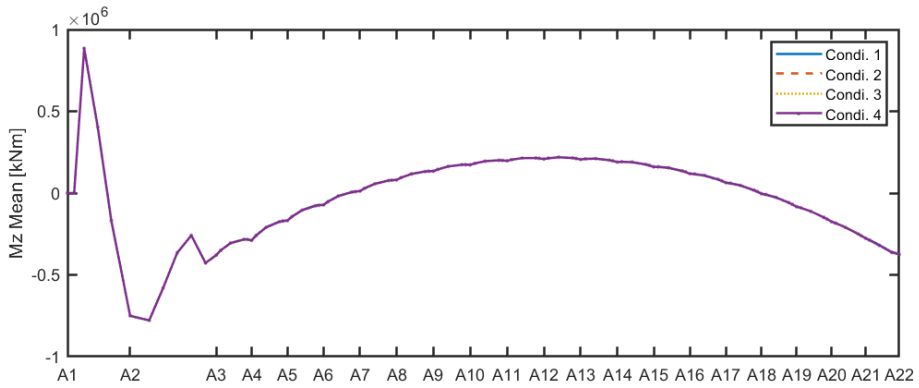
(a) Moment about bridge girder strong axis, M_z
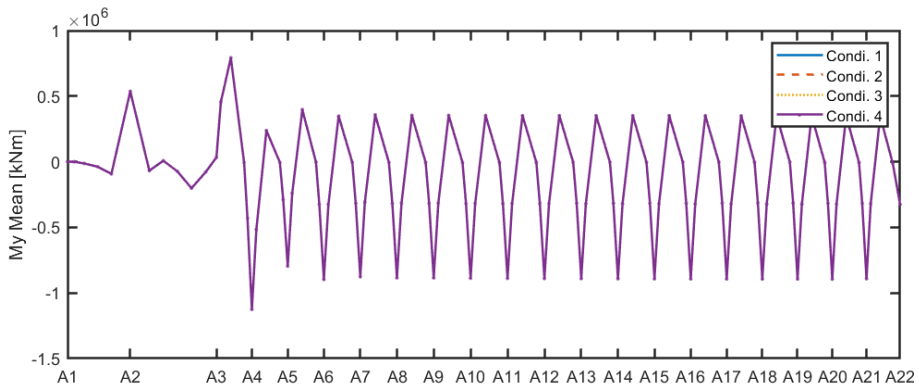
(b) Moment about bridge girder weak axis, M_y
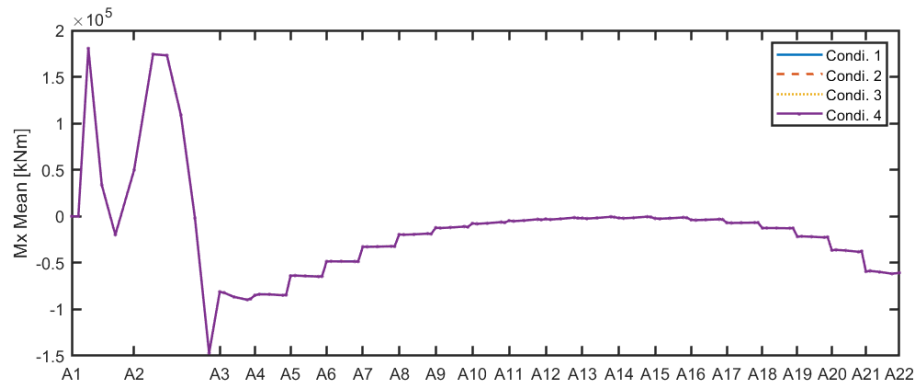
(c) Torsion moment, M_x

Figure 3.45: The mean value of (a) moment about bridge girder strong axis, M_z, (b) moment about bridge girder weak axis, M_y, (c)torsion moment, M_x, along the bridge girder under 1-year wave condition.

(a) Sway motions
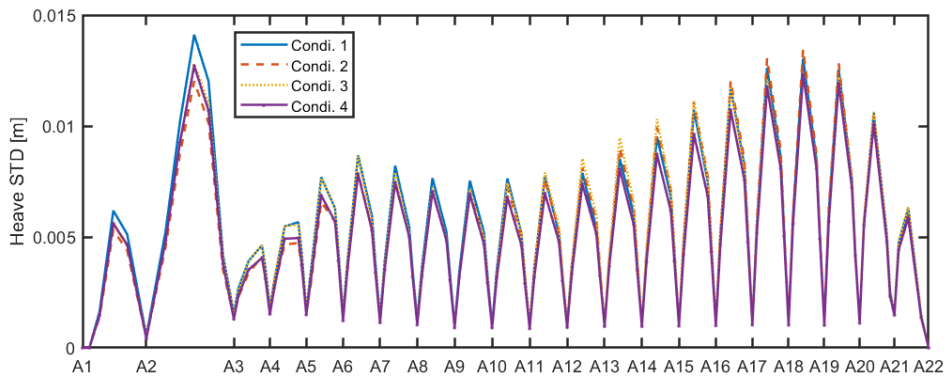
(b) heave motions

Figure 3.46: The standard deviation of (a) sway motions, (b) heave motion along the bridge girder under 1-year wave condition

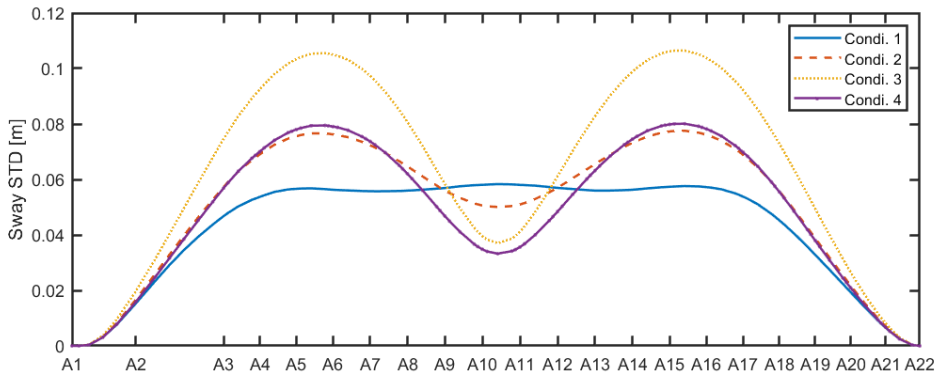The sway motion of the floating bridge girder is researched by computing the standard deviation. The standard deviation of sway motion of the floating bridge under for wave conditions from Condi. 1 to Condi. 4 is illustrated in Fig.3.46(a). On the whole, the homogeneous wave condition simulated by Cholesky decomposition Condi. 3 gives the largest standard deviation which is about 0.11 m. The standard deviation under Condi. 2 and Condi. 4 are quite similar except from pontoon Pon A8 to Pon A13 where the Condi. 4 cause smaller sway standard deviation meaning that the simulation of 1-year inhomogenous wave condition are proved effectively and sufficiently. Regarding the standard deviation of Condi. 1, the results seem a bit wrong which looks different from Cheng's thesis [6]. That should be checked in future work.

The standard deviation of heave motion is illustrated in Fig.3.46(b). The homogeneous wave condition Condi. 1 has the largest standard deviation between Pon A1 to Pon A11

while the simulated homogeneous wave condition Condi. 3 gives the largest standard deviation from Pon A11 to the end Pon A22. The simulated inhomogeneous wave condition Condi. 4 cause the smallest standard deviation over the floating bridge. But the gaps of standard deviation between each wave condition are rather low.

The standard deviation of axial force F_x along the floating bridge girder under four wave conditions is sketched in Fig.3.47. Overall, the homogeneous wave condition Condi. 1 causes the largest axial force and the simulated homogeneous wave condition Condi. 3, inhomogeneous wave condition Condi .2, simulated inhomogeneous wave condition Condi .4 give smaller standard deviation in turn. The standard deviation of the moment about strong axis M_z, the moment about weak axis M_y and the torsional moment M_x along the bridge girder are presented in Fig.3.48(a), Fig.3.48(b), and Fig.3.48(c) respectively. Comparing with the moment about weak axis M_y, the moment about strong axis M_z and the torsional moment M_x are more sensitive to inhomogeneous wave conditions since there are noticeable gaps between wave conditions in illustrated figures. In terms of the standard deviation of the moment about strong axis M_z, the simulated homogeneous wave condition Condi. 3 gives largest standard deviation between Pon A1 to Pon A2, Pon A4 to Pon A8, Pon A12 to Pon A17, and Pon A20 to Pon A22 while the rest part are occupied by the homogeneous wave condition Condi. 1. Regarding the standard deviation of the moment about weak axis M_y, the gaps between each wave condition are quite small and the Condi. 1 and Condi. 3 give almost same largest standard deviation along the bridge. For the standard deviation the torsional moment M_x, the Condi. 1 causes the largest standard deviation at the majority parts along the bridge.

To conclude, the homogeneous wave condition Condi. 1 can result in larger heave motion, bending moment and axial force compared to other three wave conditions. Additionally The sway motion of Condi. 1 should be examined further. The analyses indicate that the wave field simulations which are corresponding to the Condi. 2, Condi. 3 and Condi. 4 cause a lower effect on the global dynamic responses.
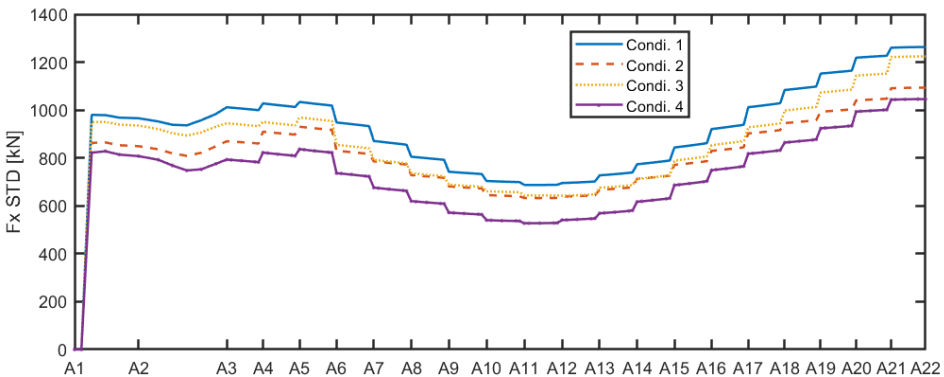
Figure 3.47: The standard deviation of axial force F_x along the bridge girder under 1-year wave condition
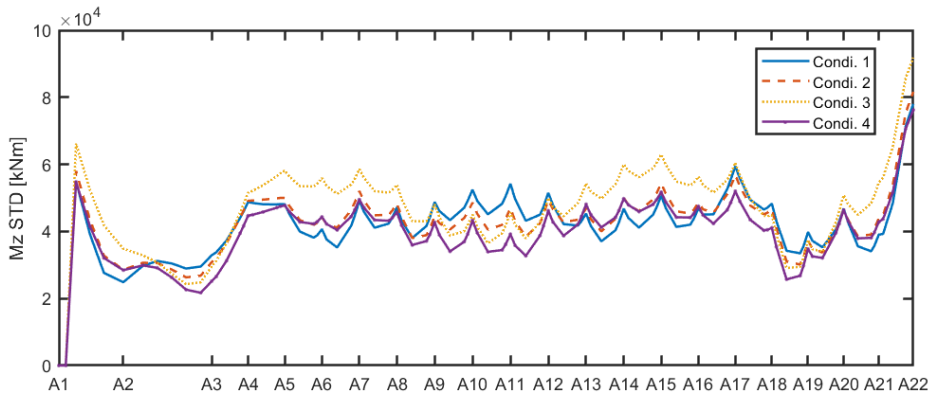
(a) Moment about bridge girder strong axis, M_z
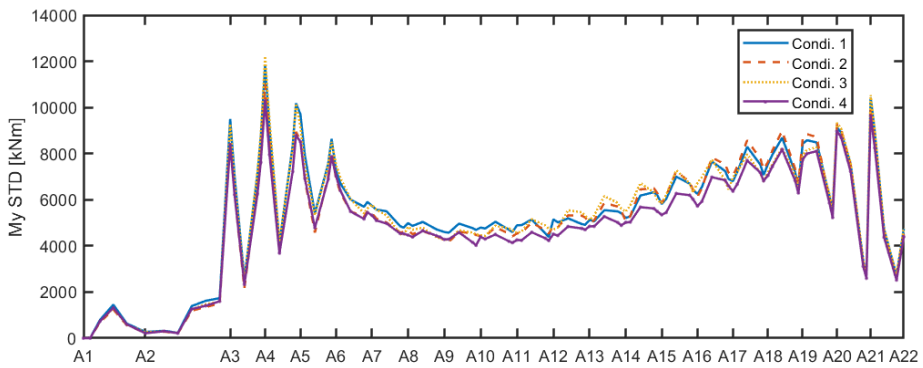
(b) Moment about bridge girder weak axis, M_y
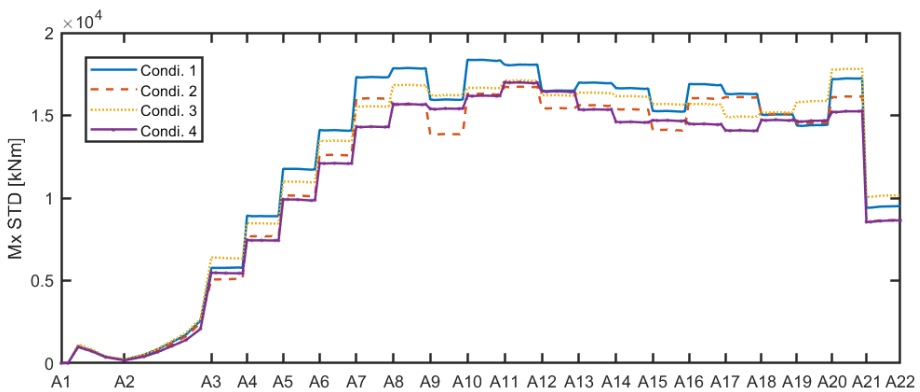
(c) Torsion moment, M_x

Figure 3.48: The standard deviation of (a) moment about bridge girder strong axis, M_z, (b) moment about bridge girder weak axis, M_y, (c)torsion moment, M_x, along the bridge girder under 1-year wave condition.

3.3.2 Wave Load Effects Under 100-year Wave Condition

The wave load effects under 100-year homogeneous wave condition and 100-year inhomogeneous wave condition on the floating bridge are presented as below. Regarding the applied 100-year wave condition, the wave load effects analyses consist four cases:

Condi. 1) **100-year homogeneous wave condition based on the identical initial data**

Condi. 2) **100-year inhomogeneous wave condition based on the inhomogeneous linear interpolated input data**

Condi. 3) **100-year inhomogeneous wave condition based on the results computed by the wave field simulation of 1-year homogeneous input data applying Cholesky decomposition method**

Condi. 4) **100-year inhomogeneous wave condition based on the results data generated by the wave field simulation of 1-year linear interpolation inhomogeneous input data applying Cholesky decomposition method**

Table 3.13: 1-year wave condition of generating wave force

| 100-year wave cond.	Condi. 1		Condi. 2		Condi. 3		Condi. 4	
Pontoon NO.	H_s	T_p	H_s	T_p	H_s	T_p	H_s	T_p
A3	2.4	5.9	2.164	5.9	2.387	5.851	2.151	5.851
A4	2.4	5.9	2.17	5.9	2.373	5.894	2.155	5.851
A5	2.4	5.9	2.177	5.9	2.384	5.894	2.154	5.810
A6	2.4	5.9	2.183	5.9	2.394	5.851	2.171	5.810
A7	2.4	5.9	2.19	5.9	2.403	5.851	2.170	5.810
A8	2.4	5.9	2.196	5.9	2.393	5.980	2.160	5.810
A9	2.4	5.9	2.203	5.9	2.371	5.936	2.173	5.810
A10	2.4	5.9	2.206	5.9	2.393	5.936	2.184	5.851
A11	2.4	5.9	2.208	5.9	2.396	5.894	2.182	5.851
A12	2.4	5.9	2.211	5.9	2.387	5.894	2.182	5.769
A13	2.4	5.9	2.213	5.9	2.392	5.936	2.191	5.851
A14	2.4	5.9	2.216	5.9	2.369	5.980	2.201	5.851
A15	2.4	5.9	2.218	5.9	2.400	5.894	2.208	5.894
A16	2.4	5.9	2.22	5.9	2.386	5.894	2.200	5.894
A17	2.4	5.9	2.4	5.9	2.398	5.851	2.380	5.851
A18	2.4	5.9	2.347	5.9	2.358	5.810	2.325	5.810
A19	2.4	5.9	2.295	5.9	2.383	5.894	2.277	5.851
A20	2.4	5.9	2.242	5.9	2.368	5.936	2.236	5.851
A21	2.4	5.9	2.184	5.9	2.396	5.810	2.171	5.851

Similarly as 1-year wave condition, the Condi. 1 to Condi. 4 of 100-year wave condition have the corresponding wave characteristics listed in Table.3.13. Regarding the coherence functions of the four wave conditions, the coherence functions of Condi. 1 and Condi. 2 are constantly 1 while the coherence functions of Condi. 3 and Condi. 4 are obtained from the assumed coherence structure along the floating bridge.

Similar as the four cases of wave load effect analyses under 1-year wave condition, the mean values of analyses about sway motion, heave motion, axial force, moment about bridge girder strong axis M_z, moment about bridge girder weak axis M_y, and torsional moment M_x under 100-year wave condition shown in appendix 4.4 are likewise almost identical which can be neglected in this section. Only the dynamic part of the global responses is investigated as following.

The sway motion of the floating bridge girder is investigated by computing the standard deviation of it. The Fig.3.49(a) depicts the standard deviation of the sway motion of the floating bridge girder under Condi. 1 to Condi. 4. Overall, the 100-year inhomogeneous wave condition by simulation, Condi. 4 causes the largest sway motion at around pontoon Pon A5 and Pon A15 while it gives the smallest sway motion at between Pon A10 an Pon A11. The largest standard deviation is about 0.38 m. The standard deviation of Condi. 3 is a bit larger than the standard deviation of Condi. 1 which indicates that the simulation of the 100-year homogeneous wave condition is rational. The 100-year inhomogeneous wave condition by linear interpolation gives a lowest standard deviation at a great proportion of pontoons and is significantly different from the 100-year inhomogeneous wave condition by simulation, Condi. 4 meaning that the sway motion is quite sensitive to the way of simulating inhomogeneous wave condition.

In terms of the heave motion, the standard deviation of heave motion of the floating bridge under four wave conditions is illustrated in Fig.3.49(b). In general, the standard deviation of heave motions is not as sensitive to the wave conditions as standard deviation of sway motions. The 100-year homogeneous wave condition by simulation Condi. 3 gives the largest standard deviation from Pon A1 to Pon A20 which can be regarded all over the floating bridge. The Condi. 4 causes the smallest standard deviation across the bridge but the gaps between each wave condition are rather low.

The observations of heave motions under 100-year wave condition are different from the results of heave motions under 1-year wave condition. The Condi. 4 gives the largest standard deviation under 100-year wave condition while The Condi. 3 causes the largest sway motion over the floating bridge. This may due to the Condi. 4 under 100-year wave condition is close to the resonant period which causes resonance. To further reveal the reasons, the spectrum of sway motion should be studied in future work.
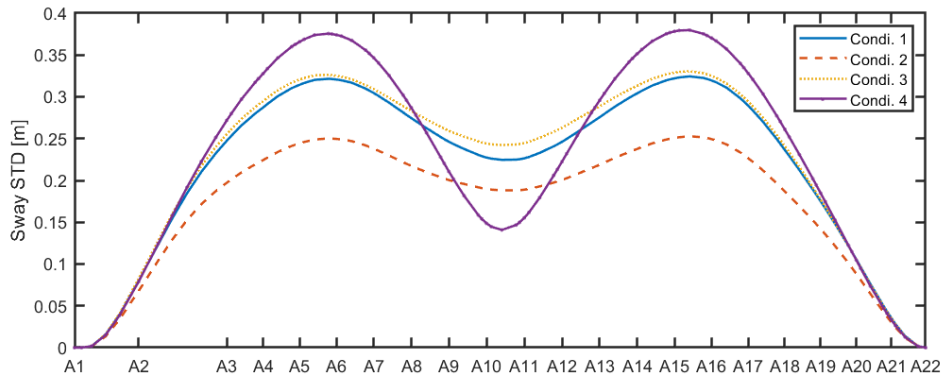
(a) Sway motions
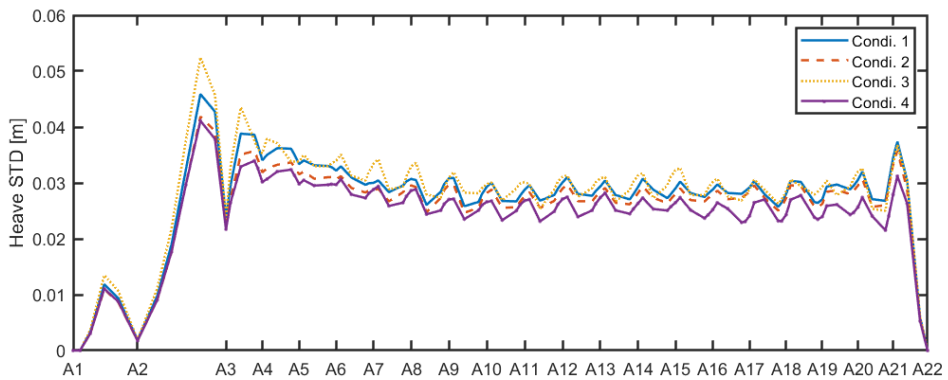
(b) heave motions

Figure 3.49: The standard deviation of (a) sway motions, (b) heave motion along the bridge girder under 100-year wave condition

The standard deviation of axial force F_x under four wave conditions is illustrated in Fig.3.50. In general, the 100-year homogeneous wave condition Condi. 1 has the largest standard deviation along the floating bridge girder while the 100-year homogeneous wave condition by simulation Condi. 3 has a bit higher standard deviation than Condi. 1 between Pon A7 to Pon A13 but the difference is very small. On the contrary, the 100-year homogeneous wave condition by simulation Condi. 4 gives the lowest standard deviation except from Pon A9 to Pon A13 where the Condi.2 has the lowest standard deviation. By observing the results of the standard deviation of axial force, the simulation about 100-year homogeneous and inhomogeneous wave condition give good feedback.
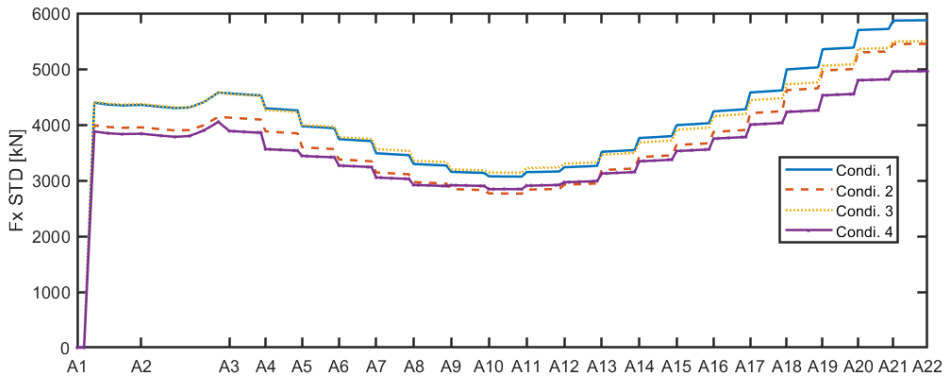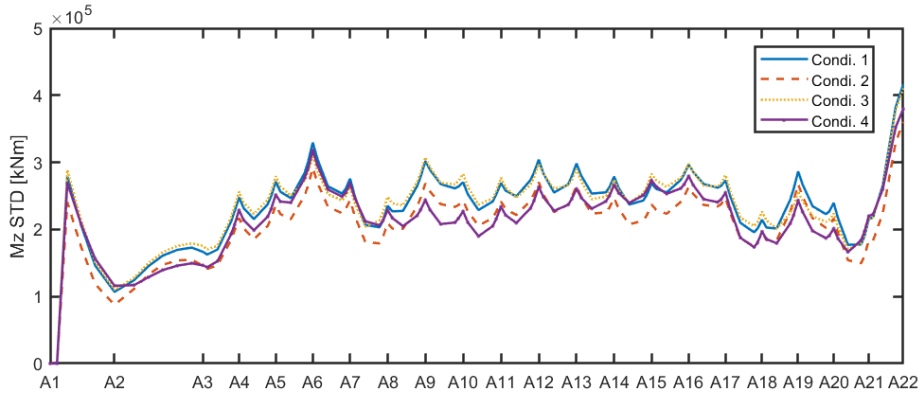
Figure 3.50: The standard deviation of axial force F_x along the bridge girder under 100-year wave condition
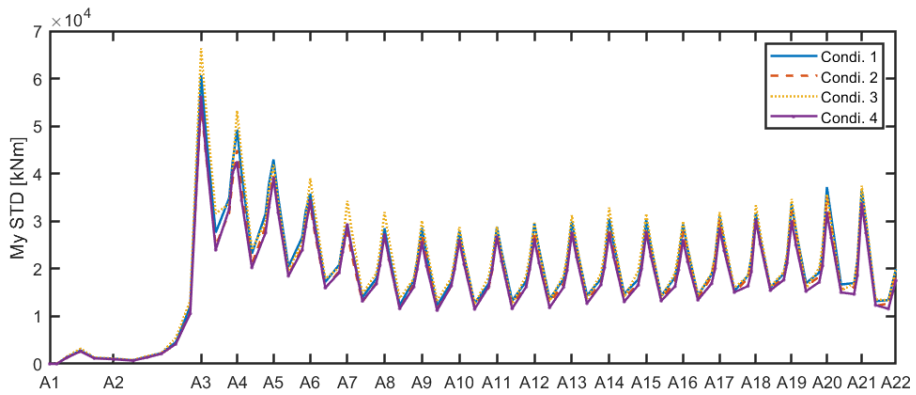
The standard deviation of the moment about strong axis M_z, the moment about weak axis M_y and the torsional moment M_x along the bridge girder are presented in Fig.3.51(a), Fig.3.51(b), and Fig.3.51(c) respectively. Similarly, the moment about strong axis M_z and the torsional moment M_x are more sensitive to inhomogeneous wave conditions compared with the moment about weak axis M_y. Regarding the moment about strong axis M_z, the 100-year homogeneous wave condition Condi. 1 and 100-year homogeneous wave condition by simulation Condi. 3 cause the highest standard deviation along the bridge together. The 100-year inhomogeneous wave condition Condi. 2 gives the lowest standard deviation between Pon A1 to Pon A2,Pon A4 to Pon A8,Pon A14 to Pon A17, and Pon A20 to Pon A22 while the lowest standard deviation rest part of bridge are resulted by simulated 100-year inhomogeneous wave condition Condi. 4. In terms of The standard deviation of the moment about weak axis M_y, the gaps between each wave condition are pretty narrow. The Condi. 3 gives the highest standard deviation over the floating bridge while the Condi. 4 has the lowest standard deviation. As far as the standard deviation of torsional moment M_x concerned, the Condi 1 causes the largest standard deviation along the bridge except between Pon A3 to Pon A5 and Pon A7 to Pon A10 where the Condi. 3 gives the highest torsional moment. Similar as the moment about strong axis M_z, the lowest standard deviation is resulted from Condi. 2 and Condi. 4 together.

To summarize, the 100-year homogeneous wave condition Condi.1 and simulated 100-year homogeneous wave condition Condi.3 result in larger response with respect to heave motions, axial force, strong axis bending moment and weak axis bending moment. The simulated 100-year inhomogeneous wave condition Condi.4 causes the larger sway motion.

(a) Moment about bridge girder strong axis, M_z

(b) Moment about bridge girder weak axis, M_y
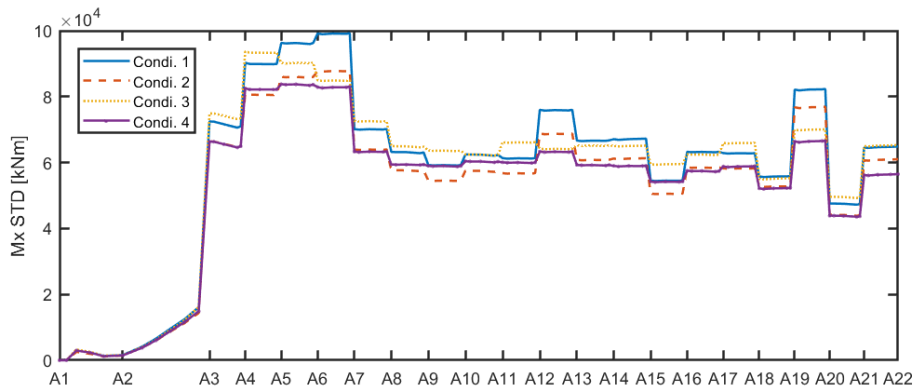
(c) Torsion moment, M_x

Figure 3.51: The standard deviation of (a) moment about bridge girder strong axis, M_z, (b) moment about bridge girder weak axis, M_y, (c)torsion moment, M_x, along the bridge girder under 100-year wave condition.

Chapter 4

Conclusion

The Norwegian Public Roads Administration (NPRA) has launched The Ferry-free E39 Coastal Highway Route project in order to reduce the travel time from 21 hours to 11 hours between Trondheim and Kristiansand by applying bridges and tunnels to replace the current fjord ferries. In this study, one of the seven fjords, Bjørnafjorden is focused. The end-anchored curved floating bridge which is a long curved structure of 5 km supported by 19 was proposed to cross Bjørnafjorden. To simulate the inhomogeneous wave condition in the fjord and estimate the global dynamic responses of the floating bridge, several investigations are conducted in this thesis:

- Introduction about basic stochastic theory for the basis of creating filter functions matrix and coherence structure along the fjord.

- The numerical procedure of generating time series of wave elevations at 19 pontoons are developed.

- Several cases are carried out for verifying the two methods, Campbell analogy and Cholesky decomposition

- The developed two methods are applied for simulating the wave field along the floating bridge at each pontoon.

- The comparisons between the results of simulated 1-year, 100-year homogeneous wave condition and 1-year, 100-year inhomogeneous wave condition are presented.

- The global dynamic motions of the floating bridge under four wave conditions are analyzed.

4.1 Basic Stochastic Theory And Methods For Wave Field Simulation

In this thesis, the basic stochastic theories are introduced as a basis for developing the methods for wave field simulation. The fundamental theories including the definitions of auto-correlation, cross-correlation spectrum, spectral density function, and directional wave spectrum. Additionally, the way to calculating the wave characteristics, significant wave height H_s and wave peak period T_p is introduced. The Jonswap spectrum is implemented in this study as the basic form of wave spectrum. Furthermore, the coherence functions are derived and the coherence structure along the fjord specifically at each pontoon supporting the floating bridge is assumed. The form of the coherence function is proposed as exponential decay while the coherence value is a constant number with respect to frequencies shown in Fig.2.10.

According to Campbell's theory [3], the matrix form of filter functions connecting the Gaussian white noise and wave elevation are developed based on the given input wave characteristics and matrix of wave spectra. During the procedure, two methods which are named Campbell analogy and Cholesky decomposition are developed. The Campbell analogy method is come from the derivation of the theories introduced in Campbell's theory [3] and creates the transfer matrix **H** by analogy. The Cholesky decomposition method is to using Cholesky decomposition to the matrix of wave spectra in order to obtain the **L** matrix which is the transfer matrix for generating wave elevations. Based on the theory of Campbell, the assumption is that the first point will affect the other point while there are no reverse effects from the points behind and the pontoon Pon A3 is set as the first point in this thesis. Note that the two methods should compute the transfer matrix with same components but the implementations in programming are different for the two methods. The combination of the time series of Gaussian white noise and transfer matrix will lead to the times series of wave elevation considering the coherence structure so that the homogeneous and inhomogeneous wave field can be simulated along the floating bridge specifically at 19 pontoons.

The times series of wave forces are generated by a Matlab script provided by Cheng. The simulation of SIMA which is used for computing global dynamic responses requires the time series of wave force imported as external excitation force to estimate the inhomogeneous wave condition.

4.2 Simulation And Results

What followed is to conduct the wave field simulation and the global dynamic responses based on the simulated wave condition by the software SIMA.

To examine the two methods, one-point and two-point cases are conducted. Regarding the one-point case, the two wave characteristics of the results of simulation by decom-

posing the wave spectrum by definition (2.3) and by using the transfer function are quite close to the input data 2.0 m H_s which indicates the procedure works for the one-point case. Compared with the one-point case, the two-point case contains a variety of hypotheses simulations including independent two-point simulation, fully correlated two-point simulation, and two-point simulation with assumed coherence function. The coherence function and wave elevations of each case prove the assumption of the relationship. All the simulations have the good results that the wave characteristics can return to the initial data with a low error smaller than 0.01 m for significant wave height H_s.

The simulation of wave field along the floating bridge at Bjørnafjorden is carried out which means the assumed coherence structure of the fjord is supposed to be taken into consideration. The simulations are designed for four wave conditions which are 1-year, 100-year homogeneous wave field, and 1-year, 100-year inhomogeneous wave field. The main criterion of defining the inhomogeneity is that if input significant wave heights at 19 pontoons are not identical. For every simulation of the floating bridge in this thesis, the wave direction θ_p is considered constantly 288 [°] while the phase angle ϕ is randomly generated independently. For each simulation, two methods, Campbell analogy and Cholesky decomposition are applied to generate the time series of wave elevations.

To summarize, by comparing the results of all the simulations, the Cholesky decomposition is the better method for wave field simulation in this study since the deviation rates are always stably lower than the deviation rates of Campbell analogy. The results of Campbell analogy have a gradually increase on the deviation rate with the separated distance from the first pontoon Pon A3 which is not acceptable and the accuracy of Campbell analogy always has a drop at the second point in simulation due to the numerical error. By observing The Cholesky decomposition performs better for homogeneous and inhomogeneous 100-year wave condition with deviation rate fluctuating around 1 percent than for homogeneous and inhomogeneous 1-year wave condition with deviation rate fluctuating around 4 percent. Due to the randomness inside the wave simulation procedure, the simulated homogeneous wave can not return to initial homogeneous wave so that the homogeneous wave condition from the simulation is actually not the real homogeneous wave condition but inhomogeneous wave condition. The situation may be improved by implementing plenty of times simulations.

The global dynamic responses are carried out by SIMA. The global dynamic response analyses are conducted under both 1-year and 100-year, homogeneous and inhomogeneous wave condition including the heave motion, sway motion, axial force along bridge girder, moment about bridge girder strong axis z, bending moment about bridge girder weak axis y, and torsional moment. The mean values of 1-year and 100-year wave conditions are not necessary to analyze since the mean values are almost identical under all wave conditions. Regarding the 1-year wave condition, the homogeneous wave condition based on initial data in Table.3.8 has the largest standard deviation which corresponds to the largest global dynamic response along the floating bridge. In terms of the 100-year wave condition, the 100-year homogeneous wave condition and simulated 100-year homogeneous wave condition give the largest standard deviation with respect to heave motions, axial force, strong

axis bending moment and weak axis bending moment. But the the simulated 100-year in-homogeneous wave condition causes the larger sway motion. All the results are compared with the results in Cheng's work [6] and the values of computed results in this thesis are considered rational. In addition, the wave directions may have effects on the motion of the floating bridge but the wave directions are identical along the floating bridge in this thesis.

4.3   Future work

The Future work could contain several points including :

- The relationship between the coherence structure and phase angle applied in generated wave elevations. In this study, the phase angle is not correlated with the coherence function and is generated randomly between $[0,2\pi]$.

- The accuracy of two methods could be double checked by implementing more times simulations.

- Check the results of standard deviation of sway motion under 1-year homogeneous wave condition with initial data. The values seem not same as the results in Cheng's work [6].

- The sensitivity check should be done for the phase angle used in generated time series of wave force. In Cheng's work [6], the cases of generating time series of wave force includes identical phase angle simulation and different phase angle simulation.

- The spectrum of sway, heave motions of the floating bridge are supposed to be investigated to understand the resonance condition.

- The effect on the global dynamic motion of the floating bridge from different wave directions should be studied.

Bibliography

[1] *A Time-Domain Method for Hydroelastic Analysis of Floating Bridges in Inhomogeneous Waves*, volume Volume 9: Offshore Geotechnics; Torgeir Moan Honoring Symposium of *International Conference on Offshore Mechanics and Arctic Engineering*, 06 2017. V009T12A010.

[2] Ola Lædre Nils Olsson Olav Torp Bjørn Andersen, Ali Hosseini. Pre-study ferry free e39. Technical report, 2016.

[3] C. Warren Campbell. Adding computationally j efficielt reaksm to monte carlo turbulence simulation. Technical report, 1985.

[4] Zhengshun Cheng, Zhen Gao, and Torgeir Moan. Hydrodynamic load modeling and analysis of a floating bridge in homogeneous wave conditions. *Marine Structures*, 59:122 – 141, 2018.

[5] Zhengshun Cheng, Zhen Gao, and Torgeir Moan. Numerical Modeling and Dynamic Analysis of a Floating Bridge Subjected to Wind, Wave, and Current Loads. *Journal of Offshore Mechanics and Arctic Engineering*, 141(1), 07 2018. 011601.

[6] Zhengshun Cheng, Zhen Gao, and Torgeir Moan. Wave load effect analysis of a floating bridge in a fjord considering inhomogeneous wave conditions. *Engineering Structures*, 163:197–214, 05 2018.

[7] Zhengshun Cheng, Erik Svangstu, Zhen Gao, and Torgeir Moan. Field measurements of inhomogeneous wave conditions in bjørnafjorden. *Journal of Waterway Port Coastal and Ocean Engineering*, 145:05018008, 01 2019.

[8] COWI. Straight bridge – navigation channel in south. Technical report, 2016.

[9] DNV. Recommended practice dnv-rp-c205,environmental conditions and environmental loads. Technical report, 2010.

[10] O. Faltinsen. *Sea Loads on Ships and Offshore Structures*. Cambridge Ocean Technology Series. Cambridge University Press, 1993.

[11] Sunghun Hong. The effect of damping on the dynamic responses of a floating bridge in wind and waves. 2019.

[12] MARINTEK. Simo - user's manual version 4.0 rev 3. Technical report, 2019.

[13] E. Simley and L. Y. Pao. A longitudinal spatial coherence model for wind evolution based on large-eddy simulation. In *2015 American Control Conference (ACC)*, pages 3708–3714, 2015.

[14] Statens vegvesen. Design basis bjørnafjorden, side- and end anchored floating bridge. Technical report, 2016.

[15] Statens vegvesen. An update from the fjord crossing project. presentation. Technical report, 2016.

[16] Statens vegvesen. The coastal highway route e39: Overview summary. Technical report, 2018.

[17] Statens vegvesen. The coastal highway route e39: Choice of technology for fjord crossings. Technical report, 2019.

[18] Wei Wei, Shixiao Fu, Torgeir Moan, Chunhui Song, and Tongxin Ren. A time-domain method for hydroelasticity of very large floating structures in inhomogeneous sea conditions. *Marine Structures*, 57:180 – 192, 2018.

Appendix

4.4 Mean Value of Results of the Global Dynamic Analyses Under 1-year Wave Condition
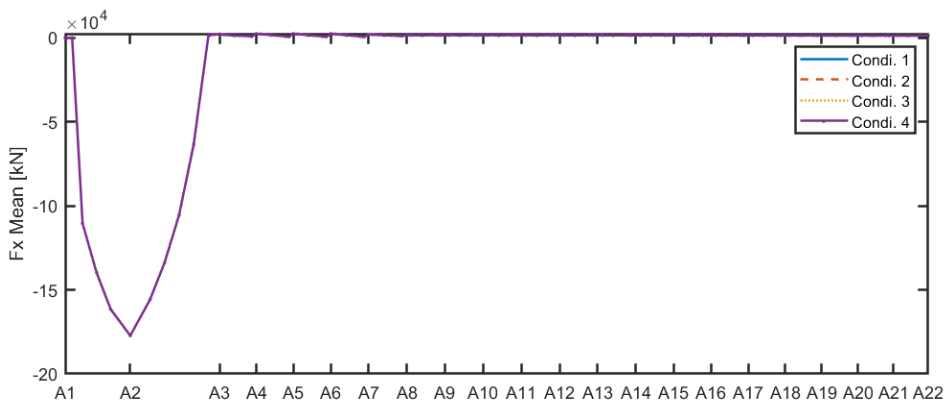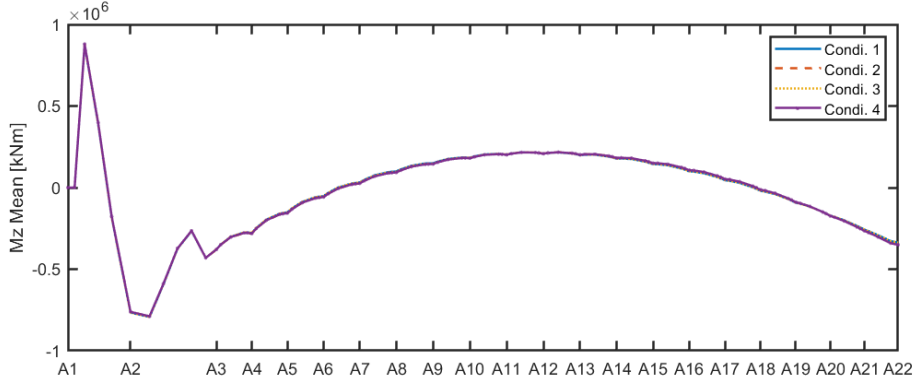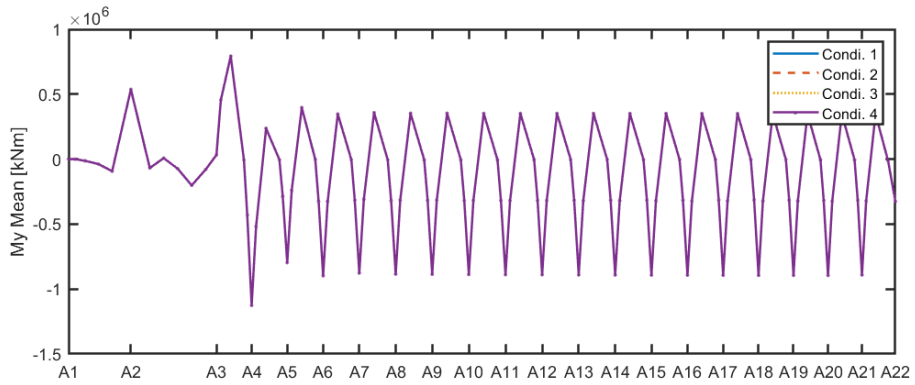

Figure 4.1: The mean value of axial force F_x along the bridge girder under 1-year wave condition
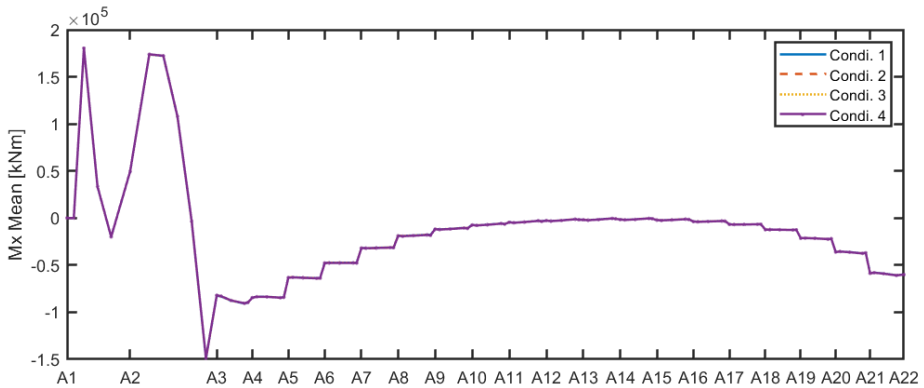
4.5 Mean Value of Results of the Global Dynamic Analyses Under 100-year Wave Condition

(a) Moment about bridge girder strong axis, M_z

(b) Moment about bridge girder weak axis, M_y

(c) Torsion moment, M_x

Figure 4.2: The mean value of (a) moment about bridge girder strong axis, M_z, (b) moment about bridge girder weak axis, M_y, (c)torsion moment, M_x, along the bridge girder under 100-year wave condition.
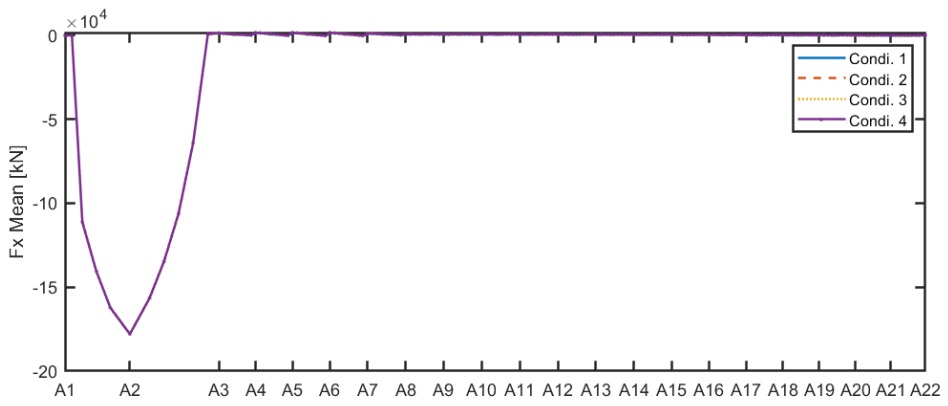
Figure 4.3: The mean value of axial force F_x along the bridge girder under 100-year wave condition